

Diese Dissertation haben beurteilt:

.....  
Prof. de Brion

.....  
Prof. Blaha



TECHNISCHE  
UNIVERSITÄT  
WIEN

DISSERTATION

**Far infrared spectroscopy of  
lattice dynamics in oxides with  
magnetically frustrated geometry**

ausgeführt zum Zwecke der Erlangung des akademischen Grades  
eines Doktors der technischen Wissenschaften  
unter der Leitung von

**Univ.Prof. Dr. Andrei Pimenov**

und

**Dr. Evan Constable**

E138

Institut für Festkörperphysik

eingereicht an der Technischen Universität Wien  
Fakultät für Physik

von

**Dipl.-Ing Lorenz Bergen BSc.**

Matrikelnummer 1027623

Adolf-Czettel-Gasse 7/45

1160 Wien

Wien, 6. März 2022

---

Lorenz Bergen



---

# Abstract

---

Magnetically frustrated materials have raised considerable research interest due to their tendency to exhibit a variety of exotic physical phenomena, such as spin-ice and spin-liquid states. In these systems, magnetic moments cannot minimise their interaction energies with all neighbouring spins simultaneously. Local ordering principles can then often take hold, stabilising a degenerate network of magnetic configurations, from which novel non-conventional magnetism emerges. Since the lattice geometry is a primary source of the frustration in these systems, studying the lattice dynamics directly is a useful way to gain insight about the environment that supports these novel frustrated spin states.

The aim of my thesis is to investigate the lattice dynamics of different magnetically frustrated materials to help improving our understanding of the exotic magnetic states they support. The main experimental work was performed using a Fourier transform infrared spectrometer in reflectance mode in combination with a He-flow cryostat to cool the samples down to temperatures approaching  $\sim 10$  K. My investigations cover phonon spectra in the (far-) infrared regime (spectral range:  $25\text{ cm}^{-1}$  to  $14000\text{ cm}^{-1}$ ) in three groups of materials.

These include langasite  $\text{La}_3\text{Ga}_5\text{SiO}_{14}$  which was studied to characterise a low-frequency phonon arising at  $\sim 40\text{ cm}^{-1}$  for  $E\parallel c$  polarisation. In this system, the La ions form a distorted kagome network. Frustration comes into play by replacing La with magnetic rare-earth ions ( $R_3\text{Ga}_5\text{SiO}_{14}$  where  $R = \text{rare-earth element}$ ). A softening of the low-frequency phonon with reduced temperature and increased substituted ion's atomic number is observed, indicating a possible instability of the langasite structure at low temperatures. Calculating the dielectric function highlights this low-frequency phonon as the main contribution of the langasite's large static permittivity,  $\varepsilon(0) \sim 100$ .

Francisite  $\text{Cu}_3\text{Bi}(\text{SeO}_3)_2\text{O}_2\text{Cl}$  is characterised by a structural phase transition at 115 K that makes this material a rare example of a soft-mode driven antiferroelectric. My studies focused on investigating signatures of a close lying ferroelectric phase that represents a polarisation of the antiferroelectric sublattices. A polar soft mode was identified in the infrared regime, its dynamics studied and connected to the lattice dynamics. Francisite is another distorted kagome system that features frustrated  $\text{Cu}^{2+}$  spins. The consequences of polar soft modes in close proximity to spin wave excitations are also investigated.

The pyrochlore lattice of corner-sharing tetrahedra is the prototype of a three dimensional frustrated system. Rare-earth pyrochlores,  $R_2B_2O_7$ , are a hot topic in condensed matter research with  $\text{Ho}_2\text{Ti}_2\text{O}_7$ , for example, shown to exhibit novel spin-ice properties. On the other hand, the ground state of  $\text{Tb}_2\text{Ti}_2\text{O}_7$  has remained a puzzle for sometime, with many experimental signatures pointing towards a spin-liquid state. Thus, I have used infrared spectroscopy to study the lattice dynamics of  $\text{Tb}_2\text{Ti}_2\text{O}_7$  single crystals in comparison with a  $\text{Tb}_2\text{Sn}_2\text{O}_7$  powder pellet and the spin ice  $\text{Ho}_2\text{Ti}_2\text{O}_7$  single crystal. A unique splitting of phonons can be observed in  $\text{Tb}_2\text{Ti}_2\text{O}_7$  providing evidence of a lattice distortion that breaks fundamental symme-

---

tries related to the magnetism. This observation supports the theory that  $\text{Tb}_2\text{Ti}_2\text{O}_7$  features a novel vibronic spin-liquid ground state.

Together, these studies highlight how the lattice and its dynamics can influence the environments that host frustrated spin systems producing unexpected behaviour.



---

# Kurzfassung

---

Magnetisch frustrierte Materialien neigen zur Bildung von außergewöhnlichen physikalischen Effekten wie Spin-Eis und Spin-Flüssigkeit Zuständen und haben damit die Aufmerksamkeit der Forschung auf sich gezogen. In diesen Systemen ist es den magnetischen Momenten nicht möglich die Wechselwirkungsenergie mit allen benachbarten Spins gleichzeitig zu minimieren. Lokale Ordnungsprinzipien greifen dabei und können ein entartetes Netzwerk von magnetischen Anordnungen stabilisieren, aus dem neuartige unkonventionelle magnetische Effekte entstehen. In diesen Systemen ist die Geometrie des Gitters die Hauptursache der Frustration. Daher ist es sinnvoll die Gitterdynamik direkt zu untersuchen, um Einblick in die Umgebungen zu bekommen, die diese frustrierten Spin-Zustände bilden.

Das Ziel meiner Arbeit ist es die Gitterdynamik verschiedener magnetisch frustrierter Materialien zu untersuchen, um ein besseres Verständnis für die exotischen magnetischen Zustände zu entwickeln, die in diesen Materialien entstehen können. Der Großteil der Experimente wurde mit einem Fourier Transformation Infrarot-Spektrometer in Reflexionsanordnung in Kombination mit einem He-Fluss Kryostat durchgeführt, um die Proben während der Messungen auf Temperaturen von annähernd 10 K zu kühlen. Meine Untersuchungen beinhalten Phononenspektren von drei Materialgruppen im (fern-) infraroten Spektralbereich (zwischen  $25\text{ cm}^{-1}$  und  $14000\text{ cm}^{-1}$ ).

Eines dieser Materialien ist der Langasit  $\text{La}_3\text{Ga}_5\text{SiO}_{14}$ , welcher untersucht wurde, um ein niederfrequentes Phonon zu charakterisieren, das bei  $\sim 40\text{ cm}^{-1}$  in  $E\parallel c$  Polarisation zu sehen ist. Die La Ionen bilden in diesem System ein verzerrtes Kagome-Gitter. Werden die Lanthan Ionen durch magnetische Ionen der Seltenen Erden ersetzt ( $R_3\text{Ga}_5\text{SiO}_{14}$ , mit  $R =$  Element der Seltenen Erden), entstehen frustrierte Netzwerke. Die Frequenz des niederfrequenten Phonons wird geringer, je niedriger die Probentemperatur bzw. je größer die Kernladungszahl des eingesetzten Ions ist. Dies deutet auf eine Instabilität des Langasit-Gitters bei niedrigen Temperaturen hin. Berechnungen der dielektrischen Funktion zeigen, dass dieses niederfrequente Phonon den Hauptbeitrag zu der üblicherweise hohen statischen Permittivität ( $\epsilon(0) \sim 100$ ) liefert.

Francisit  $\text{Cu}_3\text{Bi}(\text{SeO}_3)_2\text{O}_2\text{Cl}$  ist durch einen strukturellen Phasenübergang bei 115 K charakterisiert, der dieses Material zu einem seltenen Beispiel eines Soft-Mode getriebenen Antiferroelektrikums macht. Meine Arbeit fokussiert sich auf Anzeichen einer angrenzenden ferroelektrischen Phase, die der Polarisation der antiferroelektrischen Untergitter entspricht. Im infraroten Spektralbereich konnte eine polare Soft-Mode identifiziert werden. Ihre Dynamik wurde untersucht und mit der Gitterdynamik in Verbindung gebracht. Francisit ist ein weiteres frustriertes System mit einem Kagome Gitter, das die frustrierten  $\text{Cu}^{2+}$  Spins beinhaltet. Des Weiteren werden die Konsequenzen der in der Nähe zu Spin-Wellen Anregungen liegenden Soft-Mode untersucht.

Das Pyrochlor Gitter, bestehend aus Tetraedern mit gemeinsamen Eckpunkten, ist das einfachste Modell eines dreidimensionalen frustrierten Systems. Seltenerd-

---

Pyrochlore  $R_2B_2O_7$  zählen zu den aktuellen Themen der Forschung im Bereich der kondensierten Materie, da beispielsweise in  $Ho_2Ti_2O_7$  neuartige Spin-Eis Zustände zu sehen sind. Andererseits gibt der Grundzustand von  $Tb_2Ti_2O_7$  noch immer Rätsel auf, da es einige experimentelle Anzeichen für einen Spin-Flüssigkeit Zustand gibt. Daher habe ich die Gitterdynamik von  $Tb_2Ti_2O_7$  mit Infrarot-Spektroskopie untersucht und die Resultate mit denen eines  $Tb_2Sn_2O_7$  Pulverpellets und eines  $Ho_2Ti_2O_7$  Spin-Eis Einkristalls verglichen. Die Phononen in  $Tb_2Ti_2O_7$  zeigen eine einzigartige Spaltung und beweisen damit eine Gitterverzerrung, die fundamentale Symmetrien des Magnetismus bricht. Diese Beobachtung unterstützt die Theorie, dass  $Tb_2Ti_2O_7$  einen neuartigen vibronischen Spin-Flüssigkeit Grundzustand besitzt.

Zusammenfassend hebt meine Arbeit hervor, wie das Gitter und seine Dynamik die Umgebungen von frustrierten Spinsystemen beeinflussen, was zu außergewöhnlichem Verhalten führt.

---

## List of abbreviations

<b>AF</b>	antiferromagnetic
<b>AFE</b>	antiferroelectric
<b>BMS</b>	beam splitter
<b>BWO</b>	backward-wave oscillator
<b>CEF</b>	crystal electric field
<b>DC</b>	direct current
<b>DLaTGS</b>	deuterated L-alanine doped triglycine sulfate
<b>DTGS</b>	deuterated triglycine sulfate
<b>FE</b>	ferroelectric
<b>FIR</b>	far infrared
<b>FM</b>	ferromagnetic
<b>FTIR</b>	Fourier transform infrared
<b>KK</b>	Kramers-Kronig
<b>LHe</b>	liquid helium
<b>LN<sub>2</sub></b>	liquid nitrogen
<b>MCT</b>	mercury cadmium telluride
<b>MIR</b>	mid infrared
<b>NIR</b>	near infrared
<b>PE</b>	polyethylene
<b>PPMS</b>	physical properties measurement system
<b>THz</b>	terahertz

---

## List of symbols

$c$	vacuum velocity of light
$\mathbf{E}, \mathbf{E}, E$	electric field
$e_0$	elementary charge
$\mathbf{f}$	stimulus
$G$	response function
$\hbar$	Planck's constant
$\mathcal{H}$	Hamiltonian
$I$	intensity
$J$	interaction energy
$k, k, \mathbf{k}$	wave vector
$k_B$	Boltzmann constant
$m, M$	mass
$N$	refractive index
$P$	polarisation
$R$	reflectance
$r$	reflectivity
$\mathbf{S}, S$	spin
$SW$	spectral weight
$T$	temperature
$\mathbf{X}$	response
$\Delta\varepsilon$	dielectric contribution
$\varepsilon = \varepsilon_1 + i\varepsilon_2$	dielectric function
$\varepsilon(0)$	static permittivity
$\varepsilon_\infty$	high frequency permittivity
$\varepsilon_0$	vacuum permittivity
$\gamma$	damping
$\eta$	order parameter
$\lambda$	wavelength
$\bar{\nu}$	wave number
$\chi$	susceptibility
$\varphi$	phase angle
$\omega$	frequency
$\omega_P$	plasma frequency
$\omega_0$	resonance frequency

---

## List of samples

### Langasites

LGS	$\text{La}_3\text{Ga}_5\text{SiO}_{14}$
HoLGS	$(\text{Ho}_x\text{La}_{1-x})_3\text{Ga}_5\text{SiO}_{14}$
NGS	$\text{Nd}_3\text{Ga}_5\text{SiO}_{14}$
PGS	$\text{Pr}_3\text{Ga}_5\text{SiO}_{14}$

### Francisite

CBSCl	$\text{Cu}_3\text{Bi}(\text{SeO}_3)_2\text{O}_2\text{Cl}$
-------	---

### Pyrochlores

HTO	$\text{Ho}_2\text{Ti}_2\text{O}_7$
TTO	$\text{Ti}_2\text{Ti}_2\text{O}_7$
TSO	$\text{Ti}_2\text{Sn}_2\text{O}_7$

---

---

# Contents

---

<b>Abstract</b>	<b>iii</b>
<b>Kurzfassung</b>	<b>v</b>
<b>List of abbreviations</b>	<b>vii</b>
<b>List of symbols</b>	<b>viii</b>
<b>List of samples</b>	<b>ix</b>
<b>1 Introduction</b>	<b>1</b>
1.1 Motivation . . . . .	2
1.2 About this thesis . . . . .	4
1.3 Scientific outcome . . . . .	5
1.3.1 List of publications . . . . .	5
1.3.2 Presentation of my work at international conferences and meetings . . . . .	7
1.3.3 Co-supervised students' works . . . . .	8
<b>2 Methods</b>	<b>9</b>
2.1 Lorentz-oscillator model . . . . .	10
2.2 Phonons . . . . .	13
2.2.1 Dispersion relation of phonons . . . . .	14
2.2.2 Interaction of phonons with electromagnetic waves . . . . .	17
2.2.3 Dielectric function of phonons . . . . .	17
2.3 Phonons as an indicator of structural stability: soft modes . . . . .	18
2.3.1 Ferroelectric phase . . . . .	18
2.3.2 Landau theory of phase transitions . . . . .	20
<b>3 Experimental methods</b>	<b>23</b>
3.1 Fourier transform infrared spectroscopy . . . . .	24
3.1.1 Basic concept . . . . .	24
3.1.2 Components of the setup . . . . .	27
3.1.3 Data acquisition . . . . .	29
3.1.4 Kramers-Kronig analysis . . . . .	33
3.2 Quasi-optical THz-spectroscopy . . . . .	39
3.2.1 Mach-Zehnder interferometer . . . . .	40
3.2.2 Phase measurements and data processing . . . . .	42
3.3 Physical Properties Measurement System . . . . .	44
3.4 Experimental spectral ranges and units . . . . .	45
<b>4 Low-frequency phonon dynamics in rare-earth langasites</b>	<b>47</b>
4.1 Introduction . . . . .	48

4.2	Data processing . . . . .	50
4.3	The prototype langasite - $\text{La}_3\text{Ga}_5\text{SiO}_{14}$ . . . . .	53
4.3.1	$E\parallel c$ . . . . .	53
4.3.2	$E\parallel b^*$ . . . . .	58
4.4	Rare-earth substituted langasites . . . . .	59
4.4.1	$E\parallel c$ . . . . .	59
4.4.2	$E\parallel b^*$ . . . . .	64
4.5	Isotropy of langasite c-cut samples . . . . .	65
4.6	Summary . . . . .	66
<b>5</b>	<b>Soft-mode lattice dynamics in francisite</b>	<b>69</b>
5.1	Introduction and structural properties of francisite . . . . .	70
5.2	Data treatment . . . . .	71
5.3	Results . . . . .	72
5.3.1	Reflectance and dielectric function . . . . .	72
5.3.2	Fits . . . . .	74
5.3.3	Antiferroelectricity . . . . .	77
5.3.4	Ferroelectric signature of a soft mode . . . . .	78
5.3.5	Sublattice polarisation . . . . .	80
5.3.6	Spin-lattice effects in $\hat{b}$ -direction . . . . .	82
5.4	Summary . . . . .	83
<b>6</b>	<b>Phonon splitting in vibronic spin-liquid candidate <math>\text{Tb}_2\text{Ti}_2\text{O}_7</math></b>	<b>85</b>
6.1	Introduction . . . . .	86
6.1.1	The pyrochlore group and its structure . . . . .	86
6.1.2	Spin-ice states in pyrochlores . . . . .	86
6.1.3	The pyrochlore $\text{Tb}_2\text{Ti}_2\text{O}_7$ . . . . .	89
6.2	Analysis . . . . .	92
6.3	Results . . . . .	92
6.3.1	$\text{Ho}_2\text{Ti}_2\text{O}_7$ (HTO) . . . . .	92
6.3.2	$\text{Tb}_2\text{Ti}_2\text{O}_7$ (TTO) . . . . .	95
6.3.3	$\text{Tb}_2\text{Sn}_2\text{O}_7$ (TSO) . . . . .	98
6.4	Discussion and Summary . . . . .	100
<b>7</b>	<b>Conclusions and Outlook</b>	<b>101</b>
<b>A</b>	<b>Supplementary data</b>	<b>105</b>
A.1	Langasites . . . . .	106
A.1.1	Phonon data . . . . .	106
A.1.2	Spectra . . . . .	107
A.2	Francisite . . . . .	112
A.2.1	Phonon data . . . . .	112
A.2.2	Spectra . . . . .	113
A.3	Pyrochlores . . . . .	116



<b>Bibliography</b>	<b>117</b>
<b>List of Figures</b>	<b>136</b>
<b>List of Tables</b>	<b>140</b>
<b>Acknowledgement</b>	<b>143</b>



---

# 1

## Introduction

---

This chapter introduces the basic concepts of frustrated magnetism. A selection of consequences is discussed as a motivation for research in this fascinating field of physics. Later sections cover the outline of my thesis and the scientific outcome of my work.

### Contents

---

<b>1.1</b>	<b>Motivation</b>	<b>2</b>
<b>1.2</b>	<b>About this thesis</b>	<b>4</b>
<b>1.3</b>	<b>Scientific outcome</b>	<b>5</b>
1.3.1	List of publications	5
1.3.2	Presentation of my work at international conferences and meetings	7
1.3.3	Co-supervised students' works	8

---

## 1.1 Motivation

As a PhD-candidate, usually you can not be happy, when the term ‘*frustration*’ draws a red line throughout your studies. For me this was a bit different, as I investigated the exotic physics of magnetically frustrated materials with a focus on their lattice dynamics<sup>1</sup>. In physics we speak about magnetically frustrated systems when their microscopic magnetic moments (the so called spins) cannot minimise their interactions with all of their nearest neighbored spins simultaneously [1]. This leads to magnetic networks that can stabilise into a variety of highly degenerated ground states [2, 3]. Famous examples include states like spin glass [4], spin ice [5] and spin liquid phases [6]. In my thesis, only systems with geometric magnetic frustration are covered, i.e. the effects of frustration occur because of lattice properties [7]. Symmetric and competing interactions of ferro- and antiferromagnetic bonds are another origin of frustration [7].

The simplest picture of a frustrated system is the arrangement of three Ising spins on the corners of a triangle [8] as plotted in Figure 1.1. These spins  $\mathbf{S}$  are aligned parallel to one axis and can be either in the state ‘up’ or ‘down’. In this so called Ising model, we want to minimise the energy, expressed by the Hamiltonian  $\mathcal{H}$

$$\mathcal{H} = - \sum_{\langle i,j \rangle} J_{ij} \mathbf{S}_i \cdot \mathbf{S}_j. \quad (1.1)$$

Here  $\mathbf{S}_i$  and  $\mathbf{S}_j$  represent the spins on the lattice with positions  $i$  and  $j$ , respectively.  $J_{ij}$  is the exchange energy between these spins  $\mathbf{S}_i$  and  $\mathbf{S}_j$ . For simplification, this property vanishes, when the positions  $i$  and  $j$  are not nearest neighbours, thus there is no interaction between next nearest neighbours. The sign of  $J_{ij} \neq 0$  corresponds to the type of magnetic interaction. Positive  $J_{ij}$  represents a ferromagnetic interaction, while  $J_{ij} < 0$  represents an antiferromagnetic interaction. Starting with the ferromagnetic case, in this configuration all spins are parallel, in Figure 1.1(a) I choose them as ‘up’. One can see that the ferromagnetic interaction energy  $J_F$  is the same for each pair of spins, because the nearest neighbour is always pointing in the same direction (for simplification, the indices  $i, j$  of  $J_{ij}$  are neglected from now on). Thus, the system is not frustrated.

Now let us have a look at the antiferromagnetic (AF) case. Here the interaction  $\mathcal{H}_{AF}$  reaches its minimum for nearest neighbored spins in antiparallel configuration. In Figure 1.1(b), the spins on the baseline of the triangle are placed first. While the left one is ‘up’, the right one is ‘down’. These two spins are antiparallel, thus minimising  $\mathcal{H}_{AF}$ . But how do we place the third spin on the top of the triangle? Independent of its direction, this spin is parallel to one of the two neighbours, such that the magnetic Hamiltonian is in fact maximised. The system is frustrated [7]. Both directions of the third spin are energetically equivalent, thus the degeneracy of frustrated states is clearly observed in this basic example. One possible realisation is a 120° arrangement of Ising axes with double degeneracy depending on the rotation direction [9, 10].

---

<sup>1</sup>Read carefully. It is not written that I was never frustrated.

Two-dimensional frustrated networks can often occur in layered materials, with examples including the honeycomb [11–14] or kagome lattices [15–19], as plotted in Figure 1.2. The prototype in three dimensions is the pyrochlore lattice, a system of corner-sharing tetrahedra [20–23]. Materials with kagome and pyrochlore lattices in particular were studied during the course of my thesis.

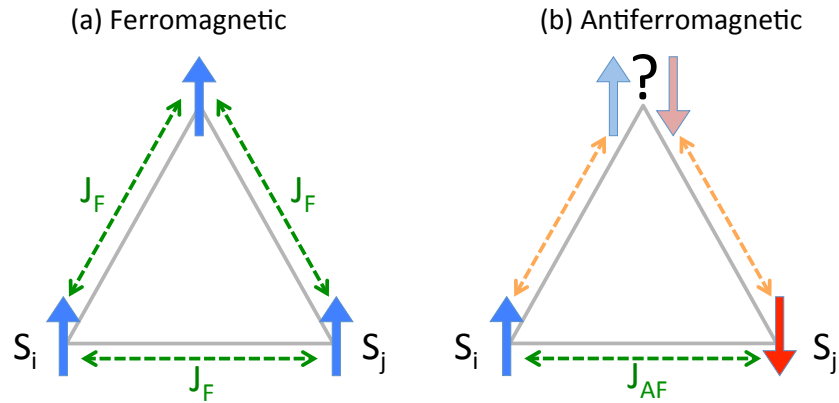


**Figure 1.1:** Possible arrangements of three spins located on the corners of a triangle for ferromagnetic (a) and antiferromagnetic (b) interactions.

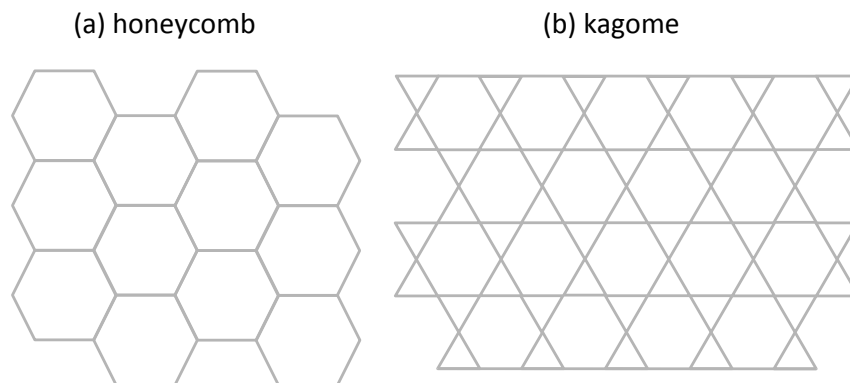


**Figure 1.2:** The two-dimensional honeycomb (a) and kagome (b) lattice.

The degeneracy of the magnetic ground state in frustrated magnets is a result of local organising principles, that allow a huge number of possible spin arrangements. This leads to the creation of novel phases such as spin-ice and spin-liquid states. For example, in each tetrahedron of a spin-ice pyrochlore lattice, two of the corner-placed spins must point towards the center and two in the other direction [5] as plotted in Figure 1.3(a). Now, many arrangements are possible that fulfil this ordering rule. One of the most exotic phenomena of frustrated magnetism can be achieved by flipping a single connecting spin of two tetrahedra within a spin ice. This 3-in/1-out spin

situation for a tetrahedron (and 1-in/3-out for its neighbored one, see Figure 1.3(b)) yields effective magnetic net charges, i.e. magnetic monopoles [24–27].

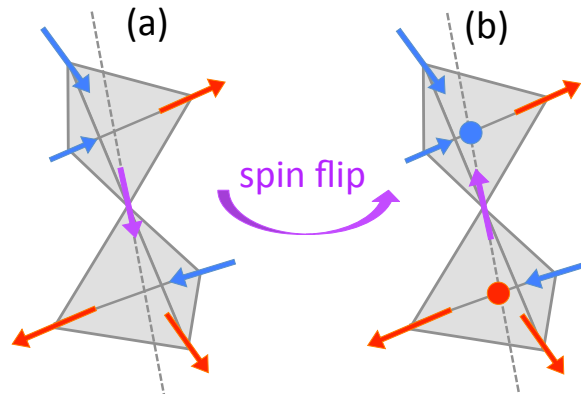


**Figure 1.3:** (a) Tetrahedra in spin-ice with a 2-in/2-out local organising principle and (b) after flipping the connecting spin to a 3-in/1-out and 1-in/3-out local organising principle, such that magnetic charges are created.

These systems can be difficult to probe since there is no macroscopic magnetic order to couple to with, for example, optical radiation. Moreover there is growing evidence that spin-lattice effects can play an important role in a number of intriguing frustrated systems. Thus, my thesis aims to study the phonon spectra in a number of frustrated materials to better understand their dielectric properties and the lattice environment from which the frustration emerges.

## 1.2 About this thesis

This thesis was performed under the supervision of Prof. Andrei Pimenov and Dr. Evan Constable at the Institute of Solid State Physics at TU Wien in the years 2017 to 2021. The experiments were performed in laboratories of the Solid State Spectroscopy Group at TU Wien. Data from additional experiments, performed by collaborators, is marked in the text.

This work was financially supported by the Austrian Science Fund (FWF) projects “Voltage” and “Solids4Fun”, a Doctoral School I was associated to.

Chapter 1 covers a short introduction to geometric magnetic frustration, along with a brief description of the structure of my thesis and the scientific outcome of my PhD studies.

The theoretical methods implemented in my work, are summarised in Chapter 2. An overview of the basic concepts of phonons (lattice vibrations) and connected phenomena is presented. Two spectroscopic methods (Fourier transform infrared spec-

troscopy and Quasi-optical THz-spectroscopy) were used for the main experimental measurements of my work. These setups are described in Chapter 3 together with the static measurement system, necessary for data acquisition at very low frequencies. The working principle of each of the systems is introduced and the data acquisition and analysis processes are described in detail.

Following these introductory chapters, the experimental results will be presented. Three different groups of materials were studied, each of them presented in its own chapter. In general, the structure of these individual results chapters is identical. They start each with an introduction of the investigated material and the specific data analysis process, then cover the results and finish with a discussion.

In Chapter 4, the low frequency phonons of langasite  $\text{La}_3\text{Ga}_5\text{SiO}_{14}$  are studied. The influence of the replacement of lanthanum with different rare-earth elements is studied, as well as the temperature dependence of the dielectric function along different crystallographic directions. An anomalous soft mode indicates a structural instability in langasite with its frequency lying in close vicinity to the rare-earth ion's crystal electric field levels. Thus, the possibility for how the phonon dynamics might influence the magnetism of these systems, is also explored. Chapter 5 covers the investigation of francisite  $\text{Cu}_3\text{Bi}(\text{SeO}_3)_2\text{O}_2\text{Cl}$ , a rare example of a material with an antiferroelectric and antiferromagnetic phase. The focus lies on the characterisation of a soft-mode driven structural phase transition in this compound and the related lattice dynamics. As francisite is also antiferroelectric with frustrated spins, the question is raised how do the lattice and spin waves interact, and how do they influence the magnetic Hamiltonian of the system. As mentioned in the motivation, the pyrochlore lattice is the textbook example for a frustrated network in three dimensions. Chapter 6 focusses on phonon spectroscopy of a number of members from this group of materials. First, the spin ice  $\text{Ho}_2\text{Ti}_2\text{O}_7$  is studied. A comparison with  $\text{Tb}_2\text{Ti}_2\text{O}_7$  is performed to help understand broken lattice symmetries that drive the peculiar magnetic ground state properties of this compound.

Finally, Chapter 7 summarises my work and connects the results of the three investigated materials. An outlook to potential future experiments and ideas for the next steps to be taken in order to continue to advance the research started in this thesis is given.

Appendix A provides further infrared spectra of the investigated materials and lists the phonon frequencies and related peak properties.

## 1.3 Scientific outcome

The results of my studies were prepared for publication in scientific journals. International conferences were visited to present the latest results of the investigations. The details are listed below.

### 1.3.1 List of publications

Publications directly related to my thesis:

1. **L. Bergen**, L. Weymann, J. Wettstein, A. M. Kuzmenko, A. A. Mukhin, B. V. Mill, A. Pimenov, and E. Constable:  
*“Lattice contributions to the anisotropic dielectric response of rare-earth langasites.”*  
Physical Review B. **104**, 024106 (2021)
2. L. Weymann, **L. Bergen**, T. Kain, A. Pimenov, A. Shuvaev, E. Constable, D. Szaller, B. V. Mill, A. M. Kuzmenko, V. Y. Ivanov, N. V. Kostyuchenko, A. I. Popov, A. K. Zvezdin, A. Pimenov, A. A. Mukhin and M. Mostovoy:  
*“Unusual magnetoelectric effect in paramagnetic rare-earth langasite.”*  
npj Quantum Materials **5**, 1 (2020).
3. **L. Bergen et al.**:  
*“Polar soft-mode dynamics in candidate antiferroelectric francisite  $Cu_3Bi(SeO_3)_2O_2Cl$ .”*  
under preparation
4. **L. Bergen et al.**:  
*“Infrared phonon dynamics reveal broken symmetries in vibronic spin liquid candidate  $Tb_2Ti_2O_7$ .”*  
under preparation

Publications not directly related to the work of my PhD Thesis:

1. C. Gollner, M. Shalaby, C. Brodeur, I. Astrauskas, R. Jutas, E. Constable, **L. Bergen**, A. Baltuška, A. Pugžlys:  
*“Highly efficient THz generation by optical rectification of mid-IR pulses in DAST.”*  
APL Photonics **6**, 046105 (2021).
2. E. Gruber, **L. Bergen**, P. Salou, E. Lattouf, C. Grygiel, Y. Wang, A. Benyagoub, D. Levavasseur, J. Rangama, H. Lebius, B. Ban-d’Etat, M. Schleberger and F. Aumayr:  
*“High resolution AFM studies of irradiated mica - following the traces of swift heavy ions under grazing incidence.”*  
Journal of Physics: Condensed Matter **30**, 285001 (2018).

Other publications to date:

1. E. Gruber, P. Salou, **L. Bergen**, M. El Kharrazi, E. Lattouf, C. Grygiel, Y. Wang, A. Benyagoub, D. Levavasseur, J. Rangama, H. Lebius, B. Ban-D’Etat, M. Schleberger, F. Aumayr:  
*“Swift heavy ion irradiation of  $CaF_2$  - from grooves to hillocks in a single ion track.”*  
Journal of Physics: Condensed Matter **28**, 4050011 (2016).



2. E. Gruber, E. Lattouf, **L. Bergen**, P. Salou, C. Grygiel, Y.Y. Wang, O. Ochedowski, A. Benyagoub, D. Lavavasseur, J. Rangama, H. Lebius, B. Ban D'Etat, M. Schleberger, and F. Aumayr:  
*“Studies of surface nanostructure formation due to swift heavy ion irradiation under grazing incidence.”*  
 Journal of Physics: Conference Series **635**, 032001 (2015).

### 1.3.2 Presentation of my work at international conferences and meetings

#### Oral contributions:

1. **L. Bergen**, E. Constable, L. Weymann, A. A. Mukhin, Anna Pimenov and A. Pimenov: *“Far infrared studies on langasites”*; Talk: 3<sup>rd</sup> Grandmaster Early-Career Workshop in Physics, Vienna/Austria; February 22<sup>nd</sup>, 2018.
2. **L. Bergen**, E. Constable, L. Weymann, A. A. Mukhin, N. Kostyuchenko and A. Pimenov: *“Far infrared studies on a diluted rare-earth langasite”*; Talk: DPG-Frühjahrstagung (DPG Spring Meeting) and EPS-CMD27 (2018 Joint meeting of the DPG and EPS Condensed Matter Divisions), Berlin/Germany; March 15<sup>th</sup>, 2018.
3. **L. Bergen**, E. Constable, L. Weymann, A. A. Mukhin, Anna Pimenov and A. Pimenov: *“Low frequency phonons in langasites”*; Talk: Solids4Fun Summer School 2018, Waidhofen a. d. Ybbs/Austria; July 5<sup>th</sup>, 2018.
4. **L. Bergen**, L. Weymann, A. Pimenov, A. Kuzmenko, A. A. Mukhin, and E. Constable: *“Low frequency phonons in rare-earth langasites”*; Talk: DPG Spring Meeting 2019, Regensburg/Germany; April 1<sup>st</sup>, 2019.
5. **L. Bergen**, L. Weymann, A. Pimenov, A. Kuzmenko, A. A. Mukhin, and E. Constable: *“Low Frequency Phonons in Nd-Langasite”*; Talk: Solids4Fun Summer School 2019, Waidhofen a. d. Ybbs/Austria; July 4<sup>th</sup>, 2019.

#### Poster presentations:

1. **L. Bergen**, E. Constable, A. A. Mukhin, I. A. Gudim, L. N. Bezmaternykh, and A. Pimenov: *“Far infrared Studies on the diluted rare-earth Langasite  $La_{2.91}Ho_{0.09}Ga_5SiO_{14}$ ”*; Poster: Solids4Fun Summer School 2017, Waidhofen a. d. Ybbs/Austria; July 6<sup>th</sup>, 2017.
2. **L. Bergen**, E. Constable, L. Weymann, A. A. Mukhin, Anna Pimenov and A. Pimenov: *“Phonon Spectroscopy of Magnetoelectric Langasite”*; Poster: 33<sup>rd</sup> Workshop on Novel Materials and Superconductivity 2018, Obertraun/Austria; February 14<sup>th</sup>, 2018.

3. **L. Bergen**, L. Weymann, A. Pimenov, A. Kuzmenko, A. A. Mukhin, and E. Constable: “*Low frequency Phonons in Rare earth Langasites*”; Poster: VII Euro-Asian Symposium “Trends in MAGnetism” - EASTMAG 2019, Ekaterinburg/Russia; September 10<sup>th</sup>, 2019.
4. **L. Bergen**, L. Weymann, E. Malysheva, M. Guennou, H. Berger, A. Pimenov, and E. Constable: “*Far-Infrared dielectric response of antiferroelectric francisite  $Cu_3Bi(SeO_3)_2O_2Cl$* ”; Poster: 35<sup>th</sup> Workshop on Novel Materials and Superconductivity 2020, Schladming/Austria; February 12<sup>th</sup>, 2020.

Seminar Talks within the Doctoral School Solids4Fun:

- “*Fourier-Transform Infrared Spectroscopy*”, May 15<sup>th</sup>, 2017.
- “*Low frequency phonons in rare-earth langasites*”, April 8<sup>th</sup>, 2019.
- “*Far-infrared dielectric response of antiferroelectric francisite  $Cu_3Bi(SeO_3)_2O_2Cl$* ”, June 15<sup>th</sup>, 2020 (remote presentation).

### 1.3.3 Co-supervised students’ works

Within the time of my PhD I had the pleasure to co-supervise three students. Their theses are listed below.

- M. Moser:  
“*Fourier transform spectroscopic study of  $V_3Al$* ”  
Bachelor’s thesis, 2018.
- E. Malysheva:  
“*Infrared studies on antiferroelectric candidate francisite  $Cu_3Bi(SeO_3)_2O_2Cl$* ”  
Bachelor’s thesis, 2018.  
  
“*Temperature dependence of lattice contribution to dielectric response of francisite  $Cu_3Bi(SeO_3)_2O_2Cl$  (CBSCl)*”  
Project work, 2019.
- S. Black:  
“*Infrared spectroscopy of  $Fe_2VAl$  and  $Fe_2V_{0.8}W_{0.2}Al$  compounds*”  
Project work, 2021.

---

# 2

## Methods

---

This chapter presents the basic methods and underlying physics covered in my thesis. First the concept of the Lorentzian oscillator is explained, a model used to describe the lattice dynamics of solids. The second part gives an overview on phonons, the quantum mechanical approach to lattice vibrations, including its supporting theories. Finally, a more applied topic is shown concerning soft-modes. This kind of vibration indicates a structural instability of the lattice.

### Contents

---

<b>2.1 Lorentz-oscillator model</b>	<b>10</b>
<b>2.2 Phonons</b>	<b>13</b>
2.2.1 Dispersion relation of phonons	14
2.2.2 Interaction of phonons with electromagnetic waves	17
2.2.3 Dielectric function of phonons	17
<b>2.3 Phonons as an indicator of structural stability: soft modes</b>	<b>18</b>
2.3.1 Ferroelectric phase	18
2.3.2 Landau theory of phase transitions	20

---

## 2.1 Lorentz-oscillator model

The concept of a Lorentzian oscillator is named after the mathematical model of the Dutch physicist Hendrik Antoon Lorentz (\*1853 - †1928). The model describes the movement of an electron in an insulator [28], bound to an atomic core with a spring (spring constant  $C$ ). The electron harmonically oscillates at a resonance frequency  $\omega_e = \sqrt{C/m}$ , assuming it has a mass  $m$ . A damping constant  $\gamma$  is added, thus the equation of motion is given in the one dimensional case as [29]

$$m \frac{d^2x}{dt^2} + m\gamma \frac{dx}{dt} + m\omega_e^2 x = F(x), \quad (2.1)$$

with  $F$  being an external force acting on the mass at the position  $x$ . An electric field with an amplitude  $E_0$  oscillating at frequency  $\omega$ , e.g. created between two ions of different charge, results in a force on the electron [28],

$$F = e_0 E_0 e^{-i\omega t}, \quad (2.2)$$

with the electron's charge  $e_0$ . In this case Eq. (2.1) can be rewritten as

$$m \frac{d^2x}{dt^2} + m\gamma \frac{dx}{dt} + m\omega_e^2 x = e_0 E_0 e^{-i\omega t}. \quad (2.3)$$

Looking for plane wave solutions, one can then insert the substitution

$$x = x_0 e^{-i\omega t}, \quad (2.4)$$

yielding, after cancelling the common term  $e^{-i\omega t}$ ,

$$-\omega^2 m x_0 - i m \omega \gamma x_0 + m \omega_e^2 x_0 = e_0 E_0, \quad (2.5)$$

$$x_0 (-\omega^2 - i\omega\gamma + \omega_e^2) = e_0 E_0 / m, \quad (2.6)$$

$$x_0 = \frac{e_0 / m}{\omega_e^2 - \omega^2 - i\omega\gamma} E_0. \quad (2.7)$$

The dielectric polarisation,  $P$ , is given as

$$P(t) = e_0 n x(t), \quad (2.8)$$

with density  $n$ , but also as

$$P(t) = \varepsilon_0 \chi_e E, \quad (2.9)$$

with the vacuum permittivity  $\varepsilon_0$ . The two expressions of  $P$  are set equal, thus the dielectric susceptibility,  $\chi_e$ , can be expressed by

$$\chi_e(\omega) = \frac{ne_0}{\varepsilon_0} \frac{x_0}{E_0} = \frac{ne_0^2}{\underbrace{\varepsilon_0 m}_{\omega_p^2}} \frac{1}{\omega_e^2 - \omega^2 - i\omega\gamma}, \quad (2.10)$$

with the pre-factor labelled as  $\omega_p^2$ , the so called plasma frequency. Now the susceptibility is connected to the dielectric function via [29]

$$\varepsilon(\omega) = 1 + \chi(\omega) = 1 + \chi_c(\omega) + \chi_e(\omega). \quad (2.11)$$

The property  $\chi_c(\omega)$  includes effects of core electrons [29]. Defining the high-frequency dielectric permittivity as

$$\varepsilon_\infty = 1 + \chi_c(\omega), \quad (2.12)$$

gives the dielectric function [29]

$$\varepsilon(\omega) = \varepsilon_\infty + \frac{\omega_p^2}{\omega_e^2 - \omega^2 - i\omega\gamma}. \quad (2.13)$$

The effects of dense matter (local field correction: the polarisation of the medium itself has to be taken account) [29] can be included by subtracting the term [30]

$$E_m = \frac{4\pi}{3}P, \quad (2.14)$$

from the applied electric field. After some calculation, see reference [29] (page 49) we arrive at

$$\varepsilon(\omega) = \varepsilon_\infty + \frac{\omega_p^2}{\omega_0^2 - \omega^2 - i\omega\gamma}, \quad (2.15)$$

with

$$\omega_0^2 = \omega_e^2 - \frac{1}{3}\omega_p^2. \quad (2.16)$$

The complex dielectric function ( $\varepsilon = \varepsilon_1 + i\varepsilon_2$ ) consists of a real ( $\varepsilon_1$ ) and an imaginary component ( $\varepsilon_2$ ). These functions can be obtained from Eq. (2.15). Both the nominator and denominator of the the second term have to be multiplied with the complex conjugate of the denominator. Then, after splitting into the real and imaginary components we get:

$$\varepsilon_1(\omega) = \varepsilon_\infty + \frac{\omega_p^2(\omega_0^2 - \omega^2)}{(\omega_0^2 - \omega^2)^2 + \omega^2\gamma^2}, \quad (2.17)$$

$$\varepsilon_2(\omega) = \frac{\omega_p^2\omega\gamma}{(\omega_0^2 - \omega^2)^2 + \omega^2\gamma^2}. \quad (2.18)$$

A few more properties related to the Lorentzian oscillator include:

- $\varepsilon_\infty = \varepsilon(\infty)$ : the high frequency permittivity
- $\Delta\varepsilon = \omega_p^2/\omega_0^2$ : dielectric contribution
- $SW = \omega_p^2$ : spectral weight
- $\varepsilon(0) = \varepsilon_\infty + \Delta\varepsilon$ : static permittivity.

Knowledge about the dielectric function provides all the information needed to calculate the complex refractive index  $N$  via [29]

$$N = n + ik = \sqrt{\varepsilon}, \quad (2.19)$$

with  $n$  being the real part of the refractive index and  $k$  the extinction coefficient.

The normal incidence reflectance  $R$  is given by [29]

$$R = \left| \frac{1 - N}{1 + N} \right|^2 \quad (2.20)$$

and connected to the reflectivity  $r = \rho e^{i\varphi}$  via  $R = rr^*$  [31]. The optical conductivity,  $\sigma = \sigma_1 + i\sigma_2$ , of the material is connected to the dielectric function via [29]

$$\sigma = \frac{i\omega}{4\pi}(1 - \varepsilon). \quad (2.21)$$

Its real and imaginary parts are then given by<sup>2</sup>:

$$\sigma_1 = \varepsilon_2 \frac{\omega}{4\pi} \quad \text{and} \quad \sigma_2 = (1 - \varepsilon_1) \frac{\omega}{4\pi}. \quad (2.22)$$

## Example of a Lorentzian oscillator

The following example presents the typical behaviour of the dielectric function and the reflectance in the presence of a Lorentzian oscillator and is plotted in Figure 2.1. Here, the values are given in wavenumber units of  $\text{cm}^{-1}$  (this is just frequency divided by the vacuum speed of light). The values chosen are:

$$\begin{aligned} \omega_0 &= 400 \text{ cm}^{-1}, \\ \omega_p &= 600 \text{ cm}^{-1}, \\ \gamma &= 30 \text{ cm}^{-1}, \\ \varepsilon_\infty &= 3. \end{aligned}$$

---

<sup>2</sup>Inserting  $\sigma = \sigma_1 + i\sigma_2$  and  $\varepsilon = \varepsilon_1 + i\varepsilon_2$  in Eq. (2.21) gives

$$\begin{aligned} \sigma_1 + i\sigma_2 &= \frac{i\omega}{4\pi}(1 - \varepsilon_1 - i\varepsilon_2), \\ \sigma_1 + i\sigma_2 &= \varepsilon_2 \frac{\omega}{4\pi} + i(1 - \varepsilon_1) \frac{\omega}{4\pi}. \end{aligned}$$

This equation has to be valid for its **real** and **imaginary** part. Giving Eq. (2.22):

$$\sigma_1 = \varepsilon_2 \frac{\omega}{4\pi}$$

and

$$\sigma_2 = (1 - \varepsilon_1) \frac{\omega}{4\pi}.$$

The dielectric contribution of this oscillator can now be calculated according the definition above, giving  $\Delta\varepsilon = 600^2/400^2 = 2.25$  and a static permittivity of  $\varepsilon(0) = 2.25 + 3 = 5.25$ . In the plot, these properties are highlighted by the dashed lines. The maximum of  $\varepsilon_2$  occurs in close proximity to the resonance frequency<sup>3</sup>,  $\omega_0$ .

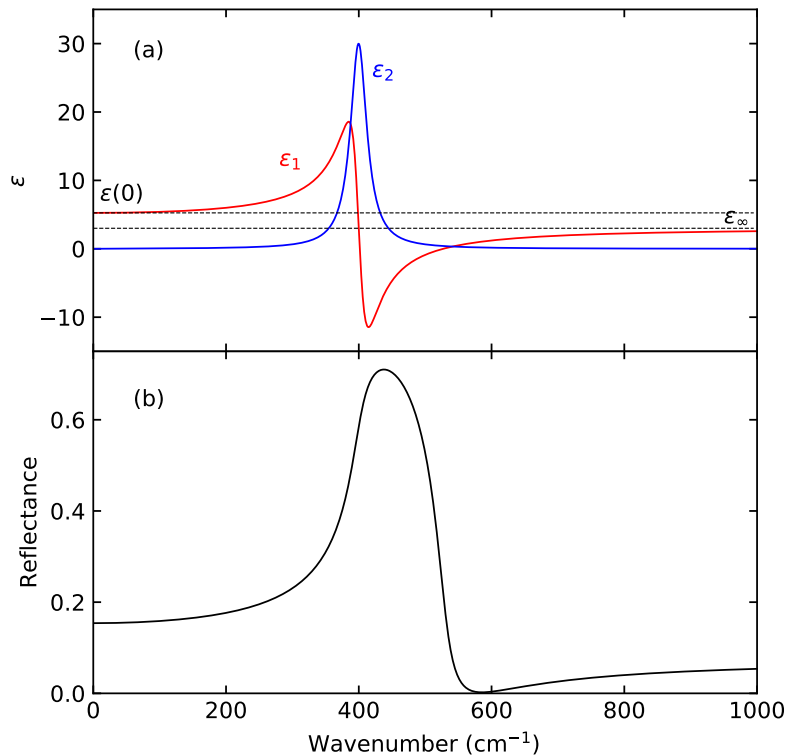


**Figure 2.1:** Dielectric function (a) and reflectance (b) of a Lorentzian oscillator. In (a) the dashed lines represent the value of  $\varepsilon_\infty$  (lower line) and  $\varepsilon(0)$  (upper line),  $\Delta\varepsilon$  is the difference of these two lines.

## 2.2 Phonons

Phonons are the quantum mechanical representations of lattice vibrations. Classically, phonons are the normal modes of the crystal lattice, described by the wave vector  $\mathbf{k}$  and the frequency  $\omega_{\mathbf{k}}$ . Two polarisations are possible, longitudinal (parallel to  $\mathbf{k}$ ) and transverse (perpendicular to  $\mathbf{k}$ ). Seen as quantum mechanical quasi particles, phonons have integer spin, thus they follow Bose-Einstein statistics. In thermal

<sup>3</sup>A second order Taylor series expansion of Eq. (2.18) at the position  $\omega - \omega_0$  yields

$$\omega_0 + \gamma^2/(8\omega_0)$$

as the maximum frequency, when  $\gamma \ll \omega_0$ .

equilibrium at a temperature  $T$ , the number of phonons  $N$  at a frequency  $\omega$  is given by the Planck distribution,

$$N = \frac{1}{e^{\hbar\omega/k_B T} - 1}, \quad (2.23)$$

with the Boltzmann constant  $k_B$ . Assuming harmonic oscillations of the vibrations, a phonon's energy eigenstates are quantized, thus the energy of the  $n^{\text{th}}$  level is

$$E_{\mathbf{k},n} = \hbar\omega_{\mathbf{k}} \left( n + \frac{1}{2} \right). \quad (2.24)$$

The phonon's momentum is  $\mathbf{p} = \hbar\mathbf{k}$ .

### 2.2.1 Dispersion relation of phonons

To obtain the classical dispersion relation (the connection between  $\omega_{\mathbf{k}}$  and  $\mathbf{k}$ ), the textbook example of a lattice with two different ions (masses) in the unit cell is chosen [29, 31]. In Figure 2.2, a one dimensional diatomic chain is presented. Here, two types of ions (masses  $M$  and  $m$ ) are arranged, such that two nearest neighbours are always of the other type. In undisplaced positions, the lattice parameter  $a$  gives the distance between two ions of same type.

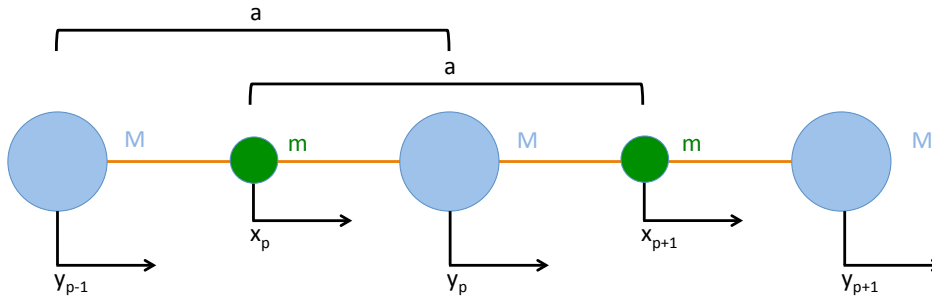


**Figure 2.2:** Model of a diatomic chain with a lattice parameter  $a$ . Atoms of mass  $M$  (blue circles) are at the  $y$ -positions, the atoms of mass  $m$  (green) are at the  $x$ -positions.

Hook's law

$$F = Cd, \quad (2.25)$$

describes a force  $F$ , required to move a spring with spring constant,  $C$ , to a displacement,  $d$ , from equilibrium. Each atom in the chain is connected to the neighbouring atoms of different type by two identical springs. Thus, for the atom at position  $x_p$  the forces are  $C(y_p - x_p)$ , in the right direction and  $C(x_p - y_{p-1})$  in the other direction, yielding the following equation of motion

$$m \frac{d^2 x_p}{dt^2} = C(y_p + y_{p-1} - 2x_p), \quad (2.26)$$



and for the ion at position  $y_p$

$$M \frac{d^2 y_p}{dt^2} = C(x_{p+1} + x_p - 2y_p). \quad (2.27)$$

The substitutions

$$x_p = x e^{ikap} e^{-i\omega t} \quad \text{and} \quad y_p = y e^{ikap} e^{-i\omega t}, \quad (2.28)$$

give, after some calculation<sup>4</sup>, the dispersion relation for a diatomic chain [29],

$$\omega_{\pm} = \left[ C \frac{M+m}{Mm} \pm C \sqrt{\left( \frac{M+m}{Mm} \right)^2 - \frac{4}{Mm} \sin^2(ka/2)} \right]^{1/2}. \quad (2.29)$$

Thus, for any  $\mathbf{k}$ , two solutions (branches) for  $\omega$  can be obtained (see Figure 2.3), one with a positive sign in Eq. (2.29),  $\omega_+$ , and one with the negative sign,  $\omega_-$  [29, 31].

<sup>4</sup> One inserts the substitution into Eq. (2.26) and (2.27). This gives, after cancelling the common factor  $e^{-i\omega t}$ ,

$$\begin{aligned} -\omega^2 m x e^{ikap} &= C y (e^{ikap} + e^{ika(p-1)}) - 2C x e^{ikap}, \\ -\omega^2 M y e^{ikap} &= C x (e^{ika(p+1)} + e^{ikap}) - 2C y e^{ikap}. \end{aligned}$$

Both equations are divided with the factor  $e^{ikap}$ , yielding

$$\begin{aligned} (-\omega^2 m + 2C)x - C(1 + e^{-ika})y &= 0, \\ (-\omega^2 M + 2C)y - C(1 + e^{ika})x &= 0. \end{aligned}$$

The upper of those two equations is solved for  $x$ :

$$x = \frac{C(1 + e^{-ika})}{-\omega^2 m + 2C} y.$$

This expression for  $x$  is then inserted into the equation above, leading, after multiplication with the denominator of  $x$ , to

$$\begin{aligned} (-\omega^2 m + 2C)(-\omega^2 M + 2C) - C^2(1 + e^{-ika})(1 + e^{ika}) &= 0, \\ \omega^4 - \omega^2 M 2C - \omega^2 m 2C + 4C^2 - C^2(1 + \underbrace{e^{ika} + e^{-ika}}_{2 \cos(ka)} + 1) &= 0, \end{aligned}$$

$$\omega^4 - \omega^2 2C \frac{M+m}{Mm} + \frac{2C^2}{Mm} \underbrace{(1 - \cos(ka))}_{2 \sin^2(ka/2)} = 0,$$

$$\omega^4 - \omega^2 2C \frac{M+m}{Mm} + \frac{4C^2}{Mm} \sin^2(ka/2) = 0,$$

$$\omega_{\pm}^2 = C \frac{M+m}{Mm} \pm C \sqrt{\left( \frac{M+m}{Mm} \right)^2 - \frac{4}{Mm} \sin^2(ka/2)}$$

and finally the dispersion relation Eq. (2.29),

$$\omega_{\pm} = \left[ C \frac{M+m}{Mm} \pm C \sqrt{\left( \frac{M+m}{Mm} \right)^2 - \frac{4}{Mm} \sin^2(ka/2)} \right]^{1/2}.$$

- $\omega_+$ : Optical branch. The typical frequency is in the order of the infrared regime of light. Thus interaction of light (photons) is allowed by conservation laws. If such a mode interacts with a photon, it is called optically active. The maximum of the dispersion relation occurs at  $\mathbf{k} = 0$ , the minimum occurs at  $\mathbf{k} = \pm\pi/a$ , which is the Brillouin zone boundary. Thus the maximum of  $\omega_+$  can easily be calculated as

$$\omega_{+0} = \omega_+(0) = \sqrt{2C \left( \frac{M+m}{Mm} \right)}. \quad (2.30)$$

Nearest neighboured atoms move in opposite directions.

- $\omega_-$ : Acoustic branch. This branch is characterised with  $\omega = 0$  for  $\mathbf{k} = 0$ , and a maximum at the zone boundaries. All atoms in the chain move along the same direction.

In total,  $3l$  branches exist in a three-dimensional lattice with  $l$  atoms in the primitive cell, 3 acoustic and  $3l-3$  optical [31]. Including the polarisation of the modes, four types of modes can be distinguished:

- longitudinal optical modes (LO),
- transverse optical modes (TO),
- longitudinal acoustic modes (LA),
- transverse acoustic modes (TA).

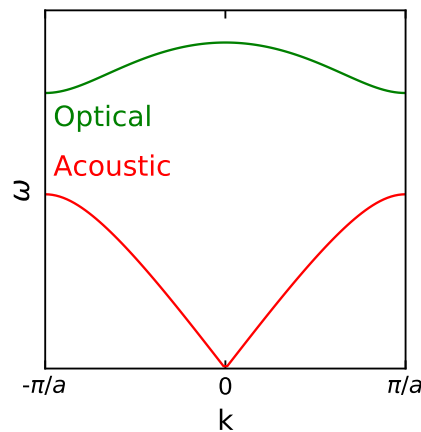


**Figure 2.3:** Dispersion of the diatomic chain (Eq. (2.29) and Eq. (2.30)), showing the two phonon branches in the first Brillouin zone.

### 2.2.2 Interaction of phonons with electromagnetic waves

Including the effects of a local electric field  $E$ , acting like an external force [28], into the equations of motion of the phonons (Eq. (2.26) and Eq. (2.27)) gives [29]

$$m \frac{d^2 x_p}{dt^2} = C(y_p + y_{p-1} - 2x_p) + e_Z E, \quad (2.31)$$

$$M \frac{d^2 y_p}{dt^2} = C(x_{p+1} + x_p - 2y_p) - e_Z E, \quad (2.32)$$

with  $e_Z$ , the effective charge (Born charge) [29, 32] of the ion. One can then neglect the position indices ( $p$ ) in the equations above by assuming that the wavelength of the lattice is much smaller than that of the electromagnetic wave [29] and rewrite the equations as,

$$\frac{d^2 x}{dt^2} = C(2y - 2x)/m + e_Z E/m, \quad (2.33)$$

$$\frac{d^2 y}{dt^2} = C(2x - 2y)/M - e_Z E/M. \quad (2.34)$$

The difference between these two equations is expressed as

$$\frac{d^2 x}{dt^2} - \frac{d^2 y}{dt^2} = -2C(x - y) \left( \frac{1}{m} + \frac{1}{M} \right) + e_Z E \left( \frac{1}{m} + \frac{1}{M} \right). \quad (2.35)$$

The property  $s$  is defined as  $s = x - y$  and the reduced mass,  $\mu$ , as

$$\frac{1}{\mu} = \frac{1}{m} + \frac{1}{M}. \quad (2.36)$$

Only optical modes can interact with electromagnetic waves. Thus, the expression of the frequency  $\omega_+$  at  $k = 0$  (Eq. (2.30)) is used to calculate the spring constant  $C = \omega_{+0}^2 \mu / 2$ . Now Eq. (2.35) becomes

$$\mu \frac{d^2 s}{dt^2} = -\mu \omega_{+0}^2 s + e_Z E, \quad (2.37)$$

giving the equation of motion describing the movement of the lattice with an applied electric field.

### 2.2.3 Dielectric function of phonons

The equation of motion, Eq. (2.37), is identical to Eq. (2.1) without damping (only using different labels). Damping is included to take care of scattering events such as from impurities. Thus the dielectric function is obtained by following the procedure described in Section 2.1:

$$\varepsilon(\omega) = \varepsilon_\infty + \frac{\omega_p^2}{\omega_T^2 - \omega^2 - i\omega\gamma}. \quad (2.38)$$

Now  $\varepsilon_\infty$  includes the additional effects from valence electrons and the independent phonon polarisations with  $\omega_T$  being the transverse optical frequency [29]. Longitudinal modes come into play, as one can write Eq. (2.38) with a common denominator

$$\varepsilon(\omega) = \varepsilon_\infty \frac{\omega_p^2/\varepsilon_\infty + \omega_T^2 - \omega^2 - i\omega\gamma}{\omega_T^2 - \omega^2 - i\omega\gamma}, \quad (2.39)$$

$$\varepsilon(\omega) = \varepsilon_\infty \frac{\omega_L^2 - \omega^2 - i\omega\gamma}{\omega_T^2 - \omega^2 - i\omega\gamma}, \quad (2.40)$$

with  $\omega_L^2 = \omega_p^2/\varepsilon_\infty + \omega_T^2$  being the longitudinal frequency.

A model with multiple phonon modes is realised by first setting up the equation of motion (Eq. (2.1)) for any individual vibration. Since the polarisation is then the sum of the polarisations of each single mode, the dielectric function becomes the sum of Lorentzian oscillators [29],

$$\varepsilon(\omega) = \varepsilon_\infty + \sum_i \frac{\omega_{p,i}^2}{\omega_i^2 - \omega^2 - i\omega\gamma_i}. \quad (2.41)$$

Now,  $\omega_{p,i}$  represents the plasma frequency of the  $i^{\text{th}}$  mode,  $\omega_i$  is its transverse frequency and  $\gamma_i$  is the damping constant.

## 2.3 Phonons as an indicator of structural stability: soft modes

The absence of lattice vibrations at non-real frequencies indicates a structure that should be stable against distortions [33]. However, if a mode is softening (its frequency shifts towards zero) this can represent a lattice instability [34]. Soft modes are therefore a well established indicator for a structural phase transition and are observed in a variety of materials [35–42].

### 2.3.1 Ferroelectric phase

Historically, a connection between zero frequency modes and ferroelectric (FE) transitions was proposed by Cochran [34]. The phenomenology of the ferroelectric phase (e.g. hysteresis loop of the polarisation, as shown in Figure 2.4) was first observed in Rochelle salt one hundred years ago [43]. Note that the ‘*ferro*’ in ferroelectric is given due to the analogous behaviour of the magnetic structure in a ferromagnetic compound, there is no need for iron in the crystal.

Cochran’s work deals with the connection between the dielectric function and the lattice vibrations in crystals [45]. In his model, the force on an ion of type  $i$  with charge  $q_i = e_0 Z_i$  (in harmonic approximation), due to short range restoring forces, is

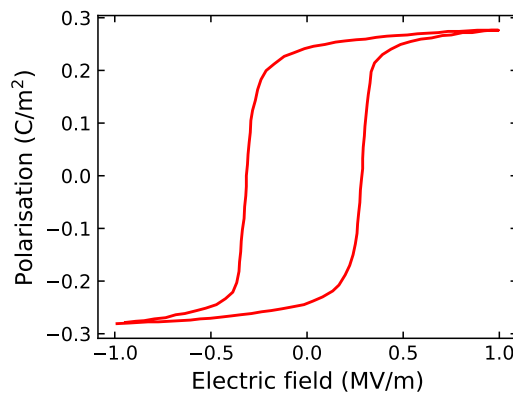


**Figure 2.4:** Ferroelectric hysteresis loop of a PMN-PT-BT actuator (data from [44]). One can see the similarity to the hysteresis of the magnetisation of a ferromagnetic material.

expressed as

$$F_i = - \sum_j R_{ij} x_j, \quad (2.42)$$

with displacement,  $x$ , and force constants  $R_{ij}$ . The second force acting on the ions is the Coulomb force,

$$F_{i,C} = e_0 Z_i E = q_i E. \quad (2.43)$$

$E$  represents the effective electric field, as defined on page 11. The equation of motion is now

$$m_i \frac{d^2 x}{dt^2} = - \sum_j R_{ij} x_j + q_i E. \quad (2.44)$$

The substitutions

$$x_i = X_i e^{i\omega t} \quad \text{and} \quad E = E_0 e^{i\omega t}, \quad (2.45)$$

yield

$$-m_i \omega^2 X_i = - \sum_j R_{ij} X_j + q_i E_0, \quad (2.46)$$

$$\omega^2 = \left( \sum_j R_{ij} X_j - q_i E_0 \right) / (m_i X_i). \quad (2.47)$$

Anharmonic effects in the lattice vibrations lead to a linear temperature dependency of  $R_{ij}$  and other properties in the electric field. This leads to Cochran's law<sup>5</sup> [34],

$$\omega^2 = A(T - T_C), \quad (2.48)$$

<sup>5</sup>I give a very naive derivation of Cochran's law. A more detailed expression of the Coulomb force was used in his publications [34, 46, 47], as expressions for the transverse optical frequency are taken from e.g. reference [48].

an approximation limited to  $T \sim T_C$ . One additional consideration is that the wavevector  $q$  approaches zero [34]. This corresponds to the wavelength being large compared to the size of the crystal's unit cell. The main result of Cochran's law is that the transverse optical frequency approaches zero at the critical temperature  $T_C$ .

A Curie-Weiss relation in the ferroelectric phase is given by [38]

$$\varepsilon(0) = \frac{C}{T - T_C} + \varepsilon_\infty, \quad (2.49)$$

with  $C$  being the Curie constant. In a diatomic lattice, this can be derived (for details see references [34, 46]) from the Lyddane-Sachs-Teller relation [49],

$$\frac{\varepsilon(0)}{\varepsilon_\infty} = \frac{\omega_L^2}{\omega_T^2}. \quad (2.50)$$

This equation states that  $\varepsilon(0) \rightarrow \infty$  for  $\omega_T \rightarrow 0$ . If the phase transition is of second order, the soft mode always softens completely, while for a first order transition this is possible, but not necessary [50].

Cochran claimed further that a spontaneous polarisation (“polarisation catastrophe”) can arise without a complete loss of stability, corresponding to a transition to another phase [34]. While there is no need for an external electric field to observe spontaneous polarisation, applying one can reverse the direction of the polarisation. This can be seen in the polarisation hysteresis loop [44], Figure 2.4. The shape of the hysteresis loop can provide information about the size of the sample's ferroelectric domain walls [51]. Two types of FE transitions can be distinguished: displacive (at  $T_C$ , a soft mode can propagate through the crystal) and order-disorder (the amplitude of the soft mode moves between the wells of the ordered and disordered state, the soft mode itself is non-propagating, thus no phonon corresponds to that mode) [31]. The polarisation is the order parameter of the transition.

Broken symmetries cause structural transitions. This can be observed in the lattice dynamics. Thus, I look for a mode softening to identify signatures of possible transitions.

### 2.3.2 Landau theory of phase transitions

The concept of an order parameter  $\eta$  leads straight to Landau's theory on second order phase transitions. Lev Landau [52–54] considered that the free energy  $F$  can be expressed as a power series of the order parameter for temperatures close to the critical temperature of the transition, typically written in the form

$$F(T, \eta) = F_0 + \alpha(T - T_C)\eta^2 + \frac{\beta}{2}\eta^4, \quad (2.51)$$

with the (positive) material constants  $\alpha$  and  $\beta$ . Odd powers of  $\eta$  can be neglected due to symmetry considerations. A linear term has to be included in the case of external fields. Figure 2.5(a) shows this approximation for three different temperatures. The

parabolic term is dominant for  $T > T_C$ , while at the critical temperature the first term vanishes, resulting in a much broader minimum. Thus, the relaxation time is larger for this potential. Below  $T_C$  the sign of the quadratic term changes, leading to a function with two minima. This picture describes only displacive transitions well, for order-disorder type an asymmetric function of the  $T < T_C$  free energy is necessary [31].

A further condition is that  $\eta$  vanishes in the high temperature phase. This can be verified easily by calculating the minimum in free energy via

$$\frac{\partial F}{\partial \eta} = (\alpha(T - T_C) + \beta\eta^2)2\eta = 0, \quad (2.52)$$

such that,

$$\eta = \sqrt{-\frac{\alpha}{\beta}(T - T_C)}. \quad (2.53)$$

The expression for  $\eta$  in Eq. (2.53) gives real values only for  $T < T_C$ , the low-temperature state. Thus, it follows that only  $\eta = 0$  is a minimum of the free energy in the high temperature state.

In general, this model can be easily adapted for first-order phase transitions. In this case,  $\beta$  in Eq. (2.51) has to be negative and a term with sixth order of  $\eta$  added [31, 50].

One can see in Figure 2.5(b) that this model gives an accurate description of the ferroelectric phase transition. In the paraelectric state, the order parameter polarisation vanishes. The spontaneous polarisation is only seen in the low temperature case. This model can also be used to characterise the antiferroelectric phase transition, that will be covered in more detail in Section 5.3.3. There, another order parameter will be introduced.

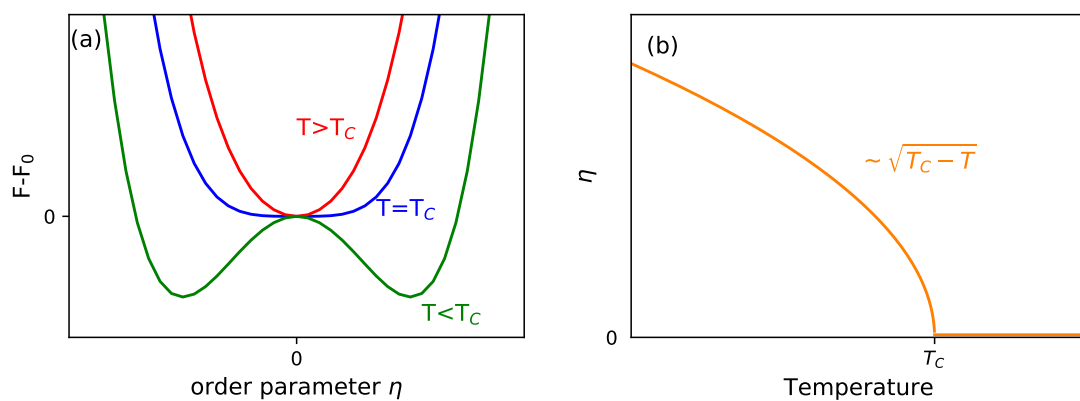


**Figure 2.5:** Landau free energy as a function of the order parameter  $\eta$  (a) and the order parameter  $\eta$  as a function of temperature (b).





---

# 3

## Experimental methods

---

An overview of the experiments implemented in my thesis is presented in this chapter. It focuses on Fourier transform infrared spectroscopy, as this type of spectrometer was mainly used. An introduction to quasi-optical THz spectroscopy and static measurement systems follows. The working principle of each of the experiments is described as well as the data acquisition and analysis process. The last section gives a comparison of the spectral working range of the different experimental setups and an introduction to the various units used in spectroscopy is provided.

### Contents

---

<b>3.1</b>	<b>Fourier transform infrared spectroscopy . . . . .</b>	<b>24</b>
3.1.1	Basic concept . . . . .	24
3.1.2	Components of the setup . . . . .	27
3.1.3	Data acquisition . . . . .	29
3.1.4	Kramers-Kronig analysis . . . . .	33
<b>3.2</b>	<b>Quasi-optical THz-spectroscopy . . . . .</b>	<b>39</b>
3.2.1	Mach-Zehnder interferometer . . . . .	40
3.2.2	Phase measurements and data processing . . . . .	42
<b>3.3</b>	<b>Physical Properties Measurement System . . . . .</b>	<b>44</b>
<b>3.4</b>	<b>Experimental spectral ranges and units . . . . .</b>	<b>45</b>

---

## 3.1 Fourier transform infrared spectroscopy

Large parts of the data presented in this thesis were obtained using a non dispersive spectroscopy method known as **F**ourier **T**ransform **I**nfra**R**ed spectroscopy (FTIR). The experiments have been performed using a Bruker 80v Vertex FTIR spectrometer (a picture is shown in Figure 3.1).

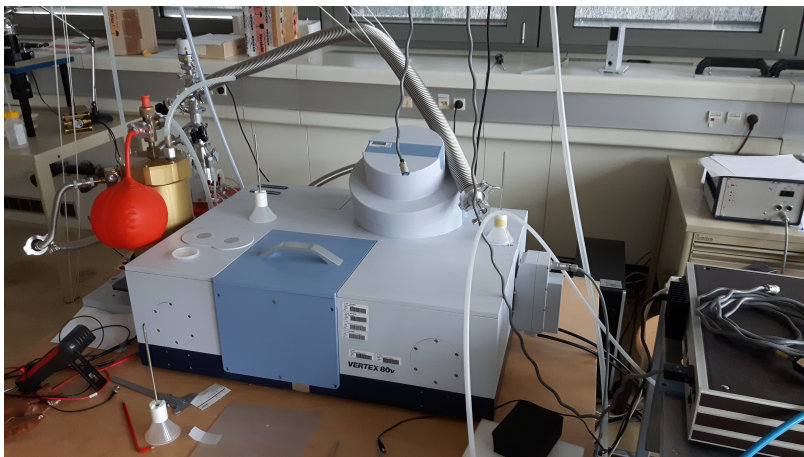


**Figure 3.1:** Photo of the FTIR spectrometer used throughout my thesis.

### 3.1.1 Basic concept

The most important component of an FTIR spectrometer is the interferometer. In our case, a so called Michelson interferometer is built into the spectrometer. Historically this arrangement is well known as it was a central part of the Michelson-Morley experiment to prove the Ether theory [55, 56]. It consists of a semitransparent mirror (the beam splitter, BMS) that splits the beam of an incident radiation source, guiding half the radiation to a static mirror and the other half to a moving mirror (see detailed sketch in Figure 3.2). Both mirrors reflect the light back to the beam splitter, where the two half-beams merge and interfere. In the case of monochromatic radiation with a wavelength  $\lambda$ , one can easily estimate that constructive interference occurs when the difference,  $x$ , in the optical path between the beam splitter and each of the mirrors is an integer ( $n$ ) multiple of the wavelength,  $n\lambda$ . Since light has to travel from the BMS to the mirror and back to the BMS,  $x$  is always twice as large as the movement of the mirror,  $d$ , from the zero position, where both interferometer arms have the same length (the point of Zero Path Difference (ZPD)). This is the intensity maximum. The intensity minimum occurs for  $x = (n + 0.5) \cdot \lambda$ . A measurement of the intensity as a function of  $x$  is called an interferogram. In the model case for monochromatic radiation, the interferogram is described by

$$I(x) = \frac{1}{2} \cdot I_0(\bar{\nu})[1 + \cos(2\pi\bar{\nu}x)], \quad (3.1)$$

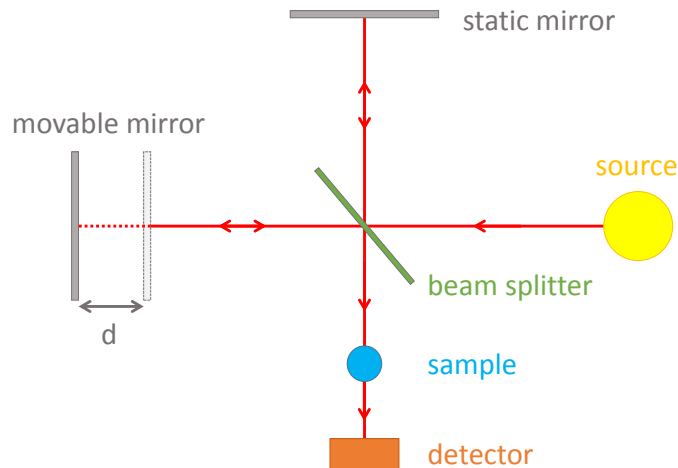


**Figure 3.2:** Beam path of an FTIR spectrometer with a Michelson interferometer for transmission measurements (details see text above).

with  $I(x)$  being the resulting signal as a function of the path difference and  $I_0(\bar{\nu})$  the radiation from the source. The property  $\bar{\nu}$  is the wavenumber,  $\bar{\nu} = 1/\lambda$ . For spectroscopic purposes, only the modulated part is relevant, hence the DC-part of the signal can be neglected [57]. Additionally, the wavenumber dependent efficiency of the optical elements, the detector and amplifier, must be included into the calculation (for details see [58]), so that the equation above can be rewritten as

$$S(x) = B(\bar{\nu}) \cos(2\pi\bar{\nu}x). \quad (3.2)$$

Now,  $S(x)$  is the detected signal and  $B(\bar{\nu})$  represents the real intensity including all characteristics of the spectrometer components. In practical application for broadband spectroscopy, we employ polychromatic radiation. Here the resulting interferogram is more complex. The detected signal then becomes the sum of all single wave intensities, for continuous sources this is given by the integral [58]

$$S(x) = \int_{-\infty}^{\infty} B(\bar{\nu}) \cos(2\pi\bar{\nu}x) d\bar{\nu}. \quad (3.3)$$

This equation shows that the connection between  $S(x)$  and  $B(\bar{\nu})$  is a Fourier cosine transform (the reason why this setup is called FTIR). The expression for  $B(\bar{\nu})$  as a function of the detector signal  $S(x)$  is then given by the re-transform

$$B(\bar{\nu}) = \int_{-\infty}^{\infty} S(x) \cos(2\pi\bar{\nu}x) dx. \quad (3.4)$$

Now the spectrum can be obtained from the measured detector signal. Since, in practice, the mirror retardation is limited to travel a finite distance in reality, a so called boxcar truncation function,  $D(x)$ , is included to compensate. This gives (see

reference [58] for more details)

$$B(\bar{\nu}) = \int_{-\infty}^{\infty} S(x) D(x) \cos(2\pi\bar{\nu}x) dx. \quad (3.5)$$

The movement of the mirror is always symmetric around the point of zero path difference. Scans can be performed independent of the direction of movement. Additionally, the resolution of the setup ( $\Delta\bar{\nu}$ ) is coupled to the maximum retardation,  $d_{max}$ , via [58]

$$\frac{1}{\Delta\bar{\nu}} = d_{max} = x_{max}/2. \quad (3.6)$$

Therefore, the resolution can be improved by extending the mirror retardation.

The radiation from a HeNe laser is also directed through the interferometer, coincident with the broadband radiation. Its signal is known to be monochromatic with a wavelength of 632.8 nm in the visible range (along with some weaker transitions, that can be neglected here). As described above, monochromatic radiation leads to a cosine signal after passing through the interferometer. By counting the minima in the laser signal as a function of the mirror motion, the mirror position can be determined (Eq. (3.2)) with a high accuracy, since the wavelength of the laser is known precisely. An FTIR spectrometer guides the radiation to a sample after passing it through the interferometer (see Figure 3.3).

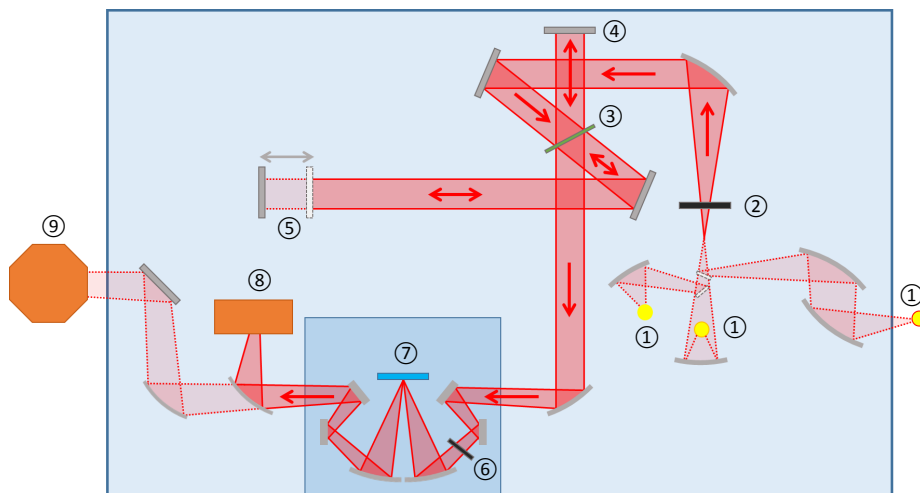


**Figure 3.3:** Beam path of the FTIR spectrometer with the Michelson interferometer used in this thesis. The components are labelled as ① sources (from left to right: NIR, MIR, FIR/THz), ② aperture, ③ beam splitter, ④ static mirror, ⑤ movable mirror, ⑥ polariser, ⑦ sample (the area in the darker blue is the sample compartment), ⑧ slot for internal detector, ⑨ bolometer detector.

The radiation interacts with the sample in two ways, reflection and transmission. The spectral response of the sample is encoded into the interferogram. Finally, the

reflected (or transmitted) beam is directed on to a detector and measured as a function of the moving mirror position. The data presented in this thesis has been obtained primarily in reflectivity mode. To ensure a near normal incidence (angle of incidence  $< 10^\circ$ ) an optical configuration shown in Figure 3.4 is used.

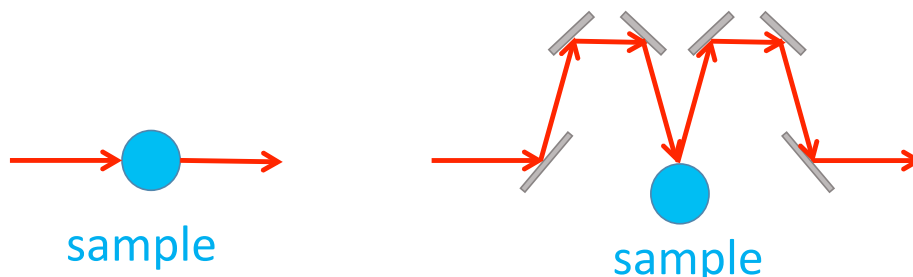


**Figure 3.4:** Beam path of transmission (left) and reflectivity (right) arrangements around the sample.

### 3.1.2 Components of the setup

In this section the different components of the FTIR spectrometer are described. Many of the components in an FTIR setup are optimised for specific bands in the electromagnetic spectrum. This requires the use of multiple sources, beam-splitters and detectors to cover a broad spectral width for experiments. Thus, measurements have to be performed in different settings covering individual working ranges:

- near infrared (NIR):  $8500 - 14000 \text{ cm}^{-1}$ ,
- mid infrared (MIR):  $600 - 7500 \text{ cm}^{-1}$ ,
- far infrared (FIR):  $40 - 650 \text{ cm}^{-1}$ ,
- terahertz (THz):  $20 - 50 \text{ cm}^{-1}$ .

A different combination of the components is necessary for each of these settings. These settings are named for their ranges across the electromagnetic spectrum, but they do not necessarily overlap with them exactly.

- **Lightsources:** Typically broadband sources are build within the experimental setup. For the visible and NIR settings, a tungsten lamp is used. A globalar is used for the MIR setting. This is a SiC rod, heated to  $1500^\circ\text{C}$ , emitting black body radiation [57]. For the FIR and THz settings we use a high pressure Hg lamp source.
- **Detectors:** A Si-diode detector is used in the visible and NIR regime. Here the incoming radiation creates electron-hole pairs in the semiconducting Si. The resulting photo-currents are measured as proportional to the radiation intensity. No external cooling is necessary. In the MIR range we use a DLaTGS (deuterated L-alanine doped triglycine sulfate) detector, while in the FIR range we use

a DTGS (deuterated triglycine sulfate) detector for quick room temperature test scans. The relevant principle of both detectors is the pyroelectric effect i.e. the incident radiation results in a change in temperature of the detector element that creates an electrical polarisation, generating a detectable electric current [57]. Both detectors operate without the need for active cooling.

A liquid nitrogen (LN<sub>2</sub>) cooled MCT-Detector (Mercury Cadmium Telluride (HgCdTe)) is used when more sensitivity is needed in the MIR range. Similar to the Si-Diode, the MCT detector directly converts the incident radiation into a detectable current.

In the FIR and THz ranges, a Si-Bolometer is used. An absorbing element (Silicon based) is connected to a thermal reservoir, filled with liquid helium (LHe, the LHe vessel is partially surrounded by a second vessel filled with LN<sub>2</sub>, to limit the LHe evaporation). The incident radiation raises the temperature of the absorbing element relative to the reservoir. The change in temperature results in a change in the resistivity of the detector element, which is detected as a change in the electrical current across the element [59]. The response time of the detector depends on the ratio of the heat capacity of the absorbing element and the thermal conductance between the absorbing element and the reservoir.

- Beam splitter (BMS): Here a CaF<sub>2</sub> crystal is used for the NIR setting. KBr is used for the MIR setting and Mylar of different thickness is used for the FIR and THz settings.

A polariser can be placed close to the sample to control the polarisation of the radiation incident on the sample (see Figure 3.3). An overview of the different components used in the FTIR spectrometer is given in Table 3.1. Figure 3.5 shows an overview of the working ranges of the different spectrometer settings.

Setting	Range (cm <sup>-1</sup> )	Source	BMS	Detector	Polariser
NIR	8500-14000	W-Lamp	CaF <sub>2</sub>	Si-Diode	Polymer Film
MIR	600-7500	Globalar	KBr	MCT (DLaTGS)	ZnSe
FIR	40-650	Hg-Lamp	Mylar Multilayer	Si-Bolometer (DTGS)	Polypropylene
THz	20-50	Hg-Lamp	Mylar 50μm	Si-Bolometer	Polypropylene

**Table 3.1:** Overview of the different FTIR spectrometer settings.

To perform measurements at lower temperatures, samples can be mounted in a He-flow cryostat. A picture is presented in Figure 3.6. Here, the mounts have two holes of the same diameter, such that the sample and gold-reference can be measured under identical conditions (see Figure 3.6). A step-motor is used to move the mount between the different positions. The cryostat is positioned in the spectrometer in place of the sample mount, only re-alignment of the mirrors in the sample compartment is necessary. At 10 K, the lowest stable temperature is reached. Due to the limitations

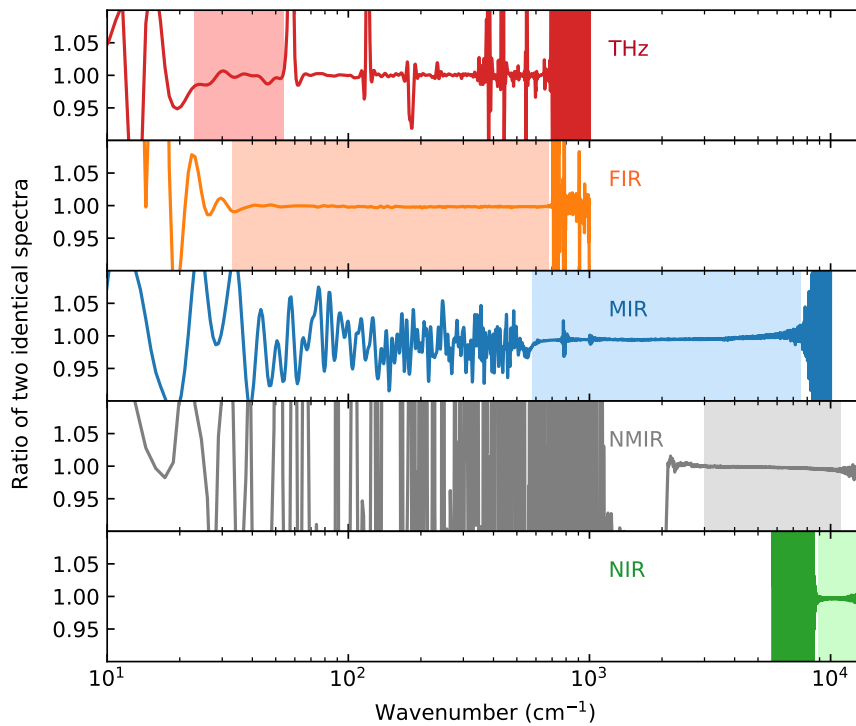


**Figure 3.5:** Effective bandwidth of the different spectral settings. A  $\text{Pr}_3\text{Ga}_5\text{SiO}_{14}$  crystal was measured in all the different settings between  $0\text{ cm}^{-1}$  and  $14\,000\text{ cm}^{-1}$ . Two measurements under identical conditions have been performed for all settings. In this plot the ratio of these two measurements is shown. The area in the background represents the working range of the individual setting. The gap between the MIR and NIR settings (from  $7500\text{ cm}^{-1}$  to  $8500\text{ cm}^{-1}$ ) can be filled with a measurement in an additional setting, named NMIR, covering the area between  $3000\text{ cm}^{-1}$  and  $11000\text{ cm}^{-1}$ . This is a combination of the NIR and MIR settings, using the MIR detectors and the NIR source and BMS. This setting was not used within the studies of my thesis.

of the cryostat windows (high transmittance is necessary) the spectral bands achievable at low temperatures are limited to the range of the FIR and THz settings.

### 3.1.3 Data acquisition

Our FTIR measurements aim to determine the absolute reflectance of the investigated sample. In the first step, the sample is fixed to the backside of a mount. This consists of a plate masked with abrasive SiC paper on the front side and a hole at the height of the beam. The sample has to be larger than the diameter of the hole and mounted in a way that it completely covers the hole. The mount is then inserted in the sample compartment of the spectrometer so that the abrasive paper side is illuminated by the radiation. This paper disperses light that would be reflected from surfaces other than the sample. Now the mirrors are aligned to maximise the reflected signal. Then



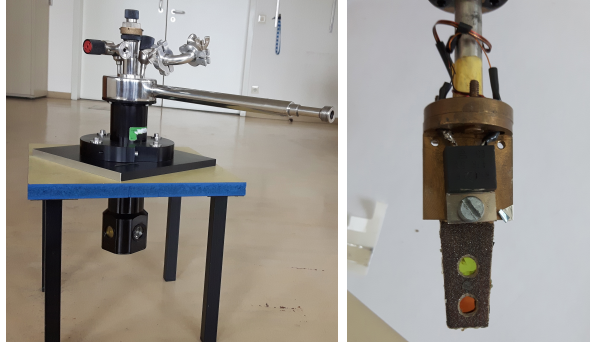


**Figure 3.6:** Picture of the cryostat (left) and the sample mount used within the cryostat (right). The  $\text{Pr}_3\text{Ga}_5\text{SiO}_{14}$  sample is fixed in the upper position of the mount, the gold mirror is in the lower position. The diameter of both holes is  $\sim 4$  mm each.

the spectrometer is evacuated (typically to  $\sim 2$  mbar), to reduce residual absorption from water molecules in the air.

The measurement process itself consists typically of 200 scans. Each one corresponds with the creation of an interferogram by one scan of the mirror. These interferograms are averaged, such that the resulting final interferogram is then Fourier transformed by the OPUS software to produce the spectrum (for more details see [60]). To ensure the uncertainty in the measurement is sufficiently low (a noise limit of  $\sim 3\%$  is chosen, as shown in Figure 3.5), two full measurements are performed under identical conditions and their ratio is calculated. If this condition is not fulfilled, realignment or changes in the setup (e.g. a higher number of scans) are necessary. After this, the sample is removed and replaced by a highly reflective gold mirror to produce a reference data set. Now it is crucial to avoid any changes in the beam path of the experiment (this means no realignment) to perform a measurement under the exact same conditions (details see Figure 3.7).

In general the reflectance  $R$  is defined by the ratio of light reflected by the sample ( $B_{sa}(\bar{\nu})$ ) to that of the incident light ( $B_{in}(\bar{\nu})$ ). The gold mirror is highly reflective (more than 97% [61]), so that for the reference spectrum one can assume

$$B_{Au}(\bar{\nu}) = B_{in}(\bar{\nu}). \quad (3.7)$$

Thus, the reflectance is given by the ratio of the sample spectrum and that of the gold-reference:

$$R(\bar{\nu}) = \left. \frac{B_{sa}(\bar{\nu})}{B_{in}(\bar{\nu})} \right|_{B_{Au}(\bar{\nu})=B_{in}(\bar{\nu})} = \frac{B_{sa}(\bar{\nu})}{B_{Au}(\bar{\nu})}. \quad (3.8)$$

The last step is to check the confidence limits. Here intervals with high noise due to weak signal intensity are omitted (Figure 3.8). For scans in different optical regimes with different settings, this procedure has to be repeated using the different settings of Table 3.1.



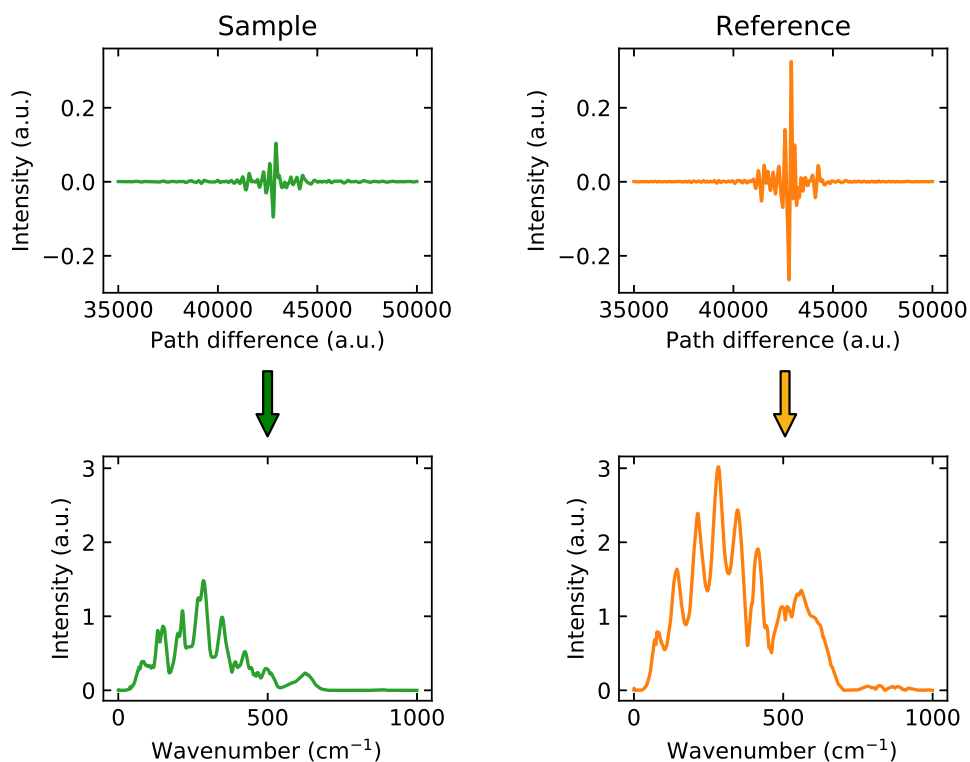


**Figure 3.7:** Example of a data set in the FIR regime. For both the sample and the reference, the FTIR measurement results in an independent interferogram (top). The frequency spectrum (bottom, here as a function of the wavenumber) is obtained after Fourier transform. The values for the path difference, signal and intensity are taken from an original data set and represent internal units of the Bruker spectrometer. The strong oscillations in the spectra are due to internal reflections in the beam splitter.

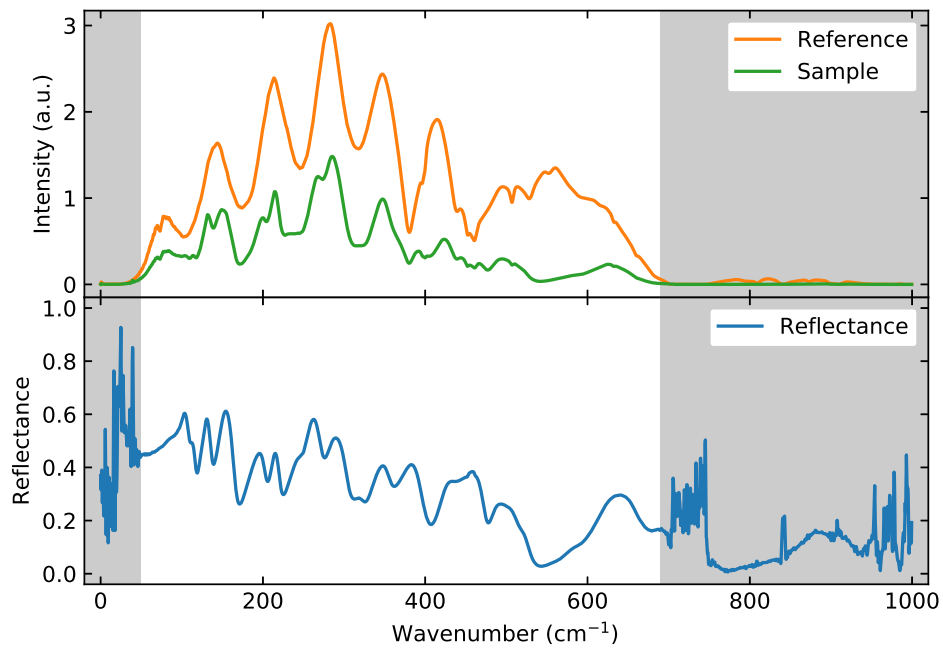


**Figure 3.8:** Calculation of the reflectance in the FIR region of the  $\text{Pr}_3\text{Ga}_5\text{SiO}_{14}$  sample used in Figure 3.7 by dividing the sample spectrum with the gold reference. One can see that the oscillations of the beam splitter vanish. The grey range (less than  $\sim 40 \text{ cm}^{-1}$  and above  $\sim 650 \text{ cm}^{-1}$ ) shows the area where the data of this setting should not be used due to a low signal to noise ratio.

### 3.1.4 Kramers-Kronig analysis

In the following, the procedure for calculating the dielectric function  $\varepsilon(\bar{\nu})$  from the available  $R(\bar{\nu})$  data is described. The procedure uses linear response theory to formulate the Kramers-Kronig (KK) relations [62, 63]. These famous relations connect the real part of a complex function with the imaginary one. In the first step, the general equations will be derived following the example of references [28, 29, 64, 65]. The KK-analysis is one of the standard methods for calculating the dielectric function from reflectance measurements and is applied to a broad range of materials e.g. [66–77].

In a linear and isotropic medium, the most general connection between a stimulus  $\mathbf{f}$  (e.g. electric field  $\mathbf{E}$ ) and the response  $\mathbf{X}$  (e.g. displacement field  $\mathbf{D}$ ) with the response function  $G$  (e.g. dielectric function  $\varepsilon$ ) is given by [28]

$$\mathbf{X}(\mathbf{r}, t) = \int d^3r' \int_{-\infty}^{\infty} dt' G(\mathbf{r}, \mathbf{r}', t, t') \mathbf{f}(\mathbf{r}', t'). \quad (3.9)$$

The following assumptions can be made for simplification [28]:

- Spatial locality:  $\mathbf{X}(\mathbf{r}, t)$  depends on  $\mathbf{f}(\mathbf{r}', t')$  only if  $\mathbf{r} = \mathbf{r}'$ , so that the response function can be rewritten as  $G(\mathbf{r}, \mathbf{r}', t, t') = G(t, t') \cdot \delta(\mathbf{r} - \mathbf{r}')$ . Execution of the spacial integration in Eq. (3.9) leads to

$$\int d^3r' \delta(\mathbf{r} - \mathbf{r}') \mathbf{f}(\mathbf{r}', t') = \mathbf{f}(\mathbf{r}, t'). \quad (3.10)$$

- Relative time: The absolute time  $t$  is not important, only the time difference  $t - t'$ . So  $G(t, t') = G(t - t')$  and Eq. (3.9) can be modified to

$$\mathbf{X}(\mathbf{r}, t) = \int_{-\infty}^{\infty} dt' G(t - t') \mathbf{f}(\mathbf{r}, t'). \quad (3.11)$$

- Causality: The response  $\mathbf{X}(\mathbf{r}, t)$  cannot be influenced by a future stimulus  $\mathbf{f}(\mathbf{r}, t')$  with  $t' > t$ . So  $G(t - t') = 0$  for  $t < t'$ .

The KK algorithm works in frequency space with  $\omega = \omega_1 + i\omega_2$  being a complex number. A Fourier transform converts the spacial dependency to the frequency domain and is defined as [28]

$$X(\mathbf{r}, \omega) = \int_{-\infty}^{\infty} dt \mathbf{X}(\mathbf{r}, t) e^{i\omega t}, \quad (3.12)$$

$$f(\mathbf{r}, \omega) = \int_{-\infty}^{\infty} dt \mathbf{f}(\mathbf{r}, t) e^{i\omega t}, \quad (3.13)$$

$$G(\omega) = \int_{-\infty}^{\infty} dt G(t - t') e^{i\omega(t-t')}. \quad (3.14)$$

From Eq. (3.14) one can see that [64]

$$G^*(\omega) = G(-\omega), \quad (3.15)$$

and further that  $G_1(\omega)$ , the real part of  $G(\omega)$  must be an even function in  $\omega$ , while the imaginary part,  $G_2(\omega)$ , is odd:

$$G_1(-\omega) = G_1(\omega) \text{ and } G_2(-\omega) = -G_2(\omega). \quad (3.16)$$

Inserting the expression for  $\mathbf{X}(\mathbf{r}, t)$  of Eq. (3.11) into Eq. (3.12) leads to

$$X(\mathbf{r}, \omega) = \int_{-\infty}^{\infty} dt \int_{-\infty}^{\infty} dt' G(t-t') \mathbf{f}(\mathbf{r}, t') e^{i\omega t}, \quad (3.17)$$

$$= \int_{-\infty}^{\infty} dt \int_{-\infty}^{\infty} dt' G(t-t') \mathbf{f}(\mathbf{r}, t') e^{i\omega t} \underbrace{e^{i\omega t'} e^{-i\omega t'}}_{=1}, \quad (3.18)$$

$$= \int_{-\infty}^{\infty} dt' \mathbf{f}(\mathbf{r}, t') \underbrace{\int_{-\infty}^{\infty} dt G(t-t') e^{i\omega(t-t')} e^{i\omega t'}}_{=G(\omega)}, \quad (3.19)$$

$$= G(\omega) \underbrace{\int_{-\infty}^{\infty} dt' \mathbf{f}(\mathbf{r}, t') e^{i\omega t'}}_{=f(\mathbf{r}, \omega)}, \quad (3.20)$$

and finally to the following linear equation between stimulus and response in the frequency domain

$$X(\mathbf{r}, \omega) = G(\omega) f(\mathbf{r}, \omega). \quad (3.21)$$

To deal with the issue of integrating across the pole at  $\omega' = (\omega, 0)$  we implement Cauchy's integral theorem [78] of the form:

$$\oint_{\Gamma} d\omega' \frac{G(\omega')}{\omega' - \omega} = 0, \quad (3.22)$$

with  $\Gamma$  being an arbitrary closed curve in the upper-half plane in the complex  $\omega'$  space [29].

For the derivation of the KK equations, usually the contour plotted in Figure 3.9 is chosen [28, 64]. This curve consists of 4 segments. Part ① is along the real axis from  $-\infty$  to  $(\omega - a)$ . Part ② is represented by an infinitesimal semicircle in the upper-half plane with radius  $a$  around the pole at  $\omega' = (\omega, 0)$ . Part ③ is along the positive real axis running from  $(\omega + a)$  to  $+\infty$ . Part ④ closes the contour, it is also a semicircle in the upper-half plane, but with a radius of infinity. Now the contour integral in Eq. (3.22) can be split into 4 integrals along the 4 parts of  $\Gamma$ :

$$\int_{\textcircled{1}} d\omega' \frac{G(\omega')}{\omega' - \omega} + \int_{\textcircled{2}} d\omega' \frac{G(\omega')}{\omega' - \omega} + \int_{\textcircled{3}} d\omega' \frac{G(\omega')}{\omega' - \omega} + \int_{\textcircled{4}} d\omega' \frac{G(\omega')}{\omega' - \omega} = 0. \quad (3.23)$$

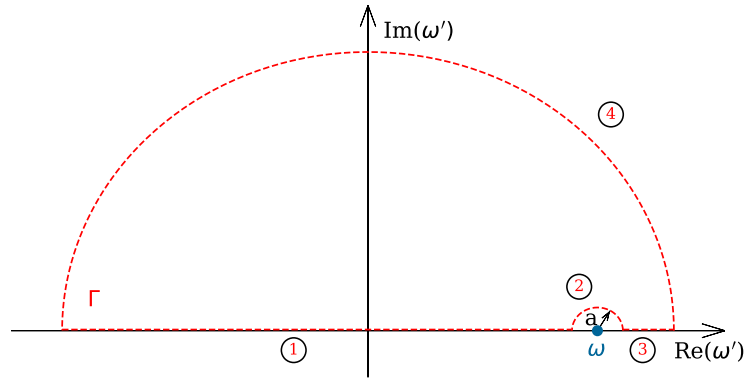


**Figure 3.9:** Plot of the integration path  $\Gamma$  (red dashed line) composed out of the four segments ① to ④ in the complex  $\omega'$ -space.

- Part ④: Since [29]

$$G(\omega') \rightarrow 0 \text{ for } |\omega'| \rightarrow \infty, \quad (3.24)$$

with at least a  $1/\omega'$  dependence,

$$\frac{G(\omega')}{\omega' - \omega}, \quad (3.25)$$

has to vanish assuming an infinitely large radius of the integral.

- Part ②: The function  $G(\omega')$  is constant for all  $\omega'$  along ②, when the radius of the infinitesimal semicircle  $a \rightarrow 0$ , it can be approximated<sup>6</sup> as  $G(\omega)$  [29]. Curve ② will be described with  $\omega' = \omega + a \cdot e^{i\alpha}$ . Here  $\alpha$  represents the angle between the actual radius vector and the positive real  $\omega'$  axis, running from  $\pi$  to 0. Furthermore  $d\omega' = i\alpha a \cdot e^{i\alpha} d\alpha$  and  $1/(\omega' - \omega) = 1/(a \cdot e^{i\alpha})$ . Calculating the integral now leads to [29]

$$\int_{\textcircled{2}} d\omega' \frac{G(\omega')}{\omega' - \omega} = \int_{\pi}^0 d\alpha G(\omega) \frac{i a e^{i\alpha}}{a e^{i\alpha}} = iG(\omega) \alpha \Big|_{\pi}^0 = -i\pi G(\omega). \quad (3.26)$$

- Part ① and ③: The integrals along the real  $\omega'$  axis for  $a \rightarrow 0$  are given as:

$$\int_{\textcircled{1}} d\omega' \frac{G(\omega')}{\omega' - \omega} + \int_{\textcircled{3}} d\omega' \frac{G(\omega')}{\omega' - \omega} = \lim_{a \rightarrow 0} \int_{-\infty}^{\omega-a} d\omega' \frac{G(\omega')}{\omega' - \omega} + \lim_{a \rightarrow 0} \int_{\omega+a}^{\infty} d\omega' \frac{G(\omega')}{\omega' - \omega}. \quad (3.27)$$

Now the limits of the right side of Eq. (3.27) are grouped together, and one can

<sup>6</sup>The mathematically clean way is to calculate the residuum [64].

see that this is equal to Cauchy's principal value  $\mathcal{P}$  of the integral [64],

$$\lim_{a \rightarrow 0} \left[ \int_{-\infty}^{\omega-a} d\omega' \frac{G(\omega')}{\omega' - \omega} + \int_{\omega+a}^{\infty} d\omega' \frac{G(\omega')}{\omega' - \omega} \right] = \mathcal{P} \int_{-\infty}^{\infty} d\omega' \frac{G(\omega')}{\omega' - \omega}. \quad (3.28)$$

Summing up the remaining results of all segments gives:

$$-i\pi G(\omega) + \mathcal{P} \int_{-\infty}^{\infty} d\omega' \frac{G(\omega')}{\omega' - \omega} = 0, \quad (3.29)$$

and after rearrangement,

$$G(\omega) = \frac{1}{i\pi} \mathcal{P} \int_{-\infty}^{\infty} d\omega' \frac{G(\omega')}{\omega' - \omega}. \quad (3.30)$$

Now inserting  $G(\omega) = G_1(\omega) + iG_2(\omega)$  into Eq. (3.30) and multiplying with  $i$  gives

$$iG_1(\omega) - G_2(\omega) = \frac{1}{\pi} \mathcal{P} \int_{-\infty}^{\infty} d\omega' \frac{G_1(\omega')}{\omega' - \omega} + \frac{i}{\pi} \mathcal{P} \int_{-\infty}^{\infty} d\omega' \frac{G_2(\omega')}{\omega' - \omega}. \quad (3.31)$$

This equation must be valid for its real and imaginary part simultaneously, finally leading to the Kramers-Kronig relations,

$$G_1(\omega) = \frac{1}{\pi} \mathcal{P} \int_{-\infty}^{\infty} d\omega' \frac{G_2(\omega')}{\omega' - \omega}, \quad (3.32)$$

and

$$G_2(\omega) = -\frac{1}{\pi} \mathcal{P} \int_{-\infty}^{\infty} d\omega' \frac{G_1(\omega')}{\omega' - \omega}. \quad (3.33)$$

A first modification is to remove the (non-existing) negative frequencies from the integration limits by multiplying the numerator and denominator in both equations with  $(\omega' + \omega)$  and splitting the integrals up into two parts with  $\omega'$  and  $\omega$  in the numerator respectively [29]:

$$G_1(\omega) = \frac{1}{\pi} \mathcal{P} \int_{-\infty}^{\infty} d\omega' \frac{\omega' G_2(\omega')}{\omega'^2 - \omega^2} + \underbrace{\frac{\omega}{\pi} \mathcal{P} \int_{-\infty}^{\infty} d\omega' \frac{G_2(\omega')}{\omega'^2 - \omega^2}}_{=0}, \quad (3.34)$$

$$G_2(\omega) = -\frac{1}{\pi} \mathcal{P} \int_{-\infty}^{\infty} d\omega' \frac{\omega' G_1(\omega')}{\omega'^2 - \omega^2} - \frac{\omega}{\pi} \mathcal{P} \int_{-\infty}^{\infty} d\omega' \frac{G_1(\omega')}{\omega'^2 - \omega^2}. \quad (3.35)$$

As mentioned before (Eq. (3.16)),  $G_1(\omega)$  is an even function in frequency and  $G_2(\omega)$  is odd. This argument cancels out the second integral in Eq. (3.34) and the first one in Eq. (3.35) ( $\omega' G_1(\omega')$  is odd), since a symmetric integration of an odd integrand is equal to 0. Integrating an even function (here the nominators  $\omega' G_2(\omega')$  and  $G_1(\omega')$ ) in the range  $(-\infty, 0)$  is equal to integrating over the range  $(0, \infty)$ . Thus the Kramers-

Kronig relations are given by

$$G_1(\omega) = \frac{2}{\pi} \mathcal{P} \int_0^\infty d\omega' \frac{\omega' G_2(\omega')}{\omega'^2 - \omega^2}, \quad (3.36)$$

$$G_2(\omega) = -\frac{2\omega}{\pi} \mathcal{P} \int_0^\infty d\omega' \frac{G_1(\omega')}{\omega'^2 - \omega^2}. \quad (3.37)$$

These equations show the KK relations in their general form. To proceed further with analysing the reflectance data, a specialised form in  $R(\omega)$  is needed. Remember that  $R(\omega) = r(\omega)r(\omega)^*$  with

$$r(\omega) = \rho(\omega)e^{i\varphi(\omega)}, \quad (3.38)$$

so  $\rho(\omega) = \sqrt{R(\omega)}$ . Now applying the logarithm on the equation above, the complex property is split, and the real and imaginary parts are separated:

$$\ln r(\omega) = \ln \rho(\omega) + i\varphi(\omega). \quad (3.39)$$

The reflectivity,  $r$  (and so  $\ln r$ ), fulfils all requirements (e.g. causality and  $r^*(\omega) = -r(\omega)$ ) made for  $G(\omega)$  so far [28], so that inserting it into the general KK-relations (Eq. (3.36) and Eq. (3.37)) yields the KK-relations for reflectivity and phase:

$$\ln \rho(\omega) = \frac{2}{\pi} \mathcal{P} \int_0^\infty d\omega' \frac{\omega' \varphi(\omega')}{\omega'^2 - \omega^2}, \quad (3.40)$$

$$\varphi(\omega) = -\frac{2\omega}{\pi} \mathcal{P} \int_0^\infty d\omega' \frac{\ln \rho(\omega')}{\omega'^2 - \omega^2}. \quad (3.41)$$

Additionally, one improvement can be made by first setting [28, 77]

$$\mathcal{P} \int_0^\infty d\omega' \frac{1}{\omega'^2 - \omega^2} = 0, \quad (3.42)$$

so that

$$\frac{2\omega}{\pi} \ln \rho(\omega) \mathcal{P} \int_0^\infty d\omega' \frac{1}{\omega'^2 - \omega^2}, \quad (3.43)$$

which is also cancelled out, can be added to the right side of Eq. (3.41). Now the phase is given by

$$\varphi(\omega) = \frac{2\omega}{\pi} \mathcal{P} \int_0^\infty d\omega' \frac{\ln \rho(\omega) - \ln \rho(\omega')}{\omega'^2 - \omega^2}. \quad (3.44)$$

Since

$$\ln \rho(\omega) = \ln \sqrt{R(\omega)} = \ln R(\omega)/2, \quad (3.45)$$

the phase equation above can be rewritten as

$$\varphi(\omega) = -\frac{\omega}{\pi} \mathcal{P} \int_0^\infty d\omega' \frac{\ln R(\omega') - \ln R(\omega)}{\omega'^2 - \omega^2}. \quad (3.46)$$

This equation for  $\varphi$  now has two advantages [77]:

- Constant errors of  $R(\omega)$  are cancelled out and do not influence the phase any more.
- For  $\omega' = \omega$  both numerator and denominator become 0. According to the rule of de l'Hospital it can be shown<sup>7</sup>, that there is no divergence any more, such that the pole is removed and Cauchy's principal value,  $\mathcal{P}$ , is not necessary any more.

Hence, the phase,  $\varphi(\omega)$ , can easily be calculated by solving the integral [77, 79]

$$\varphi(\omega) = -\frac{\omega}{\pi} \int_0^\infty d\omega' \frac{\ln R(\omega') - \ln R(\omega)}{\omega'^2 - \omega^2}. \quad (3.47)$$

Now the real and imaginary part of the refractive index can be calculated<sup>8</sup> [79] as:

$$n(\omega) = \frac{1 - R(\omega)}{1 + R(\omega) - 2\sqrt{R(\omega)} \cos \varphi(\omega)}, \quad (3.48)$$

$$k(\omega) = \frac{2\sqrt{R(\omega)} \sin \varphi(\omega)}{1 + R(\omega) - 2\sqrt{R(\omega)} \cos \varphi(\omega)}. \quad (3.49)$$

---

7

$$\frac{\frac{d}{d\omega'} [\ln(R(\omega') - \ln(R(\omega)))]}{\frac{d}{d\omega'} [\omega'^2 - \omega^2]} \Big|_{\omega'=\omega} = \frac{1}{R(\omega')} \frac{dR(\omega')}{d\omega'} \Big|_{\omega'=\omega}$$

<sup>8</sup>Assuming [79]

$$r = \frac{N - 1}{N + 1},$$

we find the following expression for the refractive index

$$N = \frac{1 + r}{1 - r},$$

with

$$r = \rho e^{i\varphi} = \rho(\cos \varphi + i \sin \varphi) = \rho c + i \rho s.$$

Inserting the expression for  $r$  into the equation above yields (in step one both nominater and denominator are multiplied with the complex conjugate of the denominator to remove the imaginary part),

$$N = \frac{1 + \rho c + i \rho s}{1 - \rho c - i \rho s} = \frac{(1 + \rho c + i \rho s) \cdot (1 - \rho c + i \rho s)}{(1 - \rho c)^2 + \rho^2 s^2} = \frac{1 + \rho c + i \rho s - \rho c - \rho^2 c^2 - i \rho^2 c s + i \rho s + i \rho^2 c s - \rho^2 s^2}{1 - 2\rho c + \rho^2 c^2 + \rho^2 s^2}.$$

Using  $\cos^2 + \sin^2 = 1$  this gives

$$\frac{1 - \rho^2 + i 2 \rho s}{1 - 2\rho c + \rho^2} = \frac{1 - \rho^2}{1 - 2\rho c + \rho^2} + i \frac{2 \rho s}{1 - 2\rho c + \rho^2} = n + i k = N.$$

The expression has to be valid for its **real** and **imaginary** part, resulting with  $R = r r^* = \rho^2$  in Eq. (3.48) and (3.49).



Finally the real and imaginary part of the dielectric function can be calculated using the refractive index via  $\varepsilon(\omega) = N(\omega)^2$  so that<sup>9</sup> [79]:

$$\varepsilon_1(\omega) = n(\omega)^2 - k(\omega)^2, \quad (3.50)$$

$$\varepsilon_2(\omega) = 2n(\omega)k(\omega). \quad (3.51)$$

In this derivation, the frequency  $\omega$  was used. The linear relation  $\bar{\nu} = \omega/(2\pi c)$  between frequency and wavenumber states that all equations can be used without further changes when using wavenumbers. In general, with Eq. (3.47), one can calculate the phase and therefore the dielectric function for any wavenumber. Things get complicated as the integration runs from 0 to infinity and the measurement of  $R(\bar{\nu})$  is of course finite in the frequency domain. The FTIR spectrometer used in this thesis can provide data roughly in a range between  $25 \text{ cm}^{-1}$  and  $14000 \text{ cm}^{-1}$ . Therefore, approximations are necessary to deal with this algorithm (see details in the results chapters). Now, the integration limit is set to a finite number  $\bar{\nu}_{max}$  so that

$$\varphi(\bar{\nu}) = -\frac{\bar{\nu}}{\pi} \int_0^{\bar{\nu}_{max}} d\bar{\nu}' \frac{\ln R(\bar{\nu}') - \ln R(\bar{\nu})}{\bar{\nu}'^2 - \bar{\nu}^2}, \quad (3.52)$$

with a value chosen to be  $15000 \text{ cm}^{-1}$  for the investigated materials. This value is above any interesting observable feature and typically in a range of constant reflectance.

Due to misalignment or non perfect sample / reference surfaces, a complete spectrum can be erroneously offset. Wrong  $\varepsilon(0)$  values are an indicator for this behaviour. Measurements performed in the cryostat especially tend to feature this effect. In this case the reflectance data must be rescaled with a constant scaling factor, so that the correct value for the dielectric function can be achieved. For more details on this aspect, see the results chapters.

## 3.2 Quasi-optical THz-spectroscopy

This THz setup is used to investigate samples in the spectral ranges below the lower detection frequency limit of the FTIR spectrometer. In contrast, experiments here are performed in transmission. A speciality of this self-constructed spectrometer is the possibility of phase sensitive measurements. In this spectral regime optical elements, such as lenses, are made out of materials such as polyethylene.

<sup>9</sup>All functions depend on the frequency (not written):

$$\varepsilon = \varepsilon_1 + i\varepsilon_2 = N^2 = (n + ik)^2 = n^2 - k^2 + i2nk.$$

The expression has to be valid for its **real** and **imaginary** part, resulting in Eq. (3.50) and (3.51),

$$\varepsilon_1 = n^2 - k^2 \quad \text{and} \quad \varepsilon_2 = 2nk.$$

### 3.2.1 Mach-Zehnder interferometer

The main part of this experimental setup is a Mach-Zehnder interferometer [80, 81]. The beam path is shown in Figure 3.10. Backward wave oscillators (BWO, Figure 3.11) are used as monochromatic radiation sources, that can be approximated as point-like sources [82, 83]. Backward wave oscillators consist of a vacuum tube, with a voltage of a few kV applied between anode and cathode. Thus, electrons are emitted from the cathode and form a beam by interacting with an external magnetic field that guides them over a slow wave structure (grid). Radiation is created due to the interaction of the electron beam with the periodic electric field of this grid structure. The direction of the emitted radiation is opposite to the electron beam. Thus, these sources are called backward wave oscillators. Backward wave oscillators are frequency tunable across a limited range by sweeping the applied voltage, so the speed of the electrons can be changed. In total ten separate BWO devices are necessary to cover the total frequency range between 39 GHz and 1080 GHz. Two of them (BWO 530 and BWO 800) are chosen for experiments presented in this thesis (see Figure 3.11).

In the setup, a lens is first used to tailor the beam shape from diverging to parallel. The beam is then guided to an attenuator, to reduce the intensity if necessary. Four different settings are possible between 1 % and 30 % transmission (and without attenuation). A wire grid polariser is used as a beam splitter, dividing the radiation into a sample and reference arm. The polariser reflects radiation with its electric field parallel to the grid and passes radiation with a polarisation perpendicular to the grid. Thus, the polarisation of the reference arm is shifted by  $90^\circ$  relative to the sample arm. To obtain the same intensity in both arms, another polariser is put in front of the beam splitter and rotated until the signals are the same.

An Oxford Instruments cryomagnet is located in the sample arm. This allows measurements to be performed in a temperature range between 2 K and room temperature with the addition of magnetic fields up to 7 T. The cryomagnet's inner windows are made out of  $\sim 50 \mu\text{m}$  thick Polypropylene, while the outer ones are made of Mylar, both materials that are highly transparent in the frequency range of the BWO sources. The sample is located in the middle of the magnet on a horizontally moveable mount with two mounting positions. The second position of the sample mount remains empty and is used for calibration scans (see Figure 3.11). Two lenses are placed before and after the cryomagnet to focus the beam onto the sample and defocus afterwards. The last device in the sample arm is an electrically movable mirror, necessary for phase sensitive measurements (see Section 3.2.2).

An oscillating mirror is placed in the reference arm, providing modulation for lock-in assisted detection. Two lenses are mounted with the same distance as those of the sample arm in order to compensate the additional phase of the sample arm.

A second grid polariser is used to merge the two beams. There is a  $90^\circ$  difference in the polarisation of the two beams due to the beam splitter. Therefore, a final polariser is required to rotate both beams by  $45^\circ$  to bring them into antiparallel orientation so that they can interfere correctly. Finally, the light is focussed on the detector, which is a LHe cooled bolometer identical to the one described in the FTIR

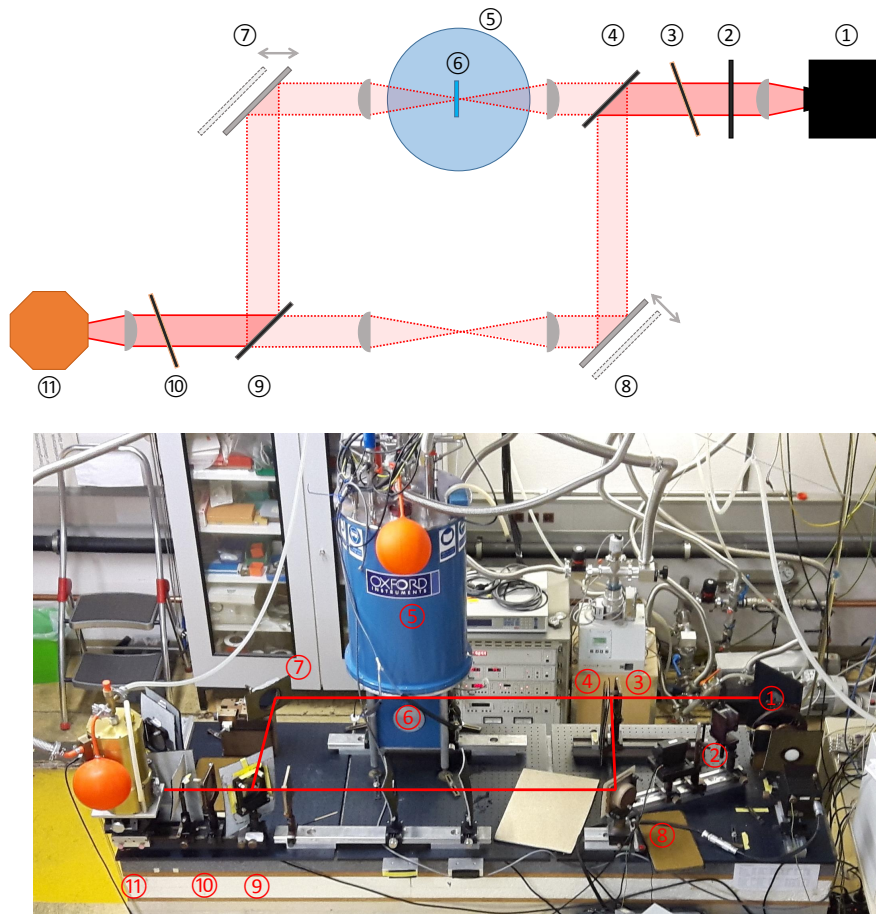


**Figure 3.10:** Beam path (top) and photo (bottom) of the Mach-Zehnder interferometer. The labels indicate: ① source (BWO), ② attenuator, ③ polariser, ④ beam splitter, ⑤ cryo-magnet, ⑥ sample, ⑦ stabilising mirror, ⑧ phase modulating mirror, ⑨ wire-grid as merger, ⑩ polariser, ⑪ bolometer.

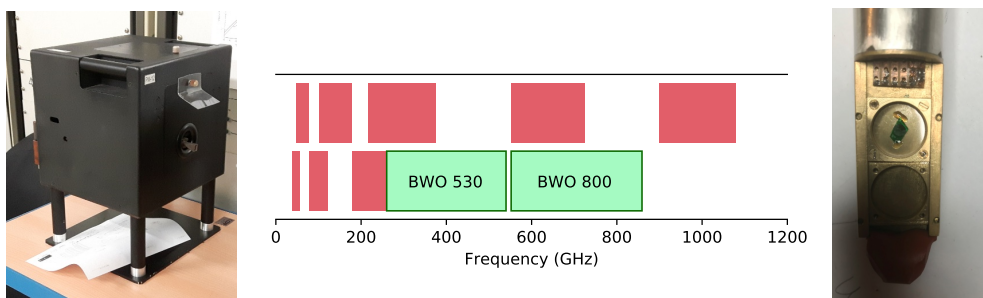


**Figure 3.11:** From left to right: image of BWO; working ranges of the different BWOs (the sources used for this thesis are highlighted in green); sample mount.

spectroscopy section (page 27).

### 3.2.2 Phase measurements and data processing

The signal detected in the bolometer is given by the interference of the sample and reference arm beams:

$$I = |\hat{E}_S - \hat{E}_R|^2 = |E_S e^{i(\varphi_S + \omega t)} - E_R e^{i(\varphi_R + \omega t)}|^2, \quad (3.53)$$

$$= E_S^2 + E_R^2 - E_S E_R (e^{i(\varphi_S - \varphi_R)} + e^{-i(\varphi_S - \varphi_R)}), \quad (3.54)$$

$$= E_S^2 + E_R^2 - 2E_S E_R \cos(\varphi_S - \varphi_R), \quad (3.55)$$

with  $\hat{E}$  being the complex electric field (with amplitude  $E$  and phase angle  $\varphi$ ) and the subscripts  $S$  and  $R$  representing the sample and reference arms, respectively. The negative sign is due to the special choice of the angle of the last polariser before the detector.  $E_S^2$  and  $E_R^2$  can be omitted, since the amplitudes are assumed to be constant over time and thus are not detected by the bolometer. The detected signal can now be described by

$$I_{det} = -2E_S E_R \cos(\underbrace{\varphi_S - \varphi_R}_{\Delta\varphi_0}). \quad (3.56)$$

The phase shift in the sample arm of the interferometer is given by

$$\varphi_S = \varphi_0 + \varphi_t, \quad (3.57)$$

where  $\varphi_t$  is the phase shift incurred by the sample and  $\varphi_0$  is the phase shift gained by travelling along the other parts of the interferometer. The equation for the reference arm is similar,

$$\varphi_R = \varphi_0 + \frac{2\pi\omega}{c}d, \quad (3.58)$$

with the second part describing the phase shift of radiation with frequency  $\omega$  passing through a slice of air with thickness  $d$ , equivalent to the thickness of the sample (effectively an imaginary sample of the same thickness). Thus, the phase difference between the two arms is given by

$$\Delta\varphi_0 = \varphi_t - \frac{2\pi\omega}{c}d. \quad (3.59)$$

Now, the two movable mirrors come into play, the phase modulating mirror in the reference arm and a phase stabilizing mirror in the sample arm. The displacement,  $\Delta l$ , of the motorised mirror in the sample arm leads to an additional phase change. So the total phase shift of this half-beam is

$$\varphi_S = \varphi_0 + \varphi_t - \frac{2\pi\omega}{c}\Delta l. \quad (3.60)$$

In order for the automatic phase stabilisation to work, an additional modulating mirror is necessary as part of a lock-in amplifier detection system. This mirror oscillates with a frequency  $\Omega \sim 28$  Hz and an amplitude  $a$ . Thus the term

$$\varphi_\Omega = \frac{2\pi\omega}{c} a \cos(\Omega t) = \delta \cos(\Omega t), \quad (3.61)$$

is included to the phase of the reference arm. So the phase difference between the two arms is expressed by

$$\varphi_S - \varphi_R = \varphi_\Omega + \varphi_t - \frac{2\pi\omega}{c} d - \frac{2\pi\omega}{c} \Delta l = \varphi_\Omega + \Delta\varphi. \quad (3.62)$$

Inserting this into the expression for the detected intensity (Eq. (3.56)) gives

$$I_{det} = -2E_S E_R \cos(\Delta\varphi + \varphi_\Omega), \quad (3.63)$$

$$= -2E_S E_R (\cos(\Delta\varphi) \cos(\varphi_\Omega) - \sin(\Delta\varphi) \sin(\varphi_\Omega)), \quad (3.64)$$

$$= -2E_S E_R (\cos(\Delta\varphi) \cos(\delta \cos(\Omega t)) - \sin(\Delta\varphi) \sin(\delta \cos(\Omega t))). \quad (3.65)$$

Since  $|\cos(\Omega t)|$  is always smaller than one, a Taylor series expansion of Eq. (3.64) can be made for small  $\delta$  up to the quadratic term in  $\varphi_\Omega$ . Thus,

$$I_{det} = -2E_S E_R (\cos(\Delta\varphi) - \cos(\Delta\varphi)(\varphi_\Omega^2/2) - \sin(\Delta\varphi)(\varphi_\Omega)), \quad (3.66)$$

and with

$$(\cos x)^2 = 1/2 (\cos 2x + 1), \quad (3.67)$$

it follows, after filtering the constant terms out, that,

$$I_{det} = \underbrace{2E_S E_R \cos(\Delta\varphi) \delta^2 / 4}_{A_2} \cdot \cos(2\Omega t) + \underbrace{2E_S E_R \sin(\Delta\varphi) \delta}_{A_1} \cdot \cos(\Omega t). \quad (3.68)$$

The amplitude,  $A_1$ , of the first harmonic depends on  $\sin(\Delta\varphi)$ , thus vanishing when  $\Delta\varphi$  is a multiple of  $2\pi$  (formally,  $\Delta\varphi = \pi m$ , but other roots are unstable, thus the mirror moves away from them)

$$\Delta\varphi = \varphi_t - \frac{2\pi\omega}{c} d - \frac{2\pi\omega}{c} \Delta l = 2\pi m, \quad (3.69)$$

with the integer  $m$  representing the order of interference. For the zero<sup>th</sup> order, the phase is given by

$$\varphi_t = \frac{2\pi\omega}{c} (\Delta l + d). \quad (3.70)$$

Therefore, the mirror moves to the closest even position, such that the detected amplitude  $A_1$  is minimised. A calibration of the interferometer is necessary to account for artefacts of the experiment (e.g. cryostat windows). So a measurement without the sample is first conducted to obtain the mirror displacement  $\Delta l_{cal}$ , that would be

zero in the ideal case. Subtracting  $\Delta l_{cal}$  from the displacement with sample  $\Delta l_S$  gives

$$\varphi_t = \frac{2\pi\omega}{c}(\Delta l_S - \Delta l_{cal} + d). \quad (3.71)$$

The amplitude of the second harmonic,  $A_2$ , already includes information about the amplitude  $E_S$ . Again, this property is monitored in the sample measurement ( $A_{2,S}$ ) and in the calibration ( $A_{2,cal}$ ). Now, the transmission coefficient can easily be determined by its absolute value

$$|t| = \frac{E_S}{E_{S,cal}} = \frac{A_{2,S}}{A_{2,cal}}, \quad (3.72)$$

and the phase,  $\varphi_t$  (Eq. (3.71)), by

$$t_{exp} = |t| \cdot e^{i\varphi_t}. \quad (3.73)$$

The sample's geometry is approximated as a plane parallel slab (without magnetic excitations). To calculate the dielectric function,  $\varepsilon$ , out of the investigated transmittance, we use [84]

$$t_{theory} = \left( \cos(kd) - i \frac{\zeta + \zeta^{-1}}{2} \sin(kd) \right)^{-1}, \quad (3.74)$$

with  $k = \sqrt{\varepsilon}\omega/c$  and  $\zeta = 1/\sqrt{\varepsilon}$  including the complex  $\varepsilon$ . Now, comparing  $t_{exp}$  and  $t_{theory}$ , one can obtain numerical values for the dielectric function. Since polarised radiation is used,  $\varepsilon$  is given for a certain polarisation and frequency  $\omega$  emitted by the BWO.

## 3.3 Physical Properties Measurement System

The Physical Properties Measurement System (PPMS) from Quantum Design is a commercial modular system with a large variety of different probes such as a torque magnetometer and an electrometer. Measurements can be performed between 2 K and room temperature, and additionally under magnetic fields up to 14 T. The dielectric function can be obtained down to low frequencies (below 2 MHz) with capacitive methods (e.g. an impedance analyser). The sample is approximated as a plane parallel capacitor, by covering its two opposite surfaces with silver paste. Now, the impedance analyser applies a voltage

$$U(t) = U_0 e^{i\omega t}, \quad (3.75)$$

with amplitude  $U_0$  and frequency  $\omega$ , on the silver paste contacts of the sample and induces a current,

$$I(t) = I e^{i\omega t}, \quad (3.76)$$

between the contacts. Ohm's law states

$$Z = \frac{U_0}{I}. \quad (3.77)$$

Thus, the impedance  $Z$  can be directly measured and the sample's permittivity,  $\varepsilon(\omega)$ , calculated via

$$\varepsilon(\omega) = \frac{d}{\varepsilon_0 A} \frac{1}{i\omega Z}, \quad (3.78)$$

with  $\varepsilon_0$  being the vacuum permittivity. The property  $d$  is the thickness of the sample and  $A$  is the area of the silver paste contacts.

### 3.4 Experimental spectral ranges and units

The previous sections show that the experimental techniques used in this thesis cover a larger range of the electromagnetic spectrum. In total, four orders of magnitude in wavenumbers ( $10^0 \text{ cm}^{-1}$  to  $10^4 \text{ cm}^{-1}$ ) can be detected with the spectroscopic setups and an additional 6 orders with the PPMS setup. An overview of the working ranges is shown in Figure 3.12.

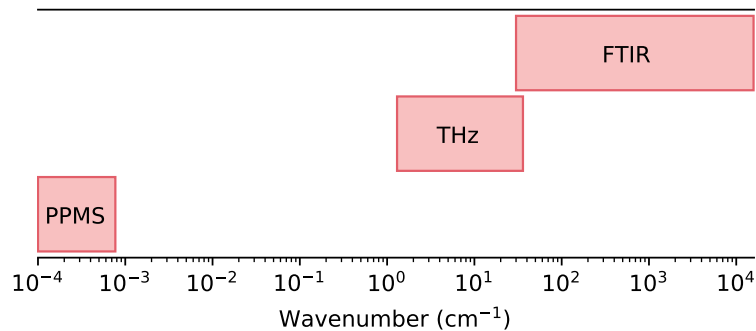


**Figure 3.12:** Overview of the spectroscopic ranges of the used experimental techniques: Fourier transform infrared spectroscopy - FTIR ( $30 \text{ cm}^{-1} - 20000 \text{ cm}^{-1}$ ), Quasi-optical THz-spectroscopy - THz ( $1 \text{ cm}^{-1} - 36 \text{ cm}^{-1}$ ) and Physical Properties Measurement System - PPMS (below  $0.0007 \text{ cm}^{-1}$ ). PPMS covers a much broader regime than shown in this picture, but the values are treated like static properties, as the wavenumbers are small relative to the range of THz and FTIR spectrometers.

Different combinations of these techniques have been used depending on the sample's response in the infrared range. The merger of the data and the different data processing methods are described in the individual results chapters covering the various materials studied.

Dynamic experiments detect the energy of the incoming radiation. Thus the monitored energy of the photons can be expressed in different spectroscopic units. In

general, the energy,  $E$ , and frequency,  $\nu$ , of a photon are connected via

$$E = h\nu, \quad (3.79)$$

with  $h$  being Planck's constant. The frequency,  $\nu$ , represents the number of oscillations of the electric field,  $\mathbf{E}$ , per second. Thus, the basic unit is Hertz ( $1 \text{ Hz} = 1 \text{ s}^{-1}$ ). For example many of the experiments performed in this thesis fall in the terahertz (THz) range ( $1 \text{ THz} = 10^{12} \text{ Hz}$ ).

Most of the numbers in this thesis are given in terms of the wavenumber,  $\bar{\nu}$ , typically used in infrared spectroscopy. This is simply the inverse wavelength

$$\bar{\nu} = \frac{1}{\lambda} = \frac{\nu}{c}, \quad (3.80)$$

with the typical unit being  $\text{cm}^{-1}$ . Frequency is typically shown in GHz (equal to  $10^9 \text{ Hz}$ ). These two units are easily convertible by multiplying the wavenumber in  $\text{cm}^{-1}$  by a factor of  $\sim 30$  to obtain GHz (this factor comes from Eq. (3.80) and is just the approximated value for the speed of light in  $\text{cm GHz}$ ,  $c = 29.9792458 \text{ cm GHz}$ ).



---

# 4

## Low-frequency phonon dynamics in rare-earth langasites

---

This chapter covers the study of low-frequency phonons in langasite  $\text{La}_3\text{Ga}_5\text{SiO}_{14}$  and related rare-earth compounds. The class of materials is introduced, as well as the data acquisition process. The first part of the results section covers the study of an a-cut sample of  $\text{La}_3\text{Ga}_5\text{SiO}_{14}$ , with a focus on the dynamics of an anomalous low-frequency phonon for  $E\parallel c$  polarised light. This anomalous lattice mode is linked to the high static permittivity in this system,  $\varepsilon(0) \sim 100$ . These results are then compared with rare-earth substituted langasites. A softening of this mode can be observed by increasing the mass of the rare-earth ion or by lowering the temperature. This leads to the suggestion that langasites are close to a structural instability. The last section gives an overview of c-cut samples of the same materials.

Large parts of the results, as presented in this chapter, were published in an article in **Physical Review B** [85]. A further contribution was made to reference [86].

### Contents

---

<b>4.1</b>	<b>Introduction</b>	<b>48</b>
<b>4.2</b>	<b>Data processing</b>	<b>50</b>
<b>4.3</b>	<b>The prototype langasite - <math>\text{La}_3\text{Ga}_5\text{SiO}_{14}</math></b>	<b>53</b>
4.3.1	$E\parallel c$	53
4.3.2	$E\parallel b^*$	58
<b>4.4</b>	<b>Rare-earth substituted langasites</b>	<b>59</b>
4.4.1	$E\parallel c$	59
4.4.2	$E\parallel b^*$	64
<b>4.5</b>	<b>Isotropy of langasite c-cut samples</b>	<b>65</b>
<b>4.6</b>	<b>Summary</b>	<b>66</b>

---

## 4.1 Introduction

The family of langasites (with general formula  $A_3BC_3D_2O_{14}$ ) has been studied intensively since the 1980s [87]. A huge variety of isostructural compounds can be grown by exchanging the cations on the  $A$ -,  $B$ -,  $C$ - and  $D$ -sites in the formula above [87–92].  $\text{La}_3\text{Ga}_5\text{SiO}_{14}$  (LGS) is considered to be the parent compound,<sup>10</sup> even though the isostructural  $\text{Ca}_3\text{Ga}_2\text{Ge}_4\text{O}_{14}$  was discovered earlier [87]. In the early years after its discovery, the piezoelectric behaviour of langasites attracted considerable research interest, being studied intensively over the last 40 years [93–99]. Nowadays, possible applications of these materials have been demonstrated in, for example, high temperature acoustic wave devices [100–103] and high temperature nanobalances [104, 105].

The langasites belong to the  $P321$  space group [87], connected to a Bravais lattice with a primitive ( $P$ ) unit cell. Crystals of this space group are characterised by a  $c$ -axis with a threefold symmetry<sup>11</sup> and two two-fold symmetry axes, perpendicular to the  $c$ -axis. The  $P321$  space group is non-polar<sup>12</sup> and non-centrosymmetric.<sup>13</sup> Figure 4.1 shows the structure of a langasite crystal consisting of two alternating layers, ordered perpendicular to the  $c$ -axis. One layer is made out of  $\text{La}^{3+}$  decahedra ( $A$ -sites) and  $\text{Ga}^{3+}$  octahedra ( $B$ -sites), the other layer consists of  $\text{Ga}^{3+}$  ( $C$ -sites) and  $\text{Si}^{4+}/\text{Ga}^{3+}$  tetrahedra ( $D$ -sites), oxygen is finally positioned at the corners of the polyhedra [87, 107].

The application of an external mechanical force along the  $a$  crystallographic direction leads to a distortion of the lattice involving the displacement of  $A$ -site ions away from the center of their polyhedra, such that an electric dipole is created [110], and the crystal becomes piezoelectric. The piezoelectric effect increases for larger ionic radii of the  $A$ -site cations, because the  $A$ -site polyhedra expand as well (in the  $a$ -direction), thus less force is necessary for a distortion of the lattice [96].

Iron langasites ( $A_3B\text{Fe}_3D_2O_{14}$ ) have attracted the interest of the research community mainly due to their magnetoelectric and multiferroic properties [111–115]. In examples such as  $\text{Ba}_3\text{NbFe}_3\text{Si}_2\text{O}_{14}$ , the spin 5/2 iron ions feature a magnetic moment [111]. The  $\text{Fe}^{3+}$  ions form an array of isolated triangles in the  $ab$ -plane situated in the layer composed of the  $C$ - and  $D$ -sites and interact antiferromagnetically [111]. This geometry leads to frustration (as already shown in Figure 1.1), although further interactions with the Fe ions of other triangles yield a more complicated system [10, 111].

These intertriangular interactions include those between the Fe ions imbedded on separate triangles both within the  $ab$  plane and along the  $c$  axis (interlayer) [10]. Interestingly, the strongest of these intertriangular interactions occurs between Fe ions along the  $c$ -axis but not directly parallel to it [10]. The chirality of the crystal defines the stronger interaction [111]. All together, the sum of these interactions

<sup>10</sup> $\text{La}_3\text{Ga}_5\text{SiO}_{14}$  is also responsible for the name langasite, as it is **LAN**thanum **G**Allium **S**ilica**TE**.

<sup>11</sup> $n$ -fold symmetry axis: rotation by  $360^\circ/n$  is the identity.

<sup>12</sup>A crystal is called polar if there exists a set of points (line, plane) such that each of these points remains unmoved by any symmetry operation and can be used as an origin [106].

<sup>13</sup>No point  $X$  exists such that for every atom at position  $\mathbf{r}$  with respect to  $X$ , an atom of the same type is placed at  $-\mathbf{r}$ .

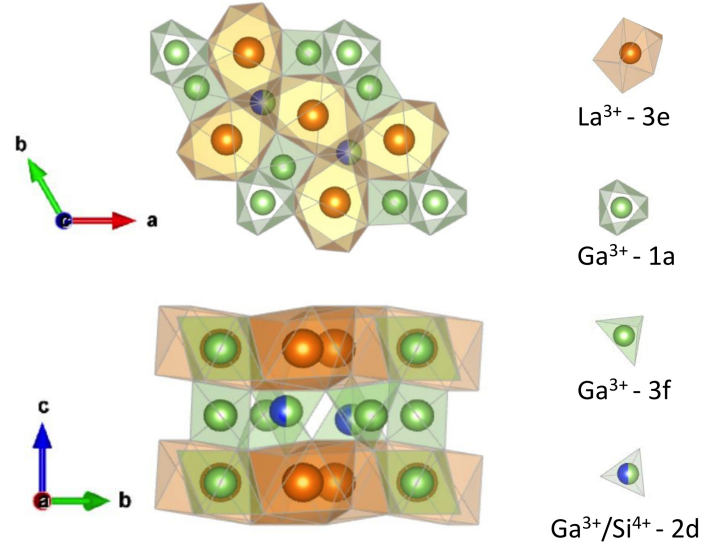


**Figure 4.1:** The langasite structure. In the upper plot, the orange  $\text{La}^{3+}$  ions form the kagome network. The lower plot shows the layered structure of langasites. A legend to the right shows the polyhedra of the individual ion sites along their Wyckoff positions. Oxygen ions are located at the corner sites of the polyhedra, but excluded in this figure. The graphic was generated using the Vesta software package [108] and crystalline information from [109]. Figure adapted from Reference [85].

forces the spins to arrange themselves in  $120^\circ$  steps within the triangle (the direction of the  $120^\circ$  rotation states the chirality within the triangle), with a helical modulation between layers along the c-axis through the crystal [10].

Recently, in our research group, we have investigated the magnetoelectric effect of a diluted rare-earth langasite [86]. In rare-earth langasites of the type  $R_3\text{Ga}_5\text{SiO}_{14}$ , the effects of magnetic frustration result from the arrangement of magnetic rare-earth cations  $R$  (situated on the  $A$ -sites) in a distorted kagome-like network in the ab-plane [19], see Figure 4.1. In these systems, magnetic ordering is not observed even at very low temperatures, despite strong magnetic interactions [19]. Inelastic neutron scattering experiments performed on  $\text{Nd}_3\text{Ga}_5\text{SiO}_{14}$  indeed show signatures of spin-liquid behaviour, such as the lack of long-range ordering down to temperatures in the mK regime [116] and a cooperative paramagnetic behaviour [117, 118]. In other studies, crystal electric field effects of the rare-earth ions are taken account, such that single ion quantum processes are proposed as the origin of the novel magnetic behaviour of this system [119].

Besides the prototype compound LGS, three more langasites were studied in the course of my thesis. These crystals differ by the replacement of the  $\text{La}^{3+}$  ions with other rare-earth elements. A full replacement of La with Nd and Pr is possible, leading to  $\text{Nd}_3\text{Ga}_5\text{SiO}_{14}$  (NGS) and  $\text{Pr}_3\text{Ga}_5\text{SiO}_{14}$  (PGS) crystals. In the case of Ho, a complete substitution is not possible, most probably due to the large difference

in their ionic radii (La 103 pm and Ho 90 pm [120]). Thus, only diluted samples of the type  $(\text{Ho}_x\text{La}_{1-x})_3\text{Ga}_5\text{SiO}_{14}$  can be grown, with  $x = 0.015 \pm 0.002$ . A picture of the four a-cut crystals is shown in Figure 4.2. Here, one can nicely see the different colors of the four samples. The langasite samples studied were typically rectangular plates with edges of  $\sim 7$  mm and a thickness of  $\sim 1$  mm. While LGS crystals are commercially available, the other samples were grown using the Czochralski method by collaborators from the Moscow State University (HoLGS and NGS) and from the Moscow Power Engineering Institute (PGS). Crystals of the c-cut type were studied for LGS, HoLGS and NGS.

The cut of a crystal gains information about the axes lying in the surface plane. For a-cut langasite samples these are the  $b^*$  and  $c$  crystallographic directions. Figure 4.1 shows that the  $b$  axis is not perpendicular to the  $a$  axis. Thus, the  $b^*$  direction is the projection of the  $b$  axis to the plane perpendicular to the  $a$  axis. The c-cut crystals cover the  $a$  and  $b$  (as well as  $a^*$  and  $b^*$ ) axes and are isotropic. Thus, my studies focus on the a-cut samples, that cover all possible information about the lattice. An additional check of the isotropy of the c-cut crystals is performed.

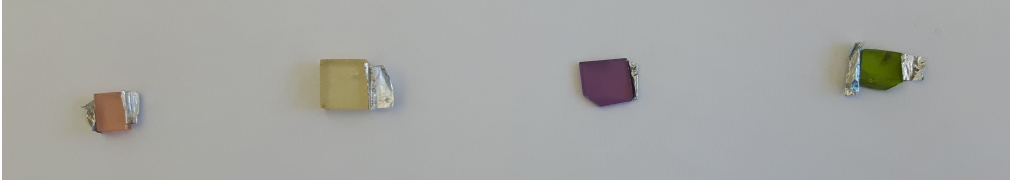


**Figure 4.2:** Photo of the four langasite a-cut crystals. Silver tape used for mounting is attached to the edges of the samples. From left to right: LGS, HoLGS, NGS, PGS.

## 4.2 Data processing

The LGS a-cut sample was first measured in the FTIR spectrometer under room temperature conditions, without the cryostat, for both polarisations ( $E \parallel b^*$  and  $E \parallel c$ ). Here the different settings of the spectrometer (Section 3.1.2) were used to obtain data between  $\sim 25 \text{ cm}^{-1}$  and  $14000 \text{ cm}^{-1}$ . The reflectance, obtained in the THz and MIR settings, was rescaled before merging, such that a smooth overlap between the data of neighbored settings can be achieved. The steps in the reflectance of the neighbored spectral ranges are due to misalignment. Now, by rescaling individual reflectance spectra we can reduce the uncertainties of the global measurement.

It is necessary to fit the data and extrapolate for the frequencies below the detection limit of the FTIR spectrometer. This is because data is needed from  $0 \text{ cm}^{-1}$  to high frequencies to perform the Kramers-Kronig analysis. There are two options available for this procedure. If the first excitation is at a wavenumber in the order of  $\sim 100 \text{ cm}^{-1}$ , such that data is available down to a regime with constant reflectance, the missing part can be approximated as constant in agreement with the lowest known

value. Alternatively, a more precise way is to approximate the low frequency trend with a Lorentzian oscillator, fit to the lowest frequency phonon (see Section 2.2). The software package RefFIT [121–123] is a nice tool for this kind of fits. One capability is to fit the reflectance data with Lorentzian oscillators, such that the dielectric function  $\varepsilon(\bar{\nu})$  is expressed as a sum of Lorentzians:

$$\varepsilon(\bar{\nu}) = \varepsilon_\infty + \sum_i \frac{\Delta\varepsilon_i \bar{\nu}_i^2}{\bar{\nu}_i^2 - \bar{\nu}^2 - i\bar{\nu}\gamma_i}, \quad (4.1)$$

with  $\varepsilon_\infty$  being the high-frequency dielectric permittivity. The properties  $\bar{\nu}_i$ ,  $\Delta\varepsilon_i$  and  $\gamma_i$  are the resonance frequency (in wavenumbers), the dielectric contribution, and the damping of the  $i^{\text{th}}$  Lorentzian oscillator, respectively.

The provided model can be either expressed in terms of reflectance or, for example, the dielectric function. It is crucial to incorporate as much of the data as possible, to get a good low-frequency fit. Small excitations can be ignored in the first approximation, since the focus is on the lowest frequency band. In the case where there are phonons with frequencies close to the lower limit of the raw data (here internal reflections of the beam splitter lead to fringes), one must be careful that the raw data and the RefFIT model overlap well at the merging frequency. Otherwise discontinuities can arise in the data and the proceeding data analysis can produce artefacts.

Fitting procedure for E||c polarisation:

Unfortunately, the lower cut-off frequency of the raw data is close to the lowest frequency phonon in the E||c polarisation. Here, the slope in reflectance can lead to very unstable fits, with inclusion or exclusion of a single data point leading to a big difference in the resulting fit. Thus, a series of three fits is necessary to provide accurate repeatable results.

1. The first step focuses on fitting well above  $100 \text{ cm}^{-1}$ .
2. The second step takes the static permittivity,  $\varepsilon(0)$ , into account giving the correct values for  $R(0)$  in the model. This value,  $\varepsilon_{PP}$ , was typically obtained by conducting measurements in the PPMS. As the PPMS performs measurements at frequencies ( $\sim 10 \text{ kHz}$ ) far below the detection limit of the FTIR spectrometer, these data points can be approximated as static values. The imaginary part of  $\varepsilon(0)$  is assumed to be negligible in the frequency range of the PPMS measurements. I then calculate the reflectance using the dielectric function via Eq. (2.20), neglecting the imaginary part, yielding

$$R(0) = \left| \frac{1 - \sqrt{\varepsilon_{PP}}}{1 + \sqrt{\varepsilon_{PP}}} \right|^2. \quad (4.2)$$

This calculated  $R(0)$  is now included to the approximation. The RefFIT package is able to fit both, the FTIR reflectance and  $R(0)$ , simultaneously. The software aims to minimise  $\chi^2$ , the sum of squared differences between raw data and fit for every data point. Now, the FTIR reflectance data contains  $\sim 1000$

data points, but  $R(0)$  only a single one. Thus, the fit is not affected. This can be solved by weighting the individual  $\chi^2$  of the two data sets. A ratio of 1:3000 for FTIR: $R(0)$  gives accurate results for very low frequencies and remains the fit unchanged above  $\sim 150 \text{ cm}^{-1}$ .

3. Finally, it is then necessary to remove  $R(0)$  from the fitting routine to give a smoother transition from fit to measured data for the third and final fit. Typically, this final fit is now much more stable and is used below  $\sim 32 \text{ cm}^{-1}$ . At this frequency the fit and the raw data now overlap well.

Fitting procedure for E||b\* polarisation:

The E||b\* case, on the other hand, is easier. Here, the raw data is mostly flat below  $60 \text{ cm}^{-1}$ . Thus, the RefFIT fitting is largely stable, without any further problems. There is no need to include static permittivity results. Here, the standard RefFIT model is used from  $0 \text{ cm}^{-1}$  to  $\sim 50 \text{ cm}^{-1}$ .

Above  $\sim 3000 \text{ cm}^{-1}$  the quality of the spectrum decreases (independent from the polarisation). No phonons were observed in this spectral region. The reflectance is mostly flat. Thus, a constant was used as an approximation above  $3000 \text{ cm}^{-1}$ .

The Kramers-Kronig (KK) analysis was then used to calculate the dielectric function,  $\varepsilon(\bar{\nu})$  (for details see Section 3.1.4). The upper limit ( $\bar{\nu}_{max}$ ) of the phase integral (Eq. (3.52)) was set to  $15000 \text{ cm}^{-1}$  for all langasite spectra, and the dielectric function was calculated between  $0 \text{ cm}^{-1}$  and  $3000 \text{ cm}^{-1}$ . That function was then fitted again using RefFIT and the results were compared with the previous fit to ensure the quality of the KK analysis.

Significant parts of my studies were performed by cooling down the LGS crystal in the cryostat, while scanning the reflectance along both crystallographic axes. In total, the sample's reflectance was studied at eight temperatures between 10 K and 300 K. Due to the limited working range of the cryostat, the data can only be obtained in the THz and FIR settings of the FTIR spectrometer (between  $25 \text{ cm}^{-1}$  and  $650 \text{ cm}^{-1}$ ). For the E||b\* polarisation, the FIR setting was used exclusively. For E||c, both settings were used, with the data merged at overlapping data points around  $\sim 45 \text{ cm}^{-1}$ . Since the cryostat data differs systematically from the spectra without the cryostat, all spectra from one series are rescaled with a temperature-independent factor, such that the two FIR measurements at room temperature (with and without cryostat) overlap. To include the spectral weight of phonons above  $600 \text{ cm}^{-1}$ , the MIR data, obtained without using the cryostat, was added to the cryostat data. This data has large influence only on the high-frequency permittivity,  $\varepsilon_\infty$ , and phonons above  $600 \text{ cm}^{-1}$ . Thus, the errors induced by the lack of low-temperature data do not influence the model of the low-frequency phonons. The dynamics of the phonons covered exclusively with the MIR setting are not studied. The low- and high-frequency approximations were performed in the same way as described above.

The rare-earth substituted a-cut langasites were also studied in general in the same way, under identical experimental conditions. Thus, the data analysis process is valid for these samples as well.



The c-cut crystals were given less focus, because an isotropic reflectance is expected (identical to  $E||b^*$  of the a-cut sample). Scans were performed in the cryostat using the THz and FIR settings at 10 K and 300 K only. However, no Kramers-Kronig analysis was done for this group of samples, thus the fitting procedure was skipped as well. The raw reflectance measurements of these samples are covered separately in Section 4.5.

## 4.3 The prototype langasite - $\text{La}_3\text{Ga}_5\text{SiO}_{14}$

### 4.3.1 $E||c$

The characteristic reflectance spectrum of LGS (with  $E||c$  polarisation in the FIR regime of the FTIR spectrometer) is shown for three temperatures in Figure 4.3. At room temperature a strong phonon is observable at  $\sim 40 \text{ cm}^{-1}$ . This low frequency phonon is observed to split into two phonons with decreasing temperature. Here, the arrows labelled as P1 and P2 indicate this low-frequency phonon structure. The inset highlights details of the temperature evolution of these two phonons. The full broadband spectrum, covering the complete measured reflectance, is shown later in Figure 4.9. In total, 17 phonons are observed using the FTIR spectrometer (counting two for the low-frequency structure). A list, summarising all fitted frequencies is given in the Appendix (Table A.1).

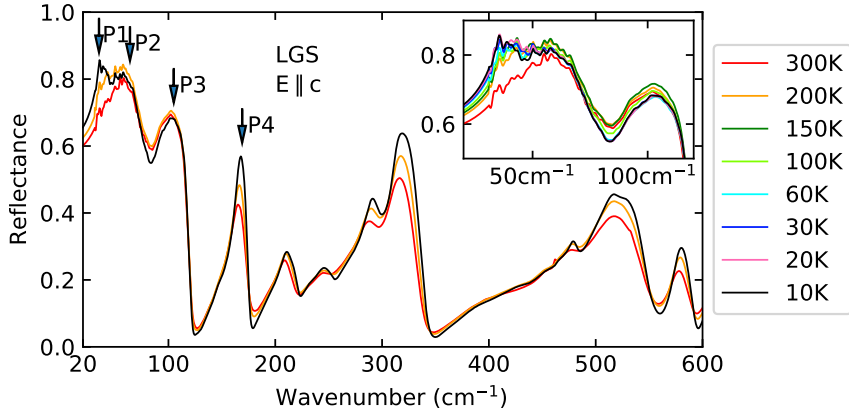


**Figure 4.3:** Reflectance of pure langasite (LGS) for  $E||c$  between  $20 \text{ cm}^{-1}$  and  $600 \text{ cm}^{-1}$ . The four arrows indicate the positions of four lowest frequency phonons. The inset shows a zoomed in section of the reflectance for the spectral region covering the low-frequency phonon and a range of temperatures. Figure adapted from Reference [85].

Two Lorentzians are necessary to provide a good fit of the low-frequency structure at 10 K. When increasing the temperature, the frequency of P1 moves towards P2. From the 200 K measurement on, it is not clear if the fit with one or two oscillators gives better agreement. However, all of the cryostat data was fitted using two

phonons. A comparison of fits using one and two oscillators is plotted in Figure 4.4. This figure highlights the agreement between the two-phonon fits and the raw data at  $\sim 30 \text{ cm}^{-1}$ . The data for static permittivity, included to the fit, was extracted from Mill *et al.* [87].

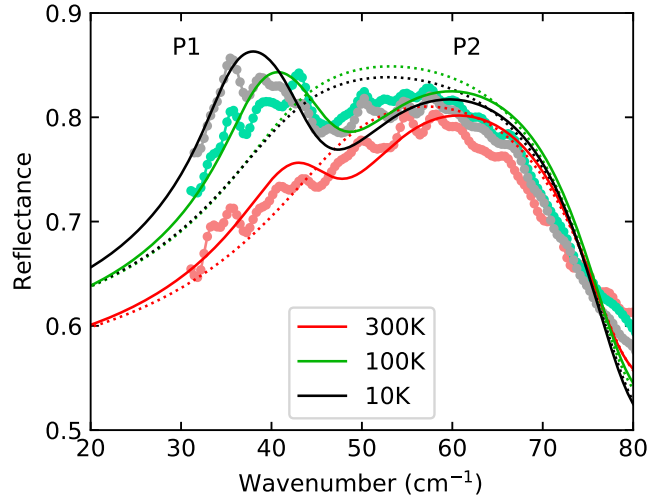


**Figure 4.4:** Comparison of raw reflectance with fits of LGS ( $E||c$ ). The data points in faded colors represent the raw data from the FTIR measurement from  $\sim 30 \text{ cm}^{-1}$  on. Full lines are fits with two Lorentzian oscillators, as used for the further data treatment. In comparison, dotted lines are fits with a single phonon. The one-phonon fit seems to be the better choice only for the highest temperature, 300 K. Figure adapted from Reference [85].

After performing the Kramers-Kronig analysis, the dielectric function was obtained and is plotted in Figure 4.5. Here, it is clear that the spectra are dominated by the influence of the low-frequency phonons. Spectra of the real part,  $\epsilon_1$ , show that the main contribution to the large static permittivity,  $\epsilon(0) \sim 100$ , is a result of P1 and P2. Other phonons seem to have only a minor influence. According to Mill *et al.* [87],  $\epsilon(0)$  increases for lowering temperature. Here, the same behaviour could be observed. In  $\epsilon_2$ , the large peak due to the low-frequency phonon dominates the complete spectrum. The maximum value is  $\sim 270$  and thus is 10 times larger than that of P3 and P4. At lower temperatures, a sharpening of the phonons can be observed.

At 10 K, the maximum of P3 and P4 in  $\epsilon_2$  is  $\sim 25$  and decreases for larger temperatures. The resonance frequency of these excitations stays almost constant. Figure 4.6 showcases the fits of the P1 and P2 phonons in terms of  $\epsilon_2$ . Here, both phonons move toward higher frequencies for increasing temperature. P1 shifts more rapidly, thus, it seems that the two phonons merge.

An overview of the fitting parameters of the first four Lorentzian profiles as a function of temperature is presented in Figure 4.7. Here, one can see the resonance frequency,  $\bar{\nu}_0$ , of the oscillators as well as their dielectric contribution,  $\Delta\epsilon$  (with  $\Delta\epsilon = \bar{\nu}_P^2/\bar{\nu}_0^2$ ). The primary contribution to the static permittivity comes from the



P1 and P2 phonons. All other contributions are in the range between  $\Delta\varepsilon = 0$  and  $\Delta\varepsilon = 2$ . While the difference in spectral weight ( $SW = \Delta\varepsilon \cdot \bar{v}_0^2$ ) of both phonons, P1 and P2, decreases (and finally changes sign at 300 K), the sum of them ( $SW_{P1} + SW_{P2}$ ) remains constant (see inset of Figure 4.7).

Figure 4.7(b) shows, in more detail, the unique behaviour of the P1 mode. This phonon softens (its frequency moves towards zero), while the frequencies of all other modes remain almost constant. A soft mode often indicates a structural transition, as described in Section 2.3.1. Here, I introduce Cochran's law (Eq. (2.48)) connecting the squared frequency of the soft mode with the critical temperature of a transition. In the case of the LGS P1 phonon, this temperature was fitted to  $T_C \sim -740$  K. Here, the temperature is fitted to be negative. (The temperature dependency of the squared frequency is presented in comparison with the other samples in Figure 4.11.) Thus, a phase transition cannot be reached. The application of an electric field that overcomes 740 times  $k_B$ , the Boltzmann constant, would close this energy gap and a transition is possible. A simple model<sup>14</sup>, assuming a cosine-like potential, expects electric fields in the order of  $10^9$  V/m. The anomalous low frequency structure is seen for E||c polarisation. The displacement of the mass due to the oscillations leads to a loss of the two-fold axes, perpendicular to the c-axis of the  $P321$  space group. Thus, the transition yields a  $P3$  space group, that is a polar phase.

The full study of the static dielectric permittivity ( $\varepsilon(0)$ ) of LGS is presented in Section 4.4.1 in comparison with all langasites studied in the frame of my thesis.

<sup>14</sup>We assume a cosine-like potential,  $W$ ,

$$W = -W_0 \cos(2\pi x/a),$$

with,  $a \approx 0.5$  nm, being the lattice constant and  $x \approx 0$ , being the position of the  $\text{La}^{3+}$  ion. Now, the force,  $F$ , is defined as

$$F = -\frac{\partial W}{\partial x} = -W_0 \frac{2\pi}{a} \sin(2\pi x/a) \approx -W_0 \left(\frac{2\pi}{a}\right)^2 x.$$

The equation of motion is

$$-W_0 \left(\frac{2\pi}{a}\right)^2 x = m\ddot{x}.$$

The substitution,

$$x = \cos(\omega t),$$

yields

$$\omega^2 = \frac{W_0}{m} \left(\frac{2\pi}{a}\right)^2.$$

Thus, with  $\omega = 40 \text{ cm}^{-1}$ ,  $m$ , the mass and  $Q$ , the charge of the  $\text{La}^{3+}$  ion, we get

$$W_0 = \frac{\omega^2 m a^2}{(2\pi)^2} \sim 0.5 \text{ eV}.$$

$$F_{max} = W_0 \frac{2\pi}{a} = \omega m \frac{a}{2\pi} = EQ.$$

$$E = W_0 \frac{2\pi}{a} \frac{1}{Q} = \frac{\omega^2 m a}{2\pi Q} \sim 10^9 \text{ V/m}.$$

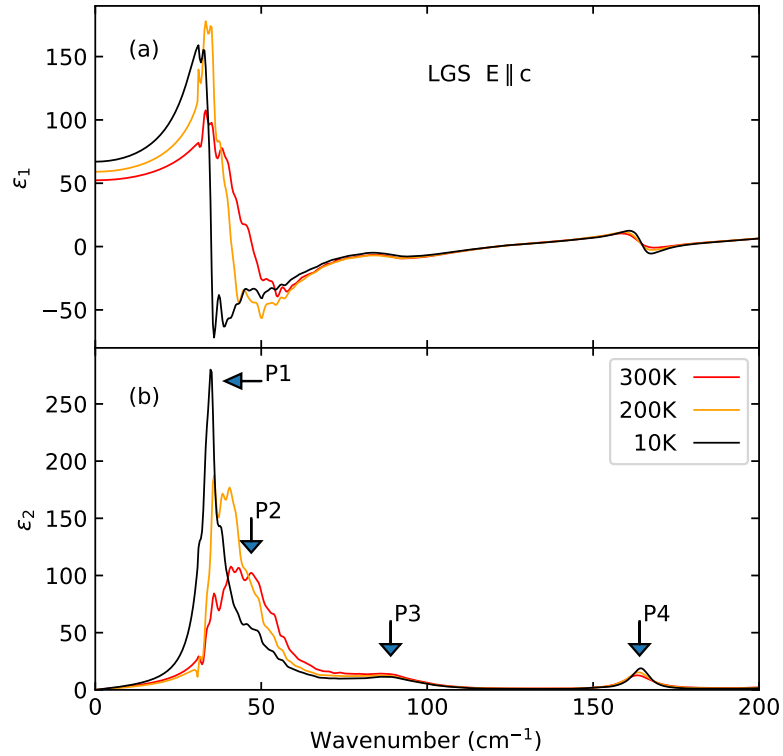


**Figure 4.5:** Dielectric function of pure langasite (LGS)  $E||c$ , split into the real part,  $\epsilon_1$  (a), and the imaginary part,  $\epsilon_2$  (b). In (b), the four arrows indicate the fitted positions of the four phonons with the lowest four resonance frequencies. Here, the spectra are dominated by the low-frequency structure of the P1 and P2 modes. One can see the strong shift of P1 towards higher frequencies, while P3 and P4 stay constant. Figure adapted from Reference [85].

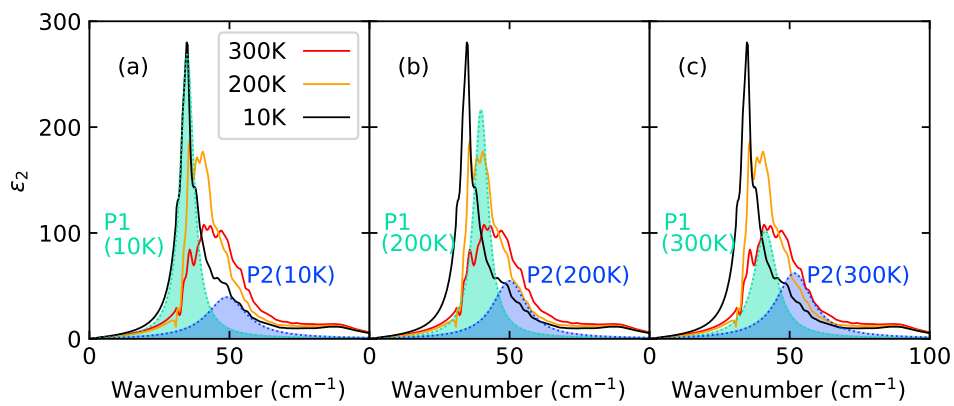


**Figure 4.6:** Fits of P1 and P2 plotted along with the  $\epsilon_2$  spectra at (a) 10 K, (b) 200 K and (c) 300 K. Figure adapted from Reference [85].

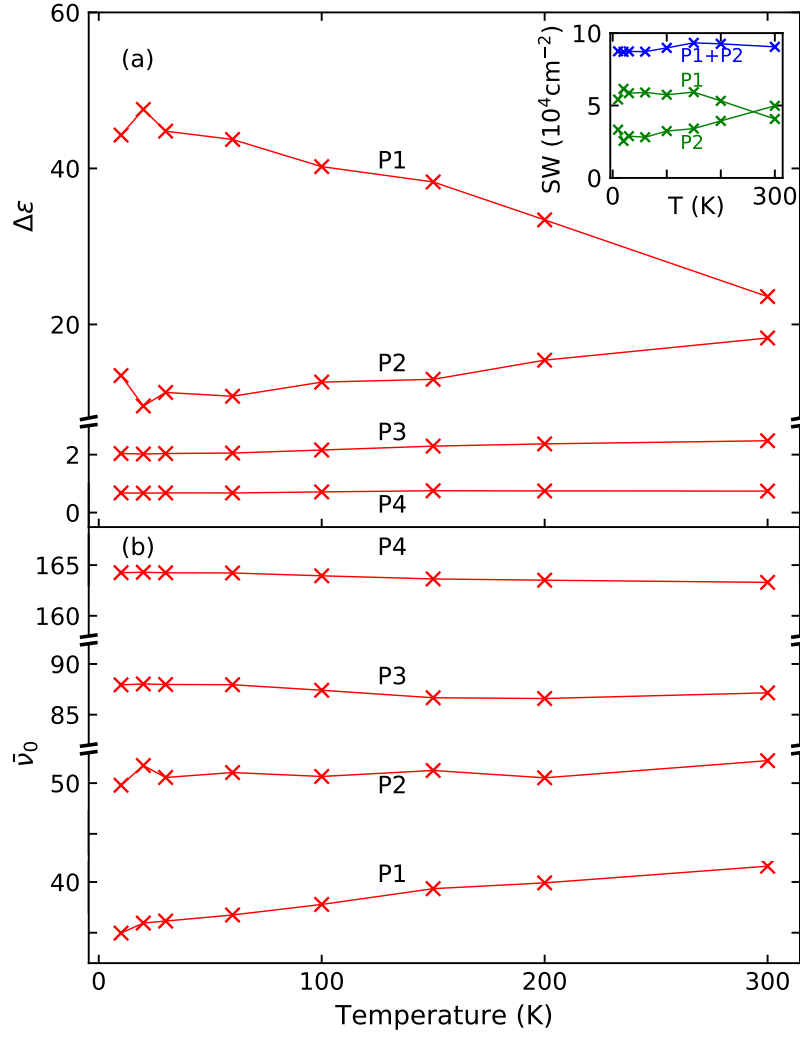


**Figure 4.7:** Fitting parameters including the dielectric contribution,  $\Delta\varepsilon$  (a), and resonance frequency,  $\bar{\nu}_0$  (b), of LGS for E||c polarisation. The inset in (a) shows the spectral weight,  $SW = \Delta\varepsilon \cdot \bar{\nu}_0^2$ , of the P1 and P2 phonons. Figure adapted from Reference [85].

### 4.3.2 $\text{E} \parallel \text{b}^*$

A higher number of phonons can be seen in the FIR regime for  $\text{E} \parallel \text{b}^*$  polarised light, as shown in Figure 4.8. In this range a total of 22 optical phonons could be detected. Here, the reflectance spectra of LGS are plotted for three different temperatures (10 K, 200 K and 300 K) between  $50 \text{ cm}^{-1}$  and  $550 \text{ cm}^{-1}$ . All data was obtained using the cryostat. A full broadband reflectance spectrum is shown later, in comparison with the substituted langasites, in Figure 4.14(a).

For polarisation  $\text{E} \parallel \text{b}^*$ , the complete phonon structure stays almost constant in the investigated temperature regime between 10 K and room temperature (see Figure 4.8(a)). Only a weak phonon at  $\sim 310 \text{ cm}^{-1}$  is observed to vanish at higher temperatures. Small shifts of the resonance frequency are also observed when changing temperature, similar to the  $\text{E} \parallel \text{c}$  phonons at frequencies above  $100 \text{ cm}^{-1}$  (Figure 4.8(c)). Typically, a broadening occurs at higher temperatures. The static permittivity (see Figure 4.8(b)) remains rather constant, nevertheless a subtle trend towards decreasing values can be seen when cooling down the sample. This behaviour of  $\epsilon(0)$  is in agreement with measurements of this property presented in reference [87].

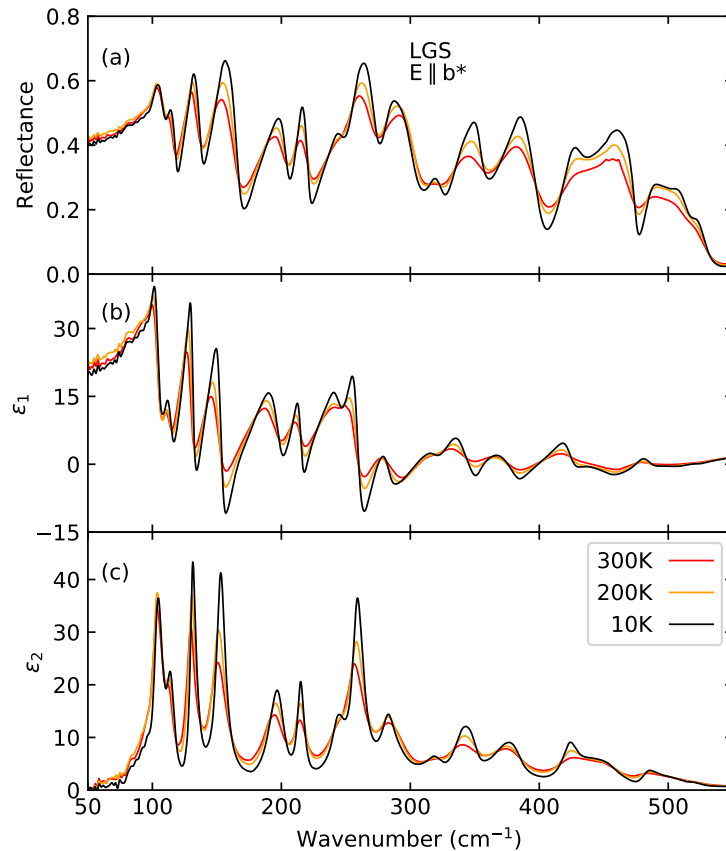


**Figure 4.8:** Reflectance (a) and dielectric function (b,c) of LGS for  $\text{E} \parallel \text{b}^*$  at different temperatures in the FIR range. Figure adapted from Reference [85].

In this direction, no low-frequency softening phonons can be seen. The lowest phonon is situated around  $90 \text{ cm}^{-1}$ .

In total, the reflectance study reveals 39 fitted phonons (17 for  $E||c$  and 22 for  $E||b^*$ ). The number of optical active phonons can be theoretically achieved out of the crystalline structure. Here the Bilbao Crystallographic Server [124, 125] was used to calculate a total of 37 optical active modes for  $\text{La}_3\text{Ga}_5\text{SiO}_{14}$ . The full representation reads as follows:

$$\Gamma = 11A_1^{(R)} + A_2^{(A)} + 13A_2^{(IR)} + E^{(A)} + 24E^{(IR+R)}.$$

Here, the superscripts represent acoustic (A), Raman (R) and infrared (IR) active modes. Information about the LGS crystallographic structure was taken from [109]. A detailed look at all listed resonance frequencies (Appendix A.1.1) shows that a phonon is visible at  $\sim 733 \text{ cm}^{-1}$  for both polarisations. This mode seems to be degenerate, appearing along both investigated crystallographic directions. The low-frequency structure for  $E||c$  is counted as two phonons (P1 and P2). The P1 mode approaches P2 with increasing temperature. Thus, it is possible that one mode splits into P1 and P2. The half Si / half Ga occupation of one site could cause a local distortion of the A-sites in the crystal, leading to an additional mode.

## 4.4 Rare-earth substituted langasites

Three additional langasite a-cut samples of  $\text{Nd}_3\text{Ga}_5\text{SiO}_{14}$  (NGS),  $\text{Pr}_3\text{Ga}_5\text{SiO}_{14}$  (PGS) and  $(\text{Ho}_x\text{La}_{1-x})_3\text{Ga}_5\text{SiO}_{14}$  (HoLGS) are studied in the same way as LGS, in order to investigate the influence of substituting the La ions with different rare-earth elements. The aim is to check whether the anomalous low frequency structure of the  $E||c$  polarisation can be observed in all substituted langasites and how the mode depends on the rare-earth ion. The results are summarised in this section.

### 4.4.1 $E||c$

The main goal of the measurements with  $E||c$  polarisation was to investigate the influence of rare-earth substitution on the low-frequency phonon. Figure 4.9 shows the room temperature reflectance of all four langasites as a comparison. Here, one can see, the anomalous low-frequency phonon structure exists in all investigated samples. Thus, this low frequency phonon seems to be a general feature of the langasite family.

The langasite structure seems to be generally stable, with the rare-earth substitution leading only to minor differences in the reflectance between different samples. The shape of the four curves is almost identical. Full spectra of the substituted langasites are presented in Appendix A.1.2.

However, a closer look into the reflectance data reveals that the low-frequency structure is shifted for the different samples. Plots of the dielectric function give a clear proof that the maximum in  $\varepsilon_2$  of the anomalous mode (and so the resonance frequency of that structure) depends on the material. The dielectric function is

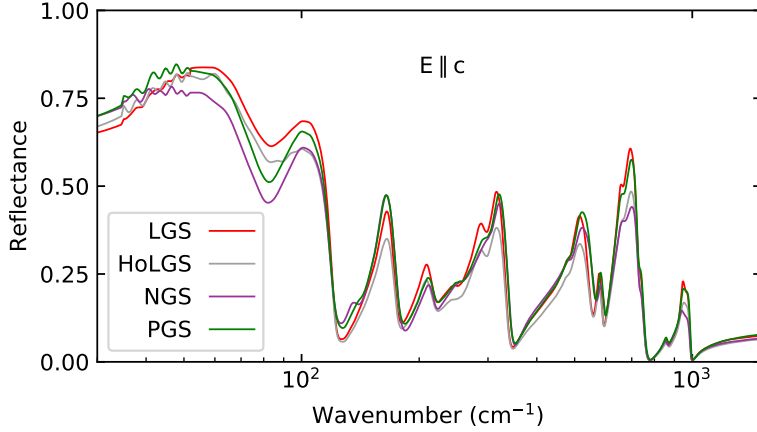


**Figure 4.9:** Room temperature reflectance of all four langasite samples for  $E||c$  polarisation. The spectra are conducted without the cryostat and are plotted between  $30\text{ cm}^{-1}$  and  $1500\text{ cm}^{-1}$ . Figure adapted from Reference [85].

plotted in Figure 4.10(a,b). All data shown here was obtained under atmospheric conditions and was measured without the use of the cryostat. Fits were performed using a single Lorentzian oscillator to model the anomalous low-frequency structure in RefFIT. The modelled resonance frequencies are summarised in the Appendix (Table A.1). HoLGS has, just like LGS, 17 optical phonons in the  $E||c$  polarisation. The other langasites, NGS and PGS, show an additional excitation at  $\sim 135\text{ cm}^{-1}$ , as shown in the inset of Figure 4.10(b).

The fitting parameters of the low-frequency phonon were studied in more detail to see the possible effects of the rare-earth substitution. Thus, the resonance frequency ( $\bar{\nu}_0$ ), the dielectric response ( $\Delta\varepsilon$ ) and the spectral weight ( $SW$ ) of the first model oscillator are plotted as a function of the atomic number of the rare-earth element in Figure 4.10(c-e). In the case of HoLGS, an effective atomic number is used, calculated from the ratio of Ho and La in the crystal. The atomic number has no direct physical property in the lattice, so the fitting parameters are also plotted as a function of the atomic mass and the ionic radius. The errorbars represent the uncertainty assuming a 5% variation in reflectance.

The resonance frequency shifts linearly towards lower wavenumbers for increasing atomic number (Figure 4.10(c)). Extrapolating for full Ho-substitution, the trendline approaches a resonance frequency of  $\sim 22\text{ cm}^{-1}$ , roughly half of the value of the LGS mode. This softening for smaller ionic radii could be the explanation for the instability of HoLGS single crystals with higher amounts of Ho. Holmium has an ionic radius of 90 pm, much smaller than all the other substitution rare-earth elements.

The dielectric contribution of the lowest oscillator has the opposite behaviour compared to the resonance frequency (Figure 4.10(d)). It increases for larger atomic numbers. Both effects lead to constant values of the spectral weight of this Lorentzian oscillator (Figure 4.10(e)).

Figure 4.11 shows the squared frequencies of the P1 mode. Linear fits are included

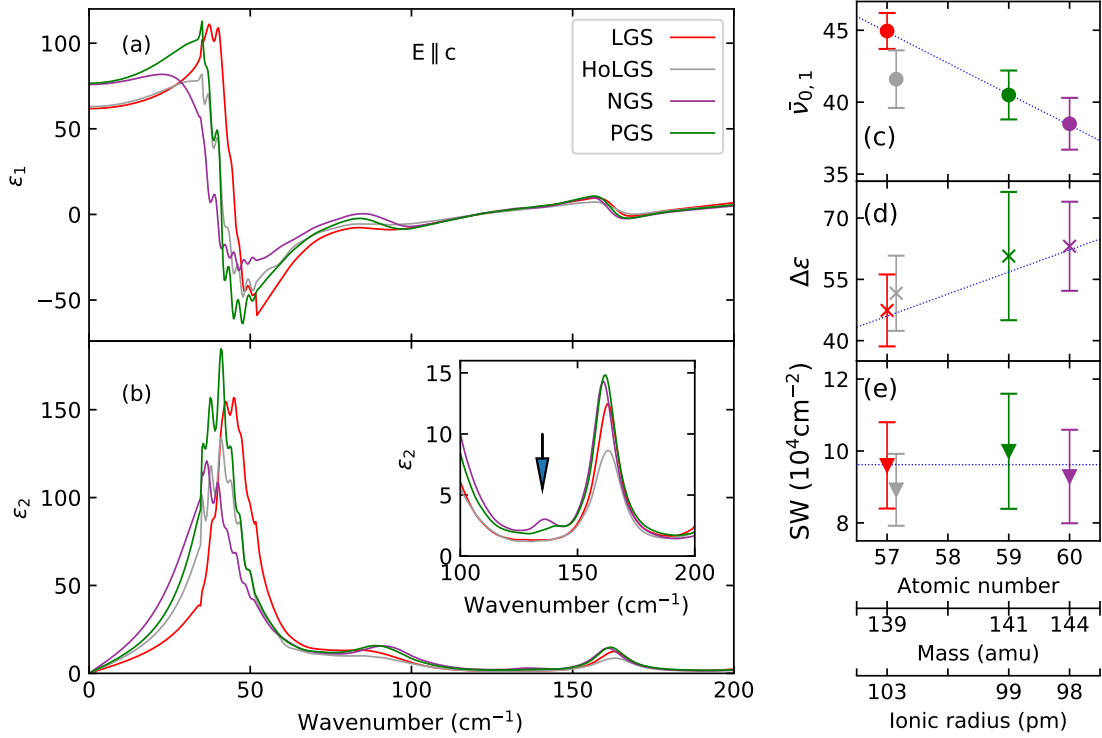


**Figure 4.10:** Dielectric function of all four langasite samples for  $E||c$  (a,b). The inset in (b) highlights the additional weak excitation of NGS and PGS at around  $135\text{ cm}^{-1}$ . Fitting parameters of the anomalous low-frequency phonon structure including resonance frequency (c), dielectric contribution (d) and spectral weight (e). Linear trend lines of these properties are plotted on top. Data obtained at room temperature, the low-frequency structure is fitted using a single oscillator only. Figure adapted from Reference [85].

to highlight the baseline interception point. This would correspond to a complete softening of the mode. Taking this assumption and applying Cochran’s law (Eq. (2.48)) we can approximate the critical temperature,  $T_C$ , of a potential structural instability. This temperature increases for increasing atomic number of the substituting ion. For positive values of  $T_C$ , a structural phase transition to a polar phase (space group  $P3$ , as mentioned above) would be expected at that temperature. A linear fit of the critical temperature as a function of the atomic number of the rare-earth ion gives positive values for atomic numbers of 62 (Sm) and greater.

Some more information can be extracted from the dielectric permittivity curves, as it is clearly visible that  $\epsilon_1(0)$ , and so  $\epsilon(0)$ , are different for each individual sample. Mill *et al.* [87] showed that static permittivity values are different for various members of the langasite family.

Static permittivity can be extracted from reflectance using the ReFFIT model. Fits were performed for all four langasites using two oscillators for modelling the

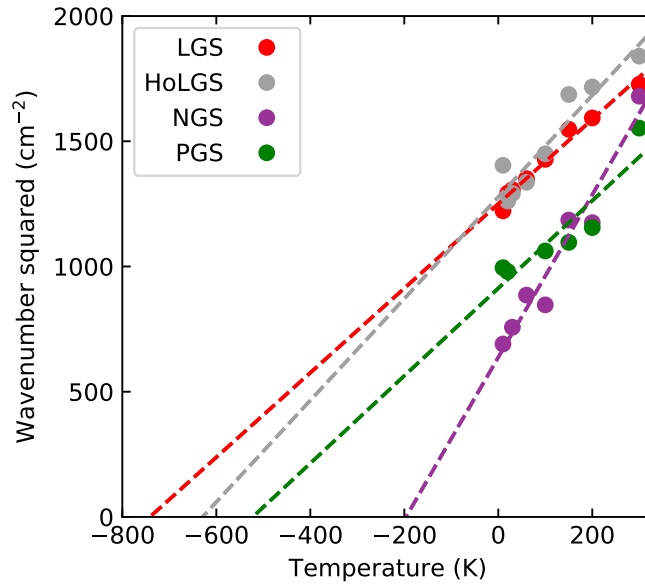


**Figure 4.11:** Squared frequencies of P1 phonon of all four langasites. Linear fits intercept the baseline at different temperatures (the 30 K data point of PGS was excluded). Figure adapted from Reference [85].

low-frequency structure and the results are plotted individually in Figure 4.12. A trend towards lower static permittivity for increasing temperature can be seen for all samples. This figure further shows the good agreement between the measured (fitted) FTIR spectral data and the static measurements performed with the PPMS. The sum of the two phonons of the low-frequency structure is marked. Here one can see that there is a temperature-independent contribution missing to match  $\epsilon(0)$  in each sample. Now, this is the sum of the dielectric contribution of all phonons excluding the P1 and P2 phonons. Figure 4.7(a) shows that the dielectric contribution of the LGS P3 and P4 phonons remains stable in the investigated temperature range. Thus, the dielectric contribution is assumed to be temperature-independent for all phonons except the low-frequency phonon structure. As our LGS sample was not studied in the PPMS,  $\epsilon(0)$  data was taken from [87]. These values are identical to the data of the HoLGS sample (data from [126], see the LGS plot of Figure 4.12). This is not unexpected, because the low Ho amount does not show large influence. The static measurements of NGS and PGS have been performed by A. Kuzmenko at the Moscow General Physics Institute.

The quasi-optical THz setup was used to study the phonon spectra at frequencies below the detection limit of the FTIR spectrometer (from  $8\text{ cm}^{-1}$  to  $15\text{ cm}^{-1}$ ). Here, the HoLGS crystal was exclusively probed in transmission along the  $E||c$  polarisation. The results gain details of the low-frequency shoulder of the P1 and P2 modes. Figure 4.13(a) presents a transmission spectrum conducted at 2 K including a fit with a Lorentzian profile. This fitted frequency is in close agreement with the FTIR data (at 10 K).



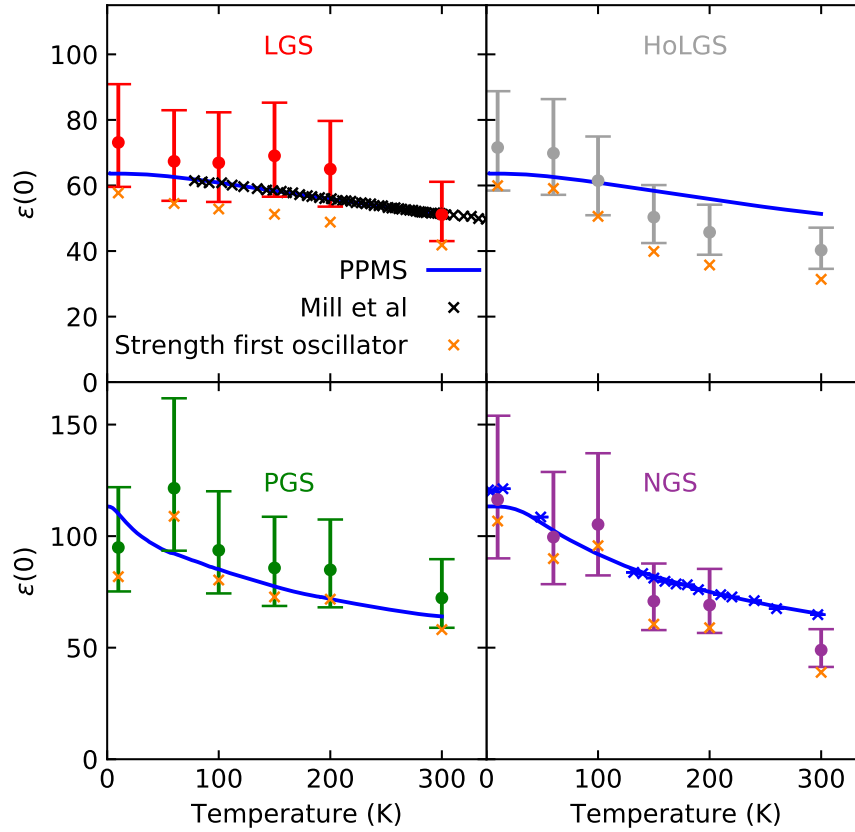


**Figure 4.12:** Comparison of static permittivity of the four langasites for  $E||c$  polarisation. The coloured errorbars represent the static permittivity obtained using RefFIT with 5% uncertainty in reflectance. The orange crosses represent the dielectric contribution,  $\Delta\varepsilon$ , of just the low-frequency anomalous structure. Full blue lines represent the static permittivity measured in the PPMS. In the case of LGS, PPMS data from HoLGS is plotted (taken from [126]) and the LGS data is from Mill *et al.* [87]. Blue crosses on top of the NGS PPMS data show additional measurements with the quasi-optical THz spectrometer at  $3\text{ cm}^{-1}$ . Figure adapted from Reference [85].

Now, in this setup magnetic fields can be applied up to 7 T. The relative change in transmission is presented in Figure 4.13(b). The figure shows that the transmission increases with larger magnetic fields, but ends in saturation above  $\sim 4$  T. This field strength is in the order of the saturation of the magnetic moments in HoLGS, as shown in reference [86]. This behaviour could be a signature of a spin-lattice coupling. For more details on this transmission measurements see references [85, 126].

Crystal electric field (CEF) levels are observed in close proximity to the P1 phonon in NGS [127]. This leads to the suggestion that spin-lattice dynamics have to be included in the discussions about the local environment of the magnetic ions. Interestingly, a CEF level is also expected for HoLGS in proximity to the P1 mode [86].  $\text{Ho}^{3+}$  ions are non-Kramers ions, oppositely to  $\text{Nd}^{3+}$ , such that doublets are not protected. Thus, a vibronic coupling is possible between the phonons and the CEF levels. A more detailed report on the CEF levels in langasites including a deeper discussion is presented in my paper, reference [85].

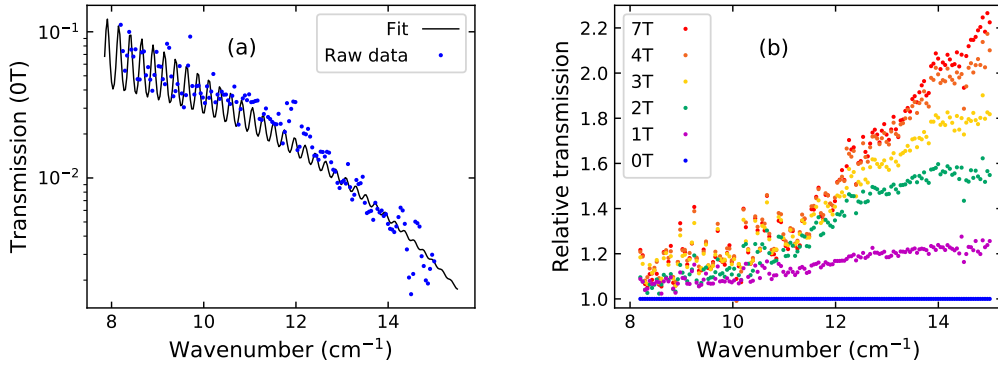


**Figure 4.13:** Measurements of the HoLGS transmission ( $E||c$  polarisation) performed using the THz-spectrometer. (a) Comparison of raw transmission and fit at 2 K, (b) relative change in transmission for different external magnetic fields,  $H||b^*$ . Figure adapted from References [85] and [126].

#### 4.4.2 $E||b^*$

This series of measurements focuses on the differences between the four materials. Similar to the  $c$ -direction, the four samples show an almost identical reflectance curve as plotted in Figure 4.14(a). The phonon frequencies are only slightly shifted. A shift of spectral weight between the phonons can be observed.

The LGS and HoLGS crystal show one additional excitation, that can be seen as a right shoulder of the  $100 \text{ cm}^{-1}$  phonon in Figure 4.14(b) (fitted resonance at  $\sim 113 \text{ cm}^{-1}$ ). This is exactly opposite to the other polarisation, where NGS and PGS show one additional weak phonon. Thus, the sum of all observed phonons remains constant for all four investigated langasites. A more detailed overview of the spectra of the substituted langasites is given in Appendix A.1.2.

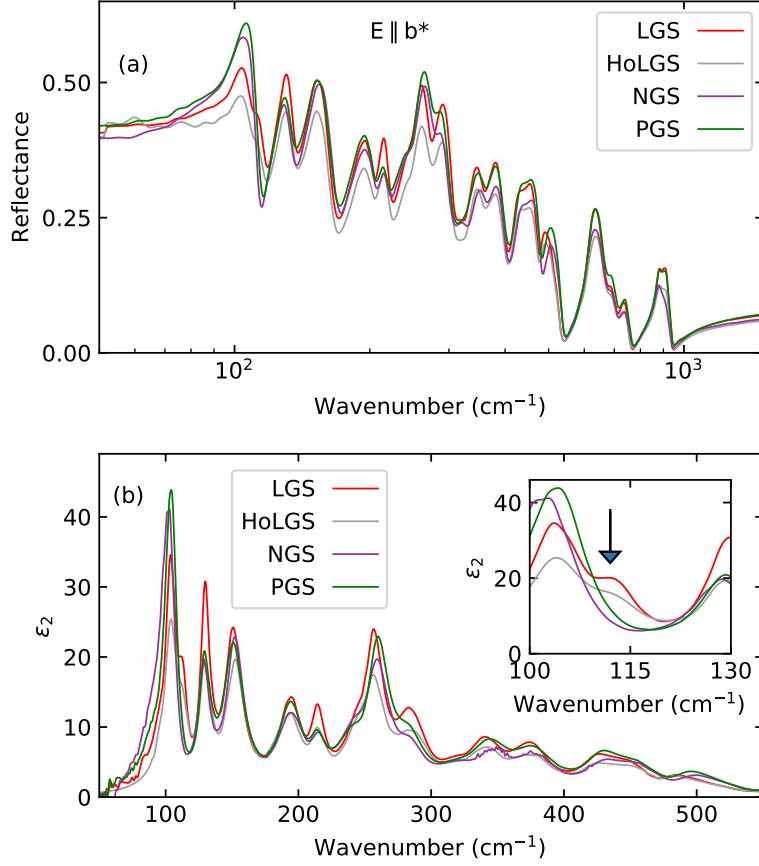


**Figure 4.14:** (a) Broadband reflectance (between 50 cm<sup>-1</sup> and 1500 cm<sup>-1</sup>) and (b), imaginary part of the dielectric function (from 50 cm<sup>-1</sup> to 550 cm<sup>-1</sup>) of the four a-cut langasite samples obtained for E||b\* polarisation. The inset highlights the area around 113 cm<sup>-1</sup>, the arrow indicates the additional peak of the LGS and HoLGS sample in  $\epsilon_2$ . Figure adapted from Reference [85].

## 4.5 Isotropy of langasite c-cut samples

An overview of the studies of langasite c-cut samples will be presented in this section. Here three langasites were studied, LGS, HoLGS and NGS. This type of cut gives information about the a and b crystallographic directions (as well a\* and b\*). These samples should be isotropic, according to their crystalline symmetry. Thus, the reflectance should be identical for any arbitrary angle of polarisation.

A small survey of these crystals was performed to verify that rare-earth substitution does not lead to anisotropy of the two-fold symmetry axes. For this purpose, scans were performed in the FIR and THz settings of the FTIR spectrometer while varying the polarisation angle in steps of 15°. This was done at two temperatures, room temperature and 10 K. It was found that the detected reflectance is independent of the polarisation angle, for each crystal at all temperatures. Figure 4.15 shows this

for the example of the HoLGS c-cut crystal. Here, one can see that the data of the different angles of polarisation overlap very nicely above  $100\text{ cm}^{-1}$ . The spectra become noisier at lower frequencies, thus the different polarisations show small changes in the reflectance. One additional feature can be seen at  $\sim 420\text{ cm}^{-1}$ . This wavenumber region covers two close lying phonons at 300 K that seem to be identifiable as two only at lower temperatures. Only the measurement at  $90^\circ$  shows the clear splitting at all temperatures. This could be due to an anisotropy in the Ho stuffing within the crystal.

As discussed above, the reflectance of this plane should be identical to the  $E\parallel b^*$ -results of the a-cut samples. Thus, in the figure, this measurement is added to those of the c-cut spectra. The shape of the reflectance of both samples is generally similar. Almost perfect overlap is achieved after rescaling the a-cut reflectance by a factor of 1.1. Thus, the isotropy of the samples can be verified as well as the correct sample orientation. Interestingly, the  $\sim 420\text{ cm}^{-1}$  result of the  $90^\circ$  scan is observable in the  $E\parallel b^*$  measurement.

## 4.6 Summary

The phonon spectra of  $\text{La}_3\text{Ga}_5\text{SiO}_{14}$  are studied in detail and compared with three other isostructural materials of the langasite family. The reflectance was detected with an FTIR spectrometer at various temperatures between 10 K and 300 K. Static measurements were performed additionally using the PPMS setup. Spectra for  $E\parallel c$  polarisation are dominated by an anomalously strong phonon at  $\sim 40\text{ cm}^{-1}$ . A weaker excitation is observed close by, such that those phonons merge at higher temperatures ( $\sim 100\text{ K}$ ). Rare-earth substitution of  $\text{La}^{3+}$  ions leads only to minor changes in the phonon spectra. The strongest effect can be seen in the low-energy phonon. Its frequency decreases linearly with increasing atomic number of the substituting ion. Together with the temperature-dependent softening of this mode, this effect gives rise to an emerging lattice instability of the langasite structure. A transition from the  $P321$  space group to a close lying polar  $P3$  phase is suggested for full softening of this low-frequency phonon. Magneto-optical measurements on HoLGS (for  $E\parallel c$ ) show that the applied magnetic field effects the dynamics of the lowest frequency mode. The close lying CEF levels indicate the possibility for novel spin-lattice effects in this compound.

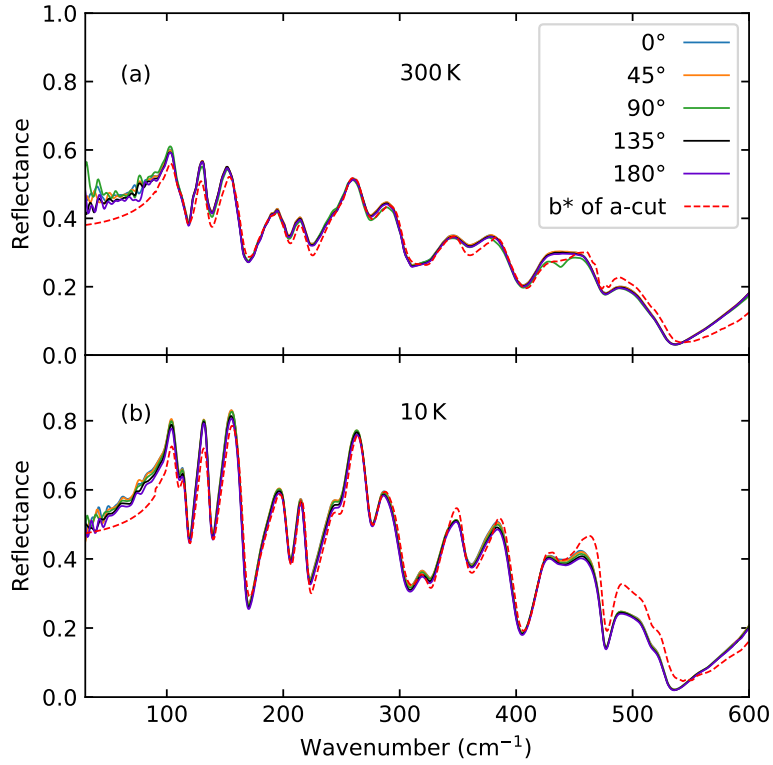


**Figure 4.15:** The reflectance of a HoLGS c-cut crystal is plotted in steps of 45° polarisation rotation. The upper plot, (a), was conducted under room temperature conditions, (b) at a sample temperature of 10 K. A good agreement can be seen for both cases, especially above 100 cm<sup>-1</sup>. Below this wavenumber, the signal to noise ratio is reduced and so the uncertainties increase. Additionally, the E||b\* reflectance of the HoLGS a-cut crystal is plotted for comparison (dashed line) and rescaled by a factor of 1.1. The angles of polarisation are given relative to the vertical position of the polariser.



---

# 5

## Soft-mode lattice dynamics in francisite

---

This chapter covers THz and FIR studies on francisite ( $\text{Cu}_3\text{Bi}(\text{SeO}_3)_2\text{O}_2\text{Cl}$ ). An introduction describes francisite and its prominent properties. A description of the data acquisition and analysis process then follows. Our studies on the soft-mode and lattice dynamics are shown in the results section, along with a discussion. The short summary section closes this chapter.

A draft manuscript based on this chapter is currently under preparation for publication [128]. Furthermore, two student projects ([129, 130]) were supervised, dealing with spectra at room temperature and with preliminary FTIR studies on francisite at low temperatures.

### Contents

---

<b>5.1</b>	<b>Introduction and structural properties of francisite . . .</b>	<b>70</b>
<b>5.2</b>	<b>Data treatment . . . . .</b>	<b>71</b>
<b>5.3</b>	<b>Results . . . . .</b>	<b>72</b>
5.3.1	Reflectance and dielectric function . . . . .	72
5.3.2	Fits . . . . .	74
5.3.3	Antiferroelectricity . . . . .	77
5.3.4	Ferroelectric signature of a soft mode . . . . .	78
5.3.5	Sublattice polarisation . . . . .	80
5.3.6	Spin-lattice effects in $\hat{b}$ -direction . . . . .	82
<b>5.4</b>	<b>Summary . . . . .</b>	<b>83</b>

---

## 5.1 Introduction and structural properties of francisite

Francisite ( $\text{Cu}_3\text{Bi}(\text{SeO}_3)_2\text{O}_2\text{Cl}$  or CBSCl) is a material from the family of selenites, named after Glyn Francis, who first identified this greenish material in the Iron Monarch ore body in southern Australia [131]. Besides this parent compound, halogen substituted isostructural francisites of type  $\text{Cu}_3\text{Bi}(\text{SeO}_3)_2\text{O}_2\text{X}$  with  $\text{X}=\text{Br}, \text{I}$  [132, 133] can be grown artificially. Crystals can also be synthesised by replacing Bi with rare-earth elements such as Er, Sm, Eu and Lu [134–136]. The sample investigated in the course of my studies is a 1 mm thick single crystal of  $\text{Cu}_3\text{Bi}(\text{SeO}_3)_2\text{O}_2\text{Cl}$ , with its primary face (5 mm  $\times$  5 mm) normal to the  $\hat{c}$ -axis. It was grown using a chemical vapour method, as described in [75].

CBSCl francisite is characterised by a structural transition at  $T_S = 115 \text{ K}$  [132] from the orthorhombic  $Pm\bar{m}n$  space group to the  $Pcmn$  space group [131]. Below  $T_S$ , a doubling of the unit cell with respect to the  $Pm\bar{m}n$  phase is observed [132]. The structure of the low-temperature  $Pcmn$  phase is plotted in Figure 5.1. In the high-temperature phase, layers of a buckled kagome lattice, consisting of  $\text{CuO}_4$  plackets, are stacked along the  $\hat{c}$ -axis and separated by  $\text{SeO}_3$  pyramids. The Bi and Cl atoms are located inside the hexagonal arrangement of the  $\text{Cu}^{2+}$  ions [132]. These copper ions occupy two different inequivalent sites, Cu1 and Cu2 [75]. The spin half magnetic moments of the copper atoms dictate the magnetic properties [133]. Phonon studies of this compound revealed anomalous soft-mode behaviour and were an early indicator of the structural transition in CBSCl [75, 137].

An antiferromagnetic ordering transition is reported below a Néel temperature of  $T_N = 25 \text{ K}$  [133]. The hexagonal arrangement of Cu sites, as mentioned above, forms a layered kagome-like lattice. Dzyaloshinsky-Moriya (details see [138, 139]) interactions lift the frustration, and when introduced, correctly model the stable antiferromagnetic ground state [140]. This is the origin of the frustrated magnetism in francisite [133], since there is competition between ferro- and antiferromagnetic interactions of the Cu1 and Cu2 ions [137, 141, 142]. A more detailed picture of francisite's magnetic behaviour is presented in e.g. [141]. Studies performed by inelastic neutron scattering show that the anisotropy in the interaction energy has to be included to model the spin dynamics correctly [132].

Early suggestions that the low temperature  $Pcmn$  phase could support an antiferroelectric state were first put forward in reference [143]. Indeed, our collaborators from the University of Luxembourg recently identified a non-polar vibrational soft-mode that drives the phase transition at 115 K [144]. In more detail, the authors claim that CBSCl is a Kittel-like example of a displacive antiferroelectric. So far no ferroelectric phase of CBSCl has been reported. However a neighbouring FE phase is a necessary condition for an AFE state. This chapter describes an infrared study, performed to investigate the potential of a close lying ferroelectric state in francisite.



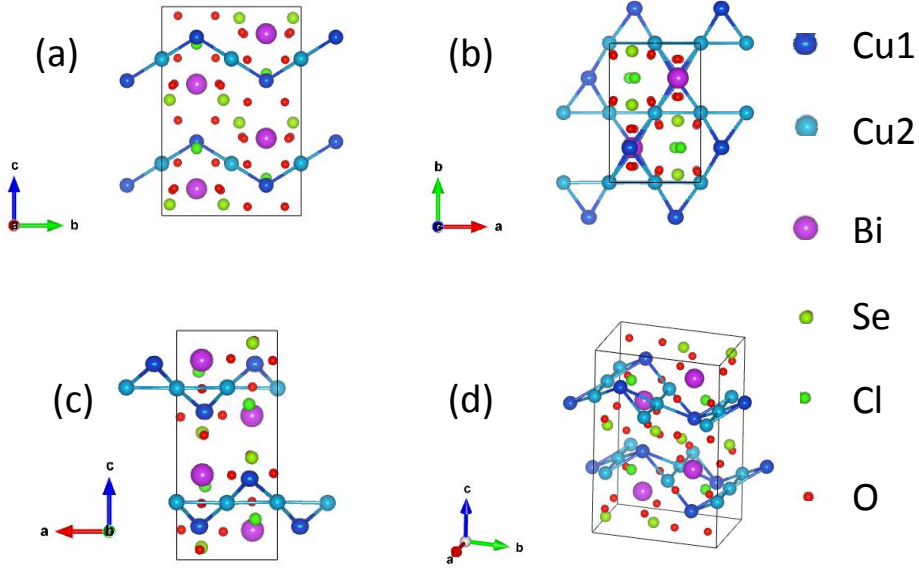


**Figure 5.1:** The low temperature ( $Pcmn$ ) crystalline structure of  $\text{Cu}_3\text{Bi}(\text{SeO}_3)_2\text{O}_2\text{Cl}$ . The pictures are adapted from [132], using the VESTA software [108] and crystalline information from reference [132].

## 5.2 Data treatment

Both the FTIR and the THz-spectrometers were used to study the CBSCL francisite  $c$ -cut sample. Details of the experimental methods are presented in Chapter 3. The infrared reflectance was detected at various temperatures between 10 K and 300 K using the FIR setting of the FTIR spectrometer. Again, data was collected along both crystallographic axes,  $\hat{a}$  and  $\hat{b}$ . Each measurement includes averaging of 100 scans, performed with a 2 mm aperture.

Backward wave oscillators BWO-530 and BWO-800 were used to detect the complex transmission of the sample in two ranges of approximately  $8\text{ cm}^{-1}$  to  $16\text{ cm}^{-1}$  and  $20\text{ cm}^{-1}$  to  $28\text{ cm}^{-1}$ . The sample was mounted on mylar foil and masked with a 4 mm aperture. A picture of this arrangement is shown in Figure 3.11. As described above in Section 3.2.2, the dielectric function can be calculated from this data. This function features a vanishing imaginary component  $\varepsilon_2$ . However, a larger contribution can be observed at 10 K due to an antiferromagnetic excitation. The reflectance  $R$  can easily be calculated using Eq. (2.20),

$$R = \left| \frac{1 - \sqrt{\varepsilon}}{1 + \sqrt{\varepsilon}} \right|^2. \quad (5.1)$$

The RefFIT program [121] was used to merge the reflectance data of both experiments. The reflectance from the FTIR spectroscopy is used in the range from  $50\text{ cm}^{-1}$

to  $700\text{ cm}^{-1}$ . All spectra show an artefact between  $700\text{ cm}^{-1}$  and  $750\text{ cm}^{-1}$  due to a beam splitter minimum in this range. This problem is overcome differently for the two polarisations. For the  $E\parallel\hat{a}$  measurements, the data above  $700\text{ cm}^{-1}$  could not be used at all. However, a spectrum of the MIR setting (a room temperature test) of the spectrometer is added to provide a good high-frequency approximation of the francisite's reflectance of this polarisation. In the other direction, only the reflectance of the artefact was excluded from the fit, with the  $750\text{ cm}^{-1}$  to  $950\text{ cm}^{-1}$  FIR data being included. Another minimum of the beam splitter requires omitting points between  $838\text{ cm}^{-1}$  and  $845\text{ cm}^{-1}$  as well. A comparison of the fit with the raw data is presented in Figure 5.2 for both polarisations.

The FTIR reflectance is superimposed with fringes in the range below  $\sim 400\text{ cm}^{-1}$ . This additional oscillating signal is an artefact due to internal reflections within the thin sample. As a result, performing a Kramers-Kronig analysis of these spectra is more difficult as the fringes in close proximity to phonon excitations can influence the final result. Thus, the reflectance of the fit was used from  $0\text{ cm}^{-1}$  to  $15000\text{ cm}^{-1}$  to calculate the dielectric function in the range from  $0\text{ cm}^{-1}$  to  $3000\text{ cm}^{-1}$  analytically. For this, RefFIT is used to calculate the permittivity. A comparison of the dielectric functions (using the fit and the KK-analysis) shows discrepancies below  $\sim 1\%$  in terms of resonance frequencies. Thus, for simplification, the permittivity determined using the fitting model, is primarily used with the KK-analysis shown as an additional check of the software. A comparison of both models is presented in Appendix A.2.2.

No phonons could be observed at frequencies above  $\sim 950\text{ cm}^{-1}$ . Thus, the broadband spectra, obtained at room temperature do not show any further information. Since the THz-spectrometer was used as well, data of the THz setting of the FTIR spectrometer was not necessary for a good low-frequency approximation of the data.

Static permittivity of the  $\hat{a}$ -axis was obtained using the PPMS and an Alpha-A analyser via capacitive measurements.

## 5.3 Results

### 5.3.1 Reflectance and dielectric function

The first spectroscopic studies on francisite were performed by Miller *et al.* [75] for CBSI and Wang *et al.* [145] for CBSBr in the FIR and THz range. However, detailed report on the low-frequency lattice dynamics across the phase transition is still lacking, although these works did contribute to a better understanding of the francisite structure. Therefore, my studies focus on these low-frequency lattice dynamics, with particular attention on a polar soft mode. Submillimeter THz spectroscopy opens the door to better resolve the dynamics of the lowest frequency phonons.

Figure 5.2 gives an overview of the measured reflectance. Here, the raw data is compared to the fits. The reflectance is shown for four characteristic temperatures. These include 10 K and 300 K (the experimental limits of the setup), as well as 100 K and 120 K (just below and above  $T_S$ ). In general, the reflectance is in nice agreement with the data from Miller *et al.* [75]. A few weak excitations could not be modelled

with stable fits. However, the predicted additional phonons are detected in the low-temperature phase arising around the temperature of the structural phase transition. A detailed list of the phonon frequencies and further fitting parameters is given in Appendix A.2.1.

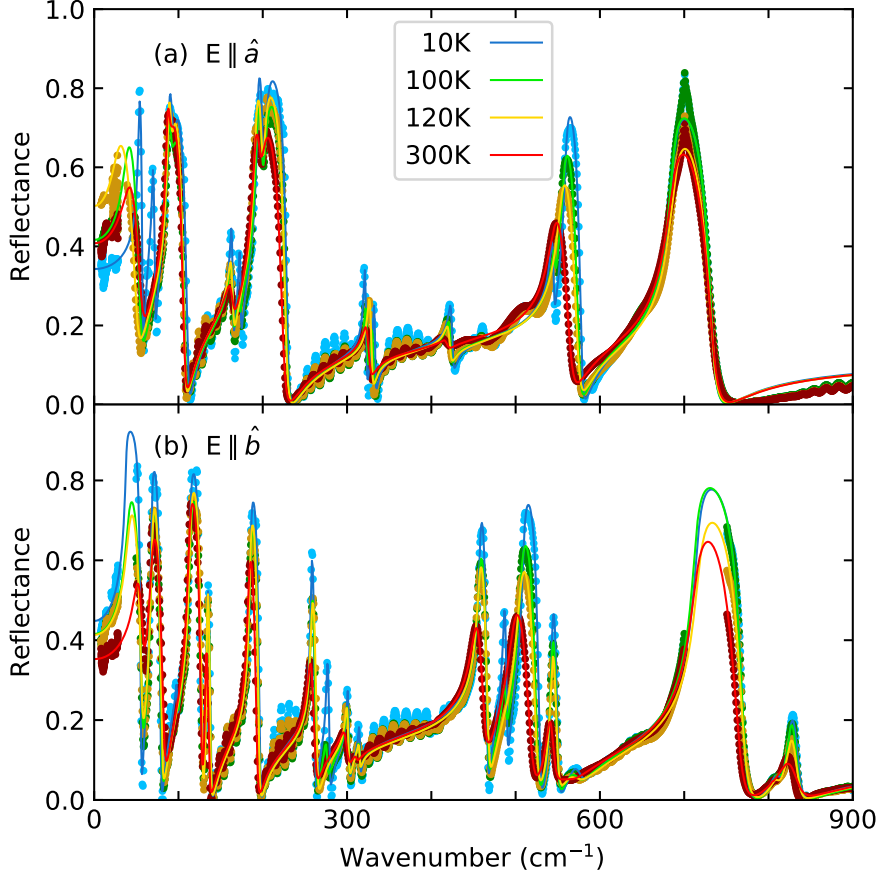


**Figure 5.2:** Far infrared reflectance of CBSCl in the range from  $10 \text{ cm}^{-1}$  to  $900 \text{ cm}^{-1}$ . The  $E \parallel \hat{a}$  polarisation is shown in (a), with  $E \parallel \hat{b}$  shown in (b). Solid lines represent the fit, single points show the raw data from both experiments. Below  $30 \text{ cm}^{-1}$  the data was obtained using THz-spectroscopy, above  $50 \text{ cm}^{-1}$  FTIR spectroscopy is used.

This work aims to highlight the role of the lattice dynamics in the sub-THz regime across the structural phase transition. Therefore, a more detailed picture of the results is given in Figure 5.3, covering the range below  $120 \text{ cm}^{-1}$ . The zoomed-in reflectance is shown in Figures 5.3(a) and (d).

The dielectric function can provide a more clear picture of the lattice dynamics, as shown in Figure 5.3(b,c,e,f). The real and imaginary parts of both polarisations are shown here in the zoomed range below  $120 \text{ cm}^{-1}$  (full spectra are shown in Appendix A.2.2). Figures 5.3(b) and (e) show  $\varepsilon_1$ , the real component of the dielectric function. From this, the values for static permittivity ( $\varepsilon(0)$ ) can be extracted. The

$E\|\hat{b}$  polarisation shows an increase of this property for lowering temperature. The main contribution to static permittivity for  $E\|\hat{a}$  is the lowest frequency phonon. Here, a more interesting temperature dependency is observed. When cooling down from room temperature to  $T_S$ ,  $\varepsilon(0)$  almost doubles. At temperatures below  $T_S$ , it then decreases rapidly again (see Figure 5.4(c)). The imaginary part of the dielectric function gives information about the phonon frequencies and is plotted in Figures 5.3(c) and (f). Both polarisations are characterised by anomalous low-frequency phonons occurring at  $\sim 45 \text{ cm}^{-1}$ . These phonons are labelled as  $\bar{\nu}_F$  for  $E\|\hat{a}$  and  $\bar{\nu}_0$  for  $E\|\hat{b}$ , respectively. A strong softening can be observed for both excitations with decreasing temperature. While  $\bar{\nu}_0$  softens monotonically for lower temperatures,  $\bar{\nu}_F$  reaches its minimum frequency at  $T_S$ , it then hardens for temperatures below  $T_S$ . Also the second lowest phonon (labelled as  $\bar{\nu}_1^a$  and  $\bar{\nu}_1^b$ , respectively) is seen to occur at a similar frequency ( $\sim 75 \text{ cm}^{-1}$  at 10 K) in both directions. While for  $E\|\hat{b}$  the frequency stays stable, a softening can be seen for  $E\|\hat{a}$  with increasing temperature towards  $T_S$ . Finally this oscillator cannot be resolved above 80 K.

### 5.3.2 Fits

The fitting parameters, including the wavenumber  $\bar{\nu}$ , damping constant  $\gamma$  and resulting dielectric contribution  $\Delta\varepsilon$ , are plotted as a function of temperature in Figure 5.4. The resonance frequencies are summarised in Figures 5.4(a) and (d). Here, it is clear that the dynamics of the  $\bar{\nu}_F$  and  $\bar{\nu}_0$  modes are, in comparison with the other phonons, unique. Only those two phonons show a change of more than 5% in frequency.

The damping of  $\bar{\nu}_F$ , denoted as  $\gamma_F$  (Figure 5.4(b)), also shows a unique behaviour. Below  $\sim 40 \text{ K}$  it stays constant at  $\sim 2 \text{ cm}^{-1}$ . From here on, the damping constant increases by a factor  $\sim 7$  while temperature approaches  $T_S$ . In the high temperature phase,  $\gamma_F$  remains almost constant. A similar behaviour can be seen for  $\bar{\nu}_0$  (see Figure 5.4(e)). Here again, the damping increases strongly between 40 K and  $T_S$ , although the final jump is much weaker.

Figures 5.4(c) and (f) deal with the static permittivity,  $\varepsilon(0)$ . According to Eq. (2.41) this is the sum of all the oscillator's dielectric contributions plus  $\varepsilon_\infty$ , the high frequency permittivity:

$$\varepsilon(0) = \varepsilon_\infty + \sum_i \frac{\bar{\nu}_{p,i}^2}{\bar{\nu}_i^2} = \varepsilon_\infty + \sum_i \Delta\varepsilon_i. \quad (5.2)$$

In both polarisations, the main contribution comes from the lowest frequency oscillator. Along the  $\hat{a}$ -axis,  $\Delta\varepsilon_F$  has its minimum at the base temperature. It then strongly increases by a factor larger than 6 to reach its maximum at  $T_S$ . From here, it then decreases for higher temperatures. The total static permittivity appears to be shifted by a constant value above the contribution from this single phonon contribution. This is a result of the small and mostly independent contributions from all other oscillators. The property  $\varepsilon^a(0)$  was measured additionally with the PPMS.

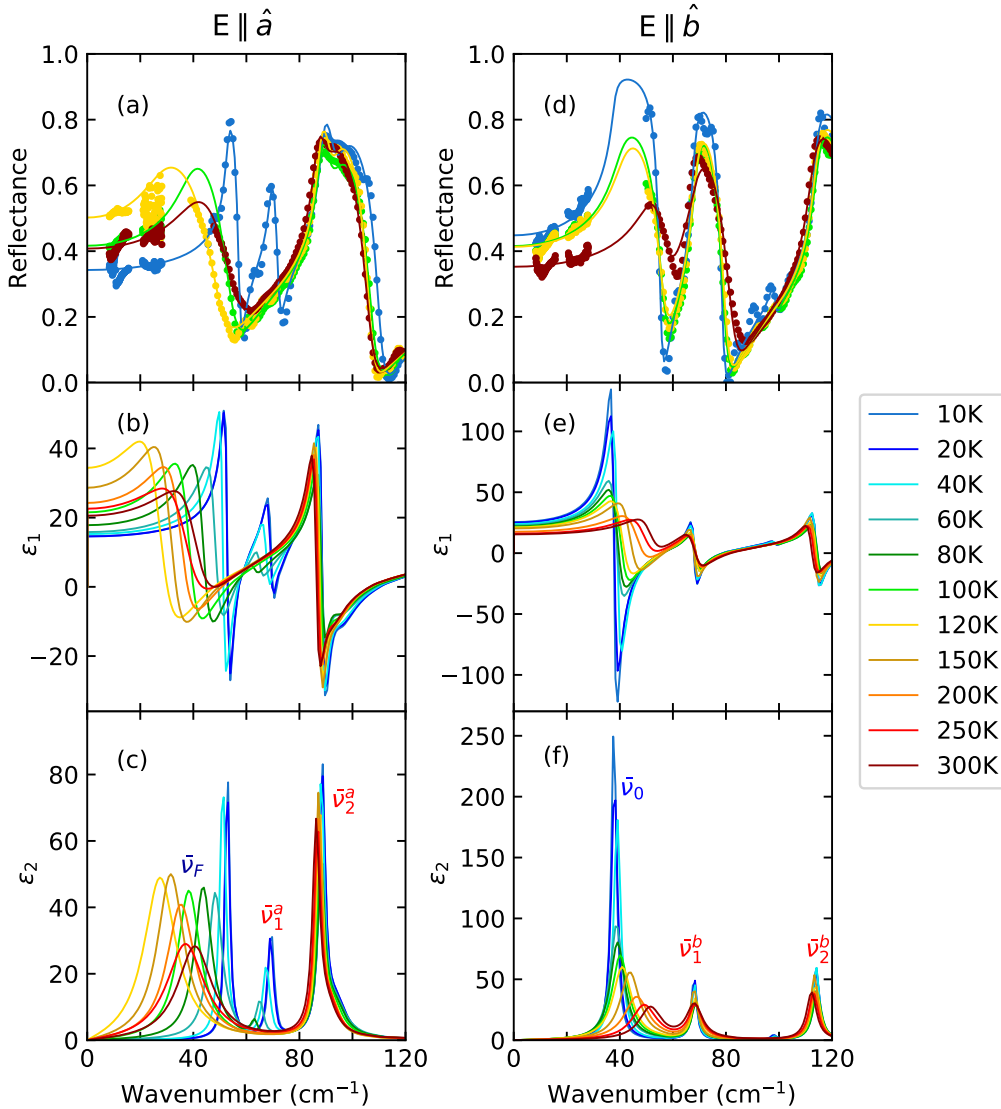


**Figure 5.3:** Far infrared reflectance and complex permittivity of CBSCl in the range below  $120 \text{ cm}^{-1}$  as a function of temperature. Full lines represent the fits, single data points show the experimental measurements. The left column shows these properties for  $E \parallel \hat{a}$  and the right one for  $E \parallel \hat{b}$ . (a) and (d) show reflectance data, (b) and (e) the real part of the dielectric function,  $\epsilon_1$ . Note that in (b) the maximum of the static permittivity is at 120 K, close to the temperature of the structural phase transition,  $T_S = 115 \text{ K}$ . The imaginary part,  $\epsilon_2$ , of the dielectric function is presented in (c) and (f). The labels indicate the low-frequency phonons found in each polarisation.

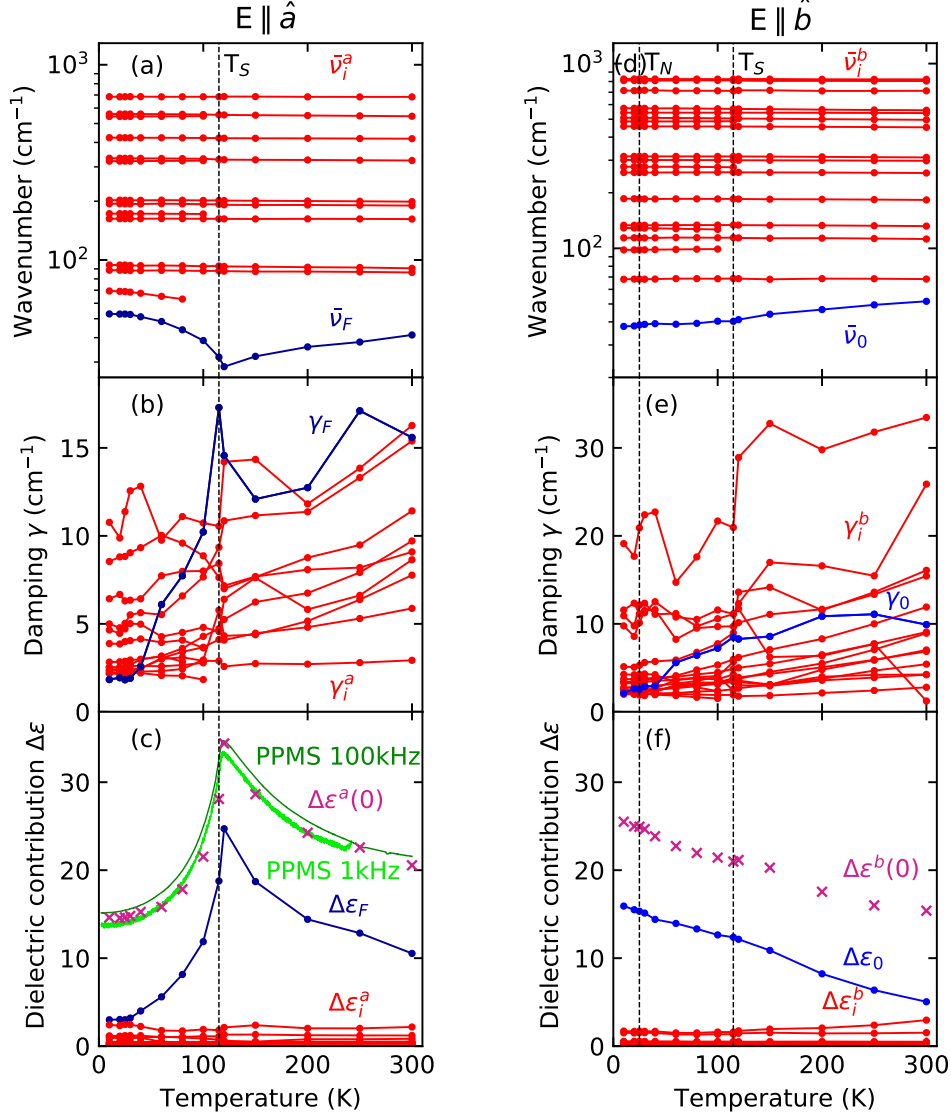


**Figure 5.4:** Fitted properties of the CBSCl oscillators as a function of temperature (left column (a-c):  $E \parallel \hat{a}$ , right column (d-f):  $E \parallel \hat{b}$ ). The dynamics of  $\bar{\nu}_F$  and  $\bar{\nu}_0$  are highlighted in blue. The softening of these lowest frequency modes in comparison to the other stable modes can be seen in (a) and (d), respectively. The damping constant  $\gamma$  of the oscillators is shown in (b) and (e). The dielectric contribution and static permittivity are plotted in (c) and (f).

In the PPMS, scans were performed at two frequencies (1 kHz and 100 kHz) and result in values almost identical to the data extracted from the phonon spectra indicating that no further dielectric contributions exist below the lattice dynamics.

For  $E \parallel \hat{b}$  the shape of the lowest oscillator's dielectric contribution,  $\Delta\varepsilon_0$ , differs to the other phonons, which also are mostly constant.  $\Delta\varepsilon_0$  shows a mostly monotonic decrease reaching half of the 10 K value at room temperature. The extracted static permittivity follows this trend.

### 5.3.3 Antiferroelectricity

Previously, I mentioned that the structural transition in CBSCl highlights a rare example of a fully displacive transition, as reported in reference [144]. In this section a brief review on antiferroelectricity will be given, which is necessary for the understanding of the further discussion of my results.

Charles Kittel formulated one of the first concepts of antiferroelectric (AFE) crystals [146]. According to his theory there have to be two sublattices ( $A$  and  $B$ ) of spontaneous antiparallel polarisation  $P$ , such that the net polarisation is equal to zero. Then the local forces on the sublattices can be expressed by [146]:

$$F_A = E + \beta_1 P_A - \beta_2 P_B, \quad (5.3)$$

$$F_B = E + \beta_1 P_B - \beta_2 P_A, \quad (5.4)$$

with  $E$  representing an external electric field and  $\beta$  the so called Lorentz constants. Furthermore, the Helmholtz free energy,  $F$ , can be written as [146]

$$F(P_A, P_B, T) = F_0 + f(P_A^2 + P_B^2) + gP_A P_B + h(P_A^4 + P_B^4). \quad (5.5)$$

The functions  $f, g, h$  depend on temperature. Again, the polarisation is the order parameter, in analogy to FE.

Antiferroelectricity is a controversial topic, as e.g. Scott [147] discussed: “*And in general one cannot characterize a crystal at one temperature as antiferroelectric by any set of experimental measurements at that temperature. The opinion of this reviewer is that antiferroelectricity is an ill defined, almost useless concept.*” One of the reasons was the lack of an order parameter and of clear symmetry criteria defining this phase [148]. At this time only a set of experimental signatures defines this phase. One of these signatures is a characteristic double hysteresis loop [148–151], as shown in Figure 5.5.

Lines and Glass defined an antiferroelectric system as [153] “*that fraction of antipolar systems which exhibits large dielectric anomalies near the Curie temperature [...] and which can be transformed to an induced ferroelectric phase by application of an electric field.*” This already states that a FE phase is close by, that is exclusively field induced. But here again, the definition is based on experimental signatures.

In a theory by Tolédano and Guennou [148] one condition for the transition from paraelectric to AFE state is that “*a set of crystallographic sites undergo a symmetry lowering that results in the emergence of polar sites and give rise to a local polariza-*



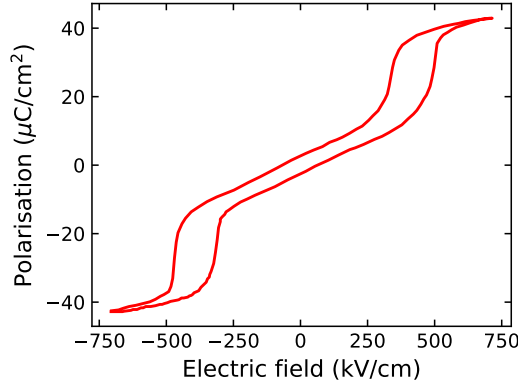


**Figure 5.5:** Antiferroelectric double hysteresis loop of  $\text{PbZrO}_3$ , data from reference [152].

tion.” This already defines a local mechanism of symmetry breaking and corresponds with the emergence of polar sites. A second criterion of these authors states for the macroscopic symmetry: “the AFE space-group has a symmorphic polar subgroup coinciding with the local symmetry of emerging polar sites.” This is the first formulation of local and macroscopic symmetry conditions for the AFE transition.

In their theory, the Landau potential is a function of the AFE order parameter  $\eta$  (which covers structural effects) and the polarisation  $P$  as a second, field-induced order parameter [148],

$$\phi(\eta, P, T) = \phi_0(T) + \frac{\alpha}{2}\eta^2 + \frac{\beta}{4}\eta^4 + \frac{\gamma}{6}\eta^6 + \frac{P^2}{2\chi_0} + \frac{\delta}{2}\eta^2 P^2 - EP, \quad (5.6)$$

with  $\alpha = A(T - T_S)$ . All other material constants remain independent of temperature. This theory now includes the coupling effects between the AFE order parameter  $\eta$  and the field-induced order parameter  $P$ .

One of the first materials where antiferroelectric signatures were observed was  $\text{PbZrO}_3$  which was intensively studied over the last 70 years [154–159]. Possible applications of AFE materials are liquid crystal displays [160–162] and energy storage devices [163–165]. In the last decades many AFE transitions were reported showing signatures of both order-disorder and displacive behaviour [166–169]. While examples of pure order-disorder transitions have been studied [170–172], clear evidence of purely displacive antiferroelectric systems has been missing. Recently the orthorhombic francisite ( $\text{Cu}_3\text{Bi}(\text{SeO}_3)_2\text{O}_2\text{Cl}$ ) was identified as the first soft-mode driven displacive antiferroelectric [144].

### 5.3.4 Ferroelectric signature of a soft mode

Now, the concept of antiferroelectricity (AFE) was introduced and here I mentioned that a close by lying ferroelectric (FE) phase is a necessary condition for an AFE



state. Cochran's law, Eq. (2.48), states that the frequency of the FE soft mode is proportional to the difference of temperature  $T$  and the Curie temperature  $T_C$ . In this section, I will show a verification of how the  $\bar{\nu}_F$  soft mode found in francisite represents a close lying ferroelectric transition. The linear fits of

$$\bar{\nu}^2 = A(T - T_C), \quad (5.7)$$

were performed for both the  $\bar{\nu}_F$  (representing a ferroelectric phase) and  $\bar{\nu}_{AF}$  (representing the soft mode of the AFE transition) mode, with  $A$  and  $T_C$  the parameters to be fit individually at low and high-temperatures across the phase transition. The  $\bar{\nu}_{AF}$  data has been obtained using Raman spectroscopy and inelastic X-ray scattering techniques and was extracted from reference [144]. Figure 5.6 shows both data sets as a function of temperature. The fit of the AFE mode crosses the baseline at 112 K, close to  $T_S = 115$  K. This corresponds with the minimum of  $\bar{\nu}_{AF}$  being approaching zero. The infrared FE mode softens considerably less. The fit of the high-frequency part intercepts the baseline at  $-59$  K. This is far below any transition temperature, but is reminiscent of the inverse magnetic susceptibility following the Curie-Weiss law in an antiferromagnet.

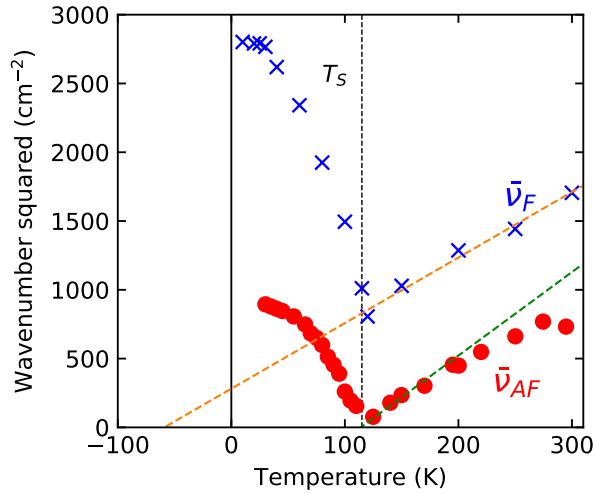


**Figure 5.6:** Analysis of the squared frequency for the  $\bar{\nu}_F$  and  $\bar{\nu}_{AF}$  modes. Data for  $\bar{\nu}_{AF}$  excitation is extracted from reference [144]. The dashed lines represent linear fits using Eq. (5.7).

In the chapter on langasites (page 55), a model is introduced that approximates the electric field strength,  $E$ , necessary to overcome an energy gap. Here,

$$E = W_0 \frac{2\pi}{a} \frac{1}{Q}, \quad (5.8)$$

with  $W_0$ , the energy gap (59 K times  $k_B$ ), a lattice parameter  $a \sim 0.6$  nm, and  $Q$ , twice the elementary charge (charge of the frustrated  $\text{Cu}^{2+}$  ions). This leads to electric fields in the order of  $3 \cdot 10^7$  V/m to reach a positive critical temperature and additional

$\sim 6 \cdot 10^7$  V/m to pass the structural transition at  $T_S$ . These values of electric fields are far above the realisation limits of the PPMS. The AFE mode is located on the boundary of the Brillouin zone [144], while  $\bar{\nu}_F$  represents a zone-center mode.

### 5.3.5 Sublattice polarisation

In this section, I want to explore a model using the  $\bar{\nu}_F$  and  $\bar{\nu}_{AF}$  dynamics to extract a possible sublattice polarisation that characterises the antiferroelectric (AFE) phase. A model, comparing the polarisation in the ferro- and antiferroelectric phase, is presented in Figure 5.7.

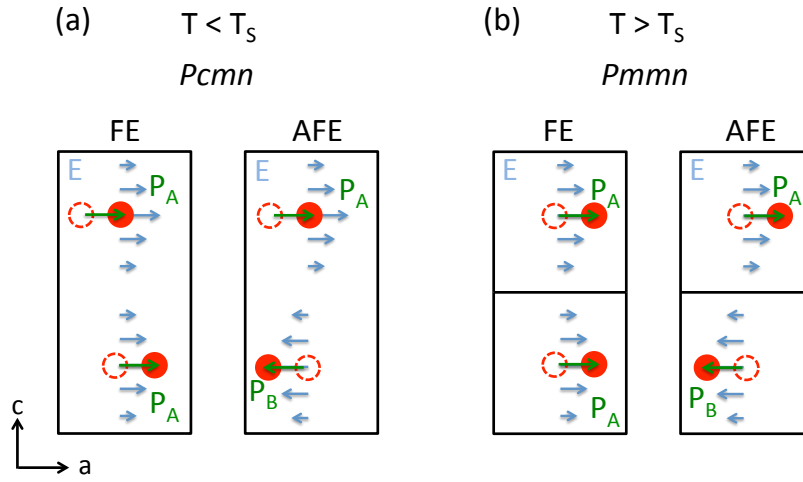


**Figure 5.7:** Picture of the local depolarising fields,  $P_A$  and  $P_B$ , of the  $\bar{\nu}_F$  and  $\bar{\nu}_{AF}$  phonon. The low-temperature phase is plotted in (a), the high-temperature phase in (b). The red circles represent the Cu ions.

From Section 2.3.1 we know that  $\bar{\nu}_F^2$ , the soft mode of the FE transition, has to be proportional to the sum of short range restoring forces  $R_0$  and the local Coulomb forces. Thus, I start with adapting Eq. (2.47),

$$\bar{\nu}^2 \propto \left( \sum_j R_{ij} X_j - q_i E_0 \right) / (m_i X_i), \quad (5.9)$$

and replace the electric field with the depolarising field  $P_0 = \varepsilon E_0$  of the phonon. Now, the substitutions,

$$R_0 = \sum_j R_{ij} X_j / (m_i X_i) \quad \text{and} \quad P = q_i P_0 / (m_i X_i \varepsilon), \quad (5.10)$$

yield

$$\bar{\nu}^2 \propto R_0 - P. \quad (5.11)$$

In the ferroelectric domain, only the  $P_A$  field plays a role, thus

$$\bar{\nu}_F^2 \propto R_0 - P_A. \quad (5.12)$$

The  $\bar{\nu}_{AF}$  mode is identified at the boundary of the Brillouin zone. It depends now on both fields,  $P_A$  and  $P_B$  and can be described by a molecular field,  $\eta$ , such that,

$$\bar{\nu}_{AF}^2 \propto R_0 - \eta. \quad (5.13)$$

Both modes,  $\bar{\nu}_F$  and  $\bar{\nu}_{AF}$ , represent the movement of the same ions, just in a different phase. Thus, I assumed (due to the symmetry)  $R_0$  to be equal for both structures. The ratio of these properties can now be easily calculated via

$$\frac{\bar{\nu}_F^2}{\bar{\nu}_{AF}^2} \propto \frac{R_0 - P_A}{R_0 - \eta}, \quad (5.14)$$

which is plotted in Figure 5.8(a). In the paraelectric phase ( $T > T_S$ ), the ratio becomes  $\bar{\nu}_F^2/\bar{\nu}_{AF}^2 \approx 2$  and in the low temperature phase,  $\bar{\nu}_F^2/\bar{\nu}_{AF}^2 \approx 3$ . At  $T_S$ , the divergence at the critical temperature can be described by  $\bar{\nu}_{AF}$  approaching 0, such that

$$\eta \rightarrow R_0 \Big|_{T \rightarrow T_S}. \quad (5.15)$$

The shape of this ratio as a function of temperature looks like the Greek letter  $\lambda$  and indicates a 2<sup>nd</sup> order transition as one might expect for the susceptibility. Thus, this ratio is somehow connected to the order parameter of the transition. The difference between the squared frequencies is given by,

$$\bar{\nu}_F^2 - \bar{\nu}_{AF}^2 = R_0 - P_A - R_0 + \eta = \eta - P_A. \quad (5.16)$$

Figure 5.8(b) shows this difference as a function of temperature. A constant value can be observed above  $T_S$  and an increase for temperatures below  $T_S$ . The shape of these data points looks as one expect for the order parameter (see Figure 2.5(b)) when adding a constant underground. Thus, the low-temperature data was fitted with the function

$$\eta - P_A = a\sqrt{T_S - T} + b, \quad (5.17)$$

(with  $a$  and  $b$  being fitting parameters) that is plotted on top of the measured data points. A good agreement can be seen. This is a further hint that  $\eta$  is the order parameter of this transition.

Now, I assume

$$\eta = P_A + P_B, \quad (5.18)$$

such that,

$$\bar{\nu}_F^2 - \bar{\nu}_{AF}^2 = \eta - P_A = P_A + P_B - P_A = P_B. \quad (5.19)$$

Now, the ratio is identical to a single depolarising field and we can learn about the change in the sublattice polarisation. It is constant in the high-temperature phase and increases for temperatures below the transition. Unfortunately, values of  $\bar{\nu}_{AF}^2$

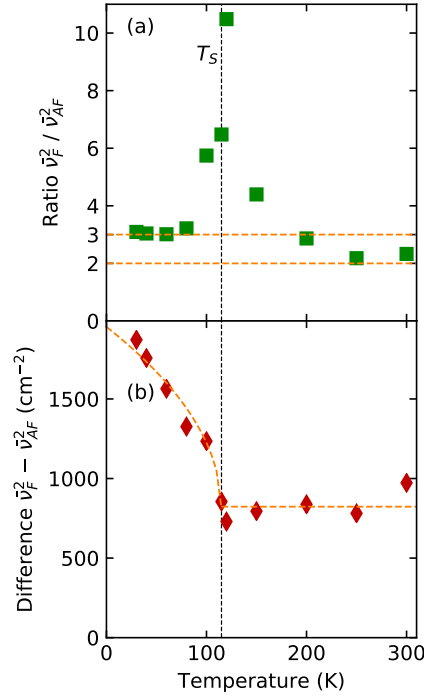


**Figure 5.8:** Analysis of squared frequency for  $\bar{\nu}_F$  and  $\bar{\nu}_{AF}$  modes. Data for  $\bar{\nu}_{AF}^2$ -excitation extracted from [144]. (a) The ratio  $\bar{\nu}_F^2/\bar{\nu}_{AF}^2$ . Dashed orange lines represent the low and high temperature approximation. (b) The difference between the squared frequencies,  $\bar{\nu}_F^2 - \bar{\nu}_{AF}^2$ . The dashed curve is a fit,  $\sim \sqrt{T_S - T}$  below  $T_S$  and constant above  $T_S$ .

could not be extracted below 30 K, such that the temperature is probably too high to observe a stabilisation of the sub lattice polarisation.

While this simple model contains a general hand-waving argument, it is nice to see that with a few simple assumptions the experimental data reveals some deeper concepts about the nature of AFE transitions.

### 5.3.6 Spin-lattice effects in $\hat{b}$ -direction

A side remark on the  $\hat{b}$ -direction is necessary, although the AFE behaviour occurs along the  $\hat{a}$ -direction. Figures 5.3(f) and 5.4(d) show a softening of the lowest frequency phonon mode ( $\bar{\nu}_0$ ). This can be seen as an indicator for an additional lattice instability, not concerning the antiferroelectric transition. At the base temperature of the experiments (10 K) a value of  $\bar{\nu}_0 \sim 38 \text{ cm}^{-1}$  can be observed, this temperature correlates with its maximum in intensity. In fact, this frequency lies close to an anti-ferromagnetic spin wave excitation (at  $\sim 33 \text{ cm}^{-1}$ ), reported in [75]. The close lying nature of the two modes and the increase in spectral weight below  $T_N$  could be a hint for a possible spin-lattice coupling.

A further hint can be observed in the static permittivity (Figure 5.4(f)). As al-

ready mentioned,  $\varepsilon(0)$  decreases monotonically with temperature. But a weak step can indeed be observed between 30 K and 40 K. This effect is close to  $T_N = 25$  K, maybe because of the coupling to the magnetic mode. Furthermore, the effects of potential spin and lattice interactions should be considered in relation to explaining the anomalous exchange interactions as reported in [132].

## 5.4 Summary

Magnetically frustrated francisite ( $\text{Cu}_3\text{Bi}(\text{SeO}_3)_2\text{O}_2\text{Cl}$ ) was studied using FTIR and sub-THz spectroscopy. The reflectance and dielectric function were presented and the phonons were fitted with Lorentzian oscillators. An overview on the lattice dynamics is presented, with focus given to the lowest frequency modes.

The lowest mode for  $E\|\hat{a}$  polarisation softens from both sides towards  $T_S$ , the temperature of a structural transition. This soft mode,  $\bar{\nu}_F$ , resembles Cochran's description of a displacive ferroelectric phase transition. Together with its dynamics in the AFE state, this mode fits a model describing a displacive antiferroelectric phase. An energy gap of  $\sim 5$  meV is observed.

The dynamics of the  $\bar{\nu}_F$  and  $\bar{\nu}_{AF}$  modes may reveal information about a sublattice polarisation, a further requirement of an AFE state. The difference of the squares of these two modes,  $\bar{\nu}_F^2 - \bar{\nu}_{AF}^2$ , can indeed providing signature of the order parameter of the AFE transition.

Hints for a possible spin lattice coupling could be observed for  $E\|\hat{b}$  phonons. The spin lattice interaction can induce the anomalous anisotropic magnetic coupling. Thus, these excitations could have a magnetic and AFE origin and make CBSCl to a new type of multiferroic.



---

# 6

## Phonon splitting in vibronic spin-liquid candidate $\text{Tb}_2\text{Ti}_2\text{O}_7$

---

This chapter covers the study of materials of the pyrochlore supergroup ( $A_2B_2O_7$ ). Rare-earth pyrochlore single crystals of  $\text{Tb}_2\text{Ti}_2\text{O}_7$  and  $\text{Ho}_2\text{Ti}_2\text{O}_7$  are investigated with infrared spectroscopy and their results are compared. The aim is to gain a better understanding of the lattice environment that hosts the frustrated spin network, and which is responsible for a likely vibronic spin-liquid phase in  $\text{Tb}_2\text{Ti}_2\text{O}_7$ . These results are then also compared with a powder pellet sample of  $\text{Tb}_2\text{Sn}_2\text{O}_7$  pyrochlore.

### Contents

---

<b>6.1</b>	<b>Introduction</b>	<b>86</b>
6.1.1	The pyrochlore group and its structure	86
6.1.2	Spin-ice states in pyrochlores	86
6.1.3	The pyrochlore $\text{Tb}_2\text{Ti}_2\text{O}_7$	89
<b>6.2</b>	<b>Analysis</b>	<b>92</b>
<b>6.3</b>	<b>Results</b>	<b>92</b>
6.3.1	$\text{Ho}_2\text{Ti}_2\text{O}_7$ (HTO)	92
6.3.2	$\text{Tb}_2\text{Ti}_2\text{O}_7$ (TTO)	95
6.3.3	$\text{Tb}_2\text{Sn}_2\text{O}_7$ (TSO)	98
<b>6.4</b>	<b>Discussion and Summary</b>	<b>100</b>

---

## 6.1 Introduction

### 6.1.1 The pyrochlore group and its structure

The pyrochlore supergroup covers minerals of the chemical formula  $A_{2-m}B_2X_{6-n}Z_{1-w}$  where the parameters  $m, n, w$  are used to describe impurities [173]. In my thesis this is mainly limited to materials of the type  $A_2B_2O_7$ . Minerals with  $B=\text{Nb}$  in the chemical formula above are members of the pyrochlore group, one of five subgroups of the pyrochlore supergroup [174]. The term pyrochlore was also used for minerals<sup>15</sup> with a chemical formula  $(\text{Ca,Na})_2(\text{Nb,Ta})_2\text{O}_6(\text{O,OH,F})$  [175], the first one -  $\text{NaCaNb}_2\text{O}_6\text{F}$  - was discovered by Wöhler almost 200 years ago [176]. This material burns with a yellow/green flame on ignition, thus the word pyrochlore represents a merger of the Greek expressions  $\pi\tilde{\upsilon}\rho$  (fire) and  $\chi\lambda\omega\rho\acute{o}\varsigma$  (green) [176, 177]. Nowadays, the term should not be used for these minerals anymore [173]. The right nomenclature of these and many other materials within the pyrochlore supergroup is covered in [173, 178]. In the following, I will use the term pyrochlore for the materials of  $A_2B_2O_7$  type.

Most of the pyrochlores crystallise in the cubic  $Fd\bar{3}m$  space group [179, 180], this structure is depicted in Figure 6.1(a). In  $A_2B_2O_7$  pyrochlores, different oxidation states of the cations are possible, such as  $A_2^{3+}B_2^{4+}O_7$  and  $A_2^{2+}B_2^{5+}O_7$  [181]. The  $A$  sites are eight-coordinated and surrounded by six  $X$  and two  $Z$  ions (forming a scalenohedra – a distorted cube). There is a shorter distance between the  $A$  and  $Z$  ions [181]. The  $A$  cations form tetrahedra, with the  $Z$  anion located in the center [181]. This network of corner-sharing tetrahedra, sometimes referred as the “pyrochlore structure”, is depicted in Figure 6.1(b). The  $B$  cations are located between six equally distanced  $X$  anions forming a network of corner-sharing  $BX_6$  polyhedra [182]. The arrangement of the  $B$  sites is tetrahedral and identical to the corner-sharing network of the  $A$  sites [183]. This network of corner-sharing tetrahedra is indeed the prototype of a three dimensional frustrated lattice [7].

The ferroelectric behaviour of  $\text{Cd}_2\text{Nb}_2\text{O}_7$  and other pyrochlores was an early interest of modern research [184, 185]. Due to their strongly frustrated lattice, rare-earth pyrochlores exhibit a large variety of exotic physical states, such as spin glass (typically  $A_2\text{Mo}_2\text{O}_7$ ) [186–190], while  $\text{Tb}_2\text{Ti}_2\text{O}_7$  and other rare-earth pyrochlores show signatures of spin liquid behaviour<sup>16</sup> [192–196]. The specific low temperature phase of  $\text{Tb}_2\text{Ti}_2\text{O}_7$  will be discussed in Section 6.1.3. One of the most well known phases, the spin ice (first discovered in  $\text{Ho}_2\text{Ti}_2\text{O}_7$  [197]), is discussed in more detail in Section 6.1.2.

### 6.1.2 Spin-ice states in pyrochlores

The term spin ice identifies magnetic materials with highly degenerate ground states dictated by local organising principles in analogy to how water ice freezes at low tem-

<sup>15</sup>Different authors use different definitions. I took the most common.

<sup>16</sup>In a spin liquid the spins are highly correlated, but still fluctuating (either classically or quantised) at zero temperature [6]. This state was first predicted by Anderson [191].



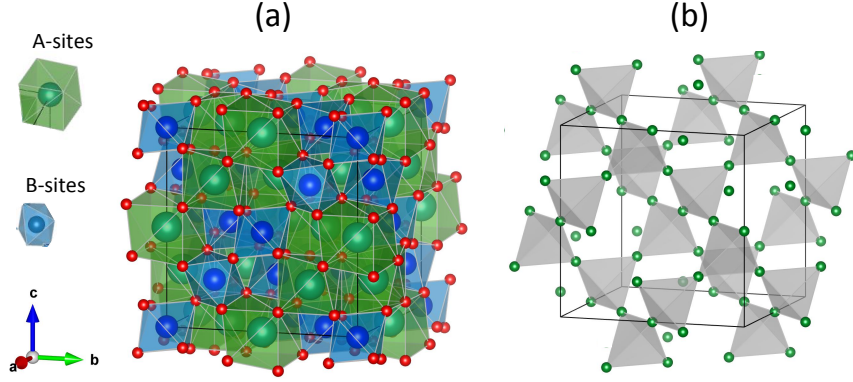


**Figure 6.1:** The pyrochlore lattice: (a) crystalline structure, (b) tetrahedra network of  $A$ -sites. Plotted using the Vesta software [108] and crystalline information from reference [179] for the example of  $Ca_2Nb_2O_7$ . Note that the corners of the polyhedra are occupied by  $O^{2-}$  ions in (a) and with  $A$ -site ions in (b).

peratures [5]. Linus Pauling reported in 1935, how the  $H_2O$  molecules arrange in such a way that each oxygen atom is surrounded by four hydrogen atoms like the corners of a tetrahedron [198]. Since two of the H-O bonds are always (randomly) shorter than the other two (two-near/two-far rule, see ice-rule [199], also Figure 6.2(a)), a degeneracy of possible ground states can be observed even at absolute zero temperature [198]. This so-called zero-point or residual entropy of water was experimentally confirmed via measurements of the heat capacity [200, 201]. In a theoretical approach one can use Boltzmann's expression of the connection between entropy  $S$  and  $\Omega$ , the number of microstates, given by [202]

$$S = k_B \ln(\Omega), \quad (6.1)$$

with  $k_B$  being the Boltzmann constant. Now, there are six possible arrangements of the protons around the oxygen atom in the tetrahedron in agreement with the two-near/two-far rule. This can be estimated by plotting<sup>17</sup> all possibilities (Figure 6.3). Now, the four possible orientations of the tetrahedra have to be taken into account, such that [198]

$$\Omega = (6/4)^n, \quad (6.2)$$

with  $n$  the number of tetrahedra. Now, I define  $N = 2n$ , the number of  $H_2O$  molecules

<sup>17</sup>Another way is to use combinatorics. The number of permutations to fill four spots with two objects of type A and two objects of type B is

$$\binom{4}{2} = \frac{4!}{(4-2)!2!} = \frac{4!}{2!2!} = \frac{24}{4} = 6.$$

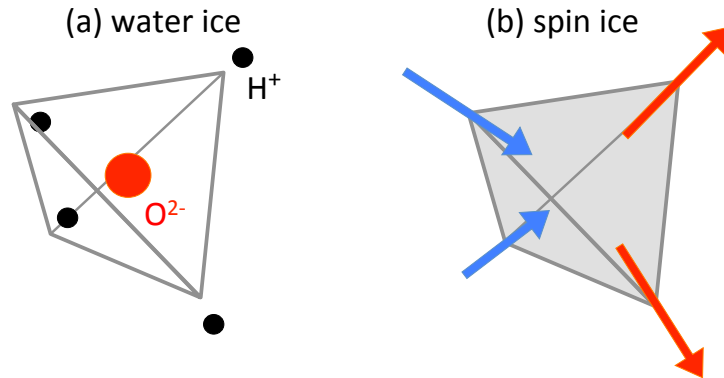


**Figure 6.2:** Visualisation of a tetrahedron in water ice (a) and spin ice (b) as a result of the 2-in/2-out local organising principle.

in the macroscopic crystal, and the entropy becomes, according to Pauling [198],

$$S = k_B N/2 \ln(3/2). \quad (6.3)$$

One important connection between water ice and a spin ice is that this zero-point entropy can be measured in both systems [203]. In a spin ice the magnetic moments of a frustrated structure come into play, which is described in the example of the tetrahedral structure of pyrochlores. While in water ice the two possibilities of the hydrogen ions are ‘near’ and ‘far’, spins can order pointing towards ‘in’ or away ‘out’ from the center of a tetrahedron. Now in analogy to the two-near/two-far rule of water ice, a two-in/two-out arrangement of the spins can be seen in a spin ice (Figure 6.2(b)) and the same six arrangements are possible (see Figure 6.3). Spin ice only occurs for pyrochlores with local  $\langle 111 \rangle$  Ising axes that are a result of the crystal field anisotropy [180, 204].

P.W. Anderson first reported a model of antiferromagnetic ordering in pyrochlores as having a magnetic analogy to Pauling’s model of water ice [205]. However, this model leads to a situation with all spins pointing ‘in’ or ‘out’ [206]. Further, this Ising ‘up/down’ based model by Anderson does not fit with the symmetry of the pyrochlore lattice [207]. A two-in/two-out ordering of the spins along the required local  $\langle 111 \rangle$  directions of the tetrahedra can only be achieved by reversing the sign of the nearest neighbour interaction, such that it occurs only for ferromagnetic interactions [208].

In the classical pyrochlore spin ice, only the rare-earth elements, which are located on the corners of the tetrahedra, have magnetic moments [6]. Historically in 1997,  $\text{Ho}_2\text{Ti}_2\text{O}_7$  was found to be the first material to exhibit spin-ice properties [197]. In the following years spin-ice behaviour was found and intensively studied in other compounds of the rare-earth pyrochlore family, such as  $\text{Ho}_2\text{Sn}_2\text{O}_7$  [209, 210] and  $\text{Dy}_2\text{Ti}_2\text{O}_7$  [203, 211]. Spin ice was further seen in artificial materials, e.g. kagome nano structures [212] and single-domain ferromagnetic islands [213, 214].

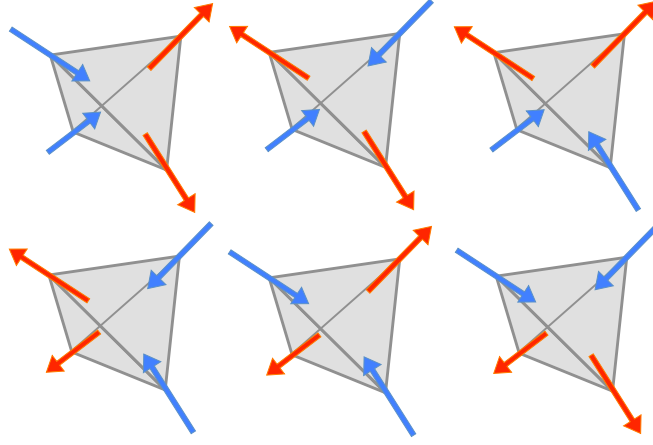


**Figure 6.3:** Visualisation of six possible arrangements of four spins on the corners of a tetrahedron in a spin ice, following the 2-in/2-out ordering. For water ice imagine to replace the arrows by  $H^+$  ions, always located on the arrow's head and situate the  $O^{2-}$  ions in the tetrahedron's center.

### 6.1.3 The pyrochlore $Tb_2Ti_2O_7$

The exact nature of the ground state of  $Tb_2Ti_2O_7$  is still debated [22, 215–222]. A brief overview is given in this section. First, I want to recapitulate the influence of the exchange energy  $J$ . Let us assume, the spins  $\mathbf{S}_i$  are fixed along the local  $\langle 111 \rangle$  directions of the tetrahedra such that their Hamiltonian,  $\mathcal{H}$ , (limited to nearest neighbour interactions) can be expressed as

$$\mathcal{H} = -J \sum_{\langle i,j \rangle} \mathbf{S}_i \cdot \mathbf{S}_j. \quad (6.4)$$

Dipolar interactions can be included by modifying the Ising exchange Hamiltonian, Eq. (6.4), to give the spin-ice Hamiltonian [223]:

$$\mathcal{H} = \underbrace{-J \sum_{\langle i,j \rangle} \mathbf{S}_i \cdot \mathbf{S}_j}_{\mathcal{H}_{\text{exchange}}} + \underbrace{Dr^3 \sum_{i>j} \frac{\mathbf{S}_i \cdot \mathbf{S}_j - 3(\hat{\mathbf{r}}_{ij} \cdot \mathbf{S}_i)(\hat{\mathbf{r}}_{ij} \cdot \mathbf{S}_j)}{r_{ij}^3}}_{\mathcal{H}_{\text{dipolar}}}, \quad (6.5)$$

with the dipolar interaction constant  $D$  and,  $\mathbf{r}_{ij}$ , the displacement vector between the spins  $i$  and  $j$ . For ferromagnetic interaction,  $J$  and  $D$  have the same sign. Commonly, the dipolar term in Eq. (6.5) can be buried in the Ising exchange interaction,

$$\mathcal{H} = -J_{zz} \sum_{\langle i,j \rangle} \mathbf{S}_i^{(z)} \cdot \mathbf{S}_j^{(z)}, \quad (6.6)$$

with  $z$  labelling the local Ising axis. Now  $J_{zz}$  can be interpreted as some kind of effective coupling. Again  $J_{zz} < 0$  represents antiferromagnetic interaction (all-in/all-

out ordering) and  $J_{zz} > 0$  the ferromagnetic case (two-in/two-out ordering). A visualisation is plotted in Figure 6.4.

As written above,  $\text{Ho}_2\text{Ti}_2\text{O}_7$  is known to be the first experimentally verified spin ice. Here  $J_{zz}$  is positive. In examples with a long-range all-in/all-out ordering, such as  $\text{Sm}_2\text{Ti}_2\text{O}_7$  [224] or  $\text{Nd}_2\text{Zr}_2\text{O}_7$  [225],  $J_{zz}$  is negative. In the case of  $\text{Tb}_2\text{Ti}_2\text{O}_7$ , the classification is more difficult, as  $J_{zz}$  is relatively close to 0 (in comparison to  $\text{Ho}_2\text{Ti}_2\text{O}_7$ ).

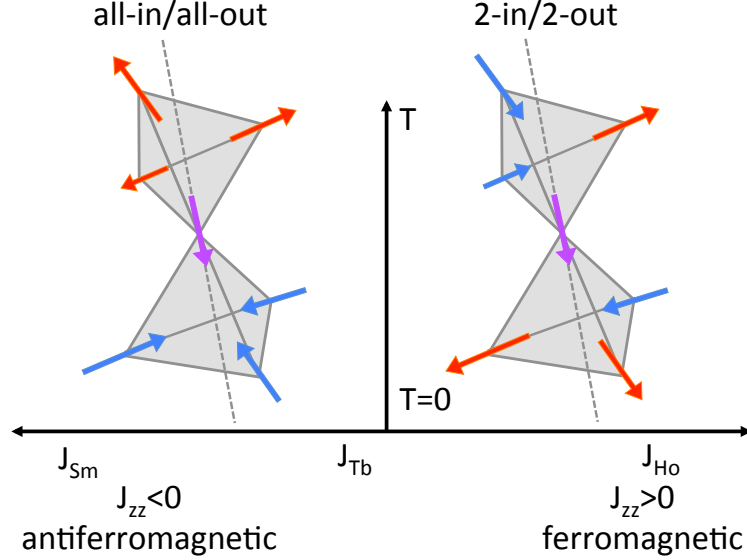


**Figure 6.4:** Magnetic arrangement at 0 K as a function of the effective exchange energy  $J_{zz}$ .

The most general nearest neighbour Hamiltonian in a pyrochlore lattice can be achieved by symmetry considerations [226]:

$$\begin{aligned} \mathcal{H} = - \sum_{\langle i,j \rangle} \{ & J_{zz} \mathbf{S}_i^{(z)} \mathbf{S}_j^{(z)} - J_{\pm} (\mathbf{S}_i^+ \mathbf{S}_j^- + \mathbf{S}_i^- \mathbf{S}_j^+) + J_{\pm\pm} (\gamma_{ij} \mathbf{S}_i^+ \mathbf{S}_j^+ + \gamma_{ij}^* \mathbf{S}_i^- \mathbf{S}_j^-) \\ & + J_{z\pm} [\mathbf{S}_i^z (\zeta_{ij} \mathbf{S}_j^+ + \zeta_{ij}^+ \mathbf{S}_j^-)] + i \leftrightarrow j \}. \end{aligned} \quad (6.7)$$

Again  $\mathbf{S}_i^{(z)}$  is the spin on the position  $i$  aligned to the local Ising axis  $z$ ,  $\mathbf{S}_i^+$  and  $\mathbf{S}_i^-$  represent transverse components of the spin moments perpendicular to the Ising axes. The properties  $\gamma_{ij}$  and  $\zeta_{ij}$  are matrices characterising the rotations between the local axes [226]. For the classical spin ice,

$$J_{zz} \gg J_{\pm}, J_{\pm\pm}, J_{z\pm}, \quad (6.8)$$

thus, we neglect those terms and arrive back at Eq. (6.6).

Neutron scattering techniques can also be used to characterise the type of magnetic ordering. In examples of long-range ordering, like  $\text{Sm}_2\text{Ti}_2\text{O}_7$ , the resulting diffraction

pattern shows clear magnetic Bragg peaks [224], see Figure 6.5(a). Measurements on  $Ho_2Ti_2O_7$  spin ice, on the other hand, result in scattering patterns with characteristic pinch points [227], see Figure 6.5(b). Pinch points represent a type of singularity in the scattering pattern of dipolar systems (a consequence of the spin-ice description) and are characteristic for these systems [228]. Neutron scattering experiments on  $Tb_2Ti_2O_7$  do indeed show pinch points. However, they also include butterfly-shaped patterns, such that the total diffraction pattern is not in agreement with a typical spin ice [229, 230], see Figure 6.5(c). The location of these butterfly-shaped patterns on the scattering map indicates a strong contribution of the transverse terms in the Hamiltonian. Thus, one must use the full Hamiltonian (Eq. (6.7)) and not the spin ice form of Eq. (6.5) to correctly understand this system. This is a hint that  $Tb_2Ti_2O_7$  is not a typical spin ice.

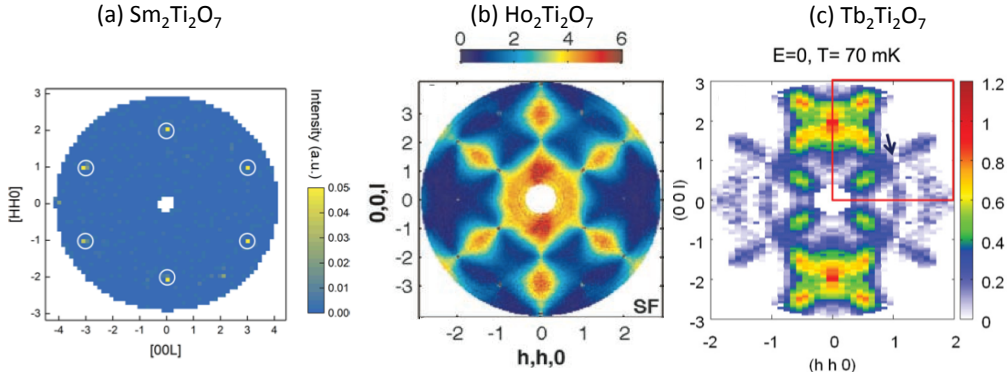


**Figure 6.5:** Comparison of neutron scattering patterns of (a)  $Sm_2Ti_2O_7$  (image taken from [224]), (b)  $Ho_2Ti_2O_7$  (image taken from [227]) and (c)  $Tb_2Ti_2O_7$  (image taken from [230]).

The system differs also in the energy of the first excited crystal electric field level (CEF). For spin-ice compounds including Ho or Dy energies of  $\sim 200 \text{ cm}^{-1}$  are reported [5]. This is a factor  $\sim 15$  larger than the CEF level of Tb which appears at  $\sim 12 \text{ cm}^{-1}$  [215, 231, 232]. Tb is a non-Kramers ion, thus the degeneracy of any doublet state is not protected by symmetry [222]. These non-Kramers doublets are susceptible to splitting from lattice distortions. The close lying states of a split doublet are susceptible for quantum fluctuations between them and mixing of the states, which could explain the exotic magnetism observed in  $Tb_2Ti_2O_7$ . However, in this case the symmetry of the ground state doublet in  $Tb_2Ti_2O_7$  is such that magnetic fluctuations (at the dipole limit) are forbidden. Therefore such mixing requires an addition of higher order multipole states which can be induced by the vibronic coupling to phonons and CEF levels.

The aim of this chapter is to probe the phonon spectra of  $Tb_2Ti_2O_7$  and compare them with the classical spin ice  $Ho_2Ti_2O_7$  and the Tb spin ice  $Tb_2Sn_2O_7$  to look for evidence of spin lattice coupling that could help to describe the peculiar magnetic ground state in this system.

## 6.2 Analysis

Single crystals of  $\text{Ho}_2\text{Ti}_2\text{O}_7$  (HTO) and  $\text{Tb}_2\text{Ti}_2\text{O}_7$  (TTO) were measured at low temperatures using the FTIR spectrometer. The spectra were obtained at 15 temperatures between 10 K and 300 K. In this setup, the data can be used in a range from  $\sim 40 \text{ cm}^{-1}$  up to  $\sim 680 \text{ cm}^{-1}$ . In pyrochlores, the lowest frequency phonon is typically at  $\sim 100 \text{ cm}^{-1}$ . Thus, the low frequency fit of the reflectance was performed with a linear approximation. The value at  $45 \text{ cm}^{-1}$  was taken and used as a constant to fill the missing values down to  $0 \text{ cm}^{-1}$ . The high frequency approximation is a room temperature scan in the MIR setting, which is used above  $680 \text{ cm}^{-1}$ . Here, a rather temperature-independent reflectance is expected in this spectral regime [233], thus the room temperature reflectance could be added without any scaling. A constant was used as an approximation above  $6000 \text{ cm}^{-1}$ . The spectra are saved up to  $15000 \text{ cm}^{-1}$ . The Kramers-Kronig analysis of the spectra was performed, such that the permittivity spectra are available from  $0 \text{ cm}^{-1}$  to  $3000 \text{ cm}^{-1}$ . The integration limit was chosen to be  $15000 \text{ cm}^{-1}$ . RefFIT software [121] was then used to fit the  $\varepsilon_2$  spectra.

The lowest frequency phonon can be difficult to fit due to a low intensity, as there is some background at high temperatures. At temperatures below  $\sim 150 \text{ K}$  the phonon becomes stronger and is thus more easy to fit. While the fit gives reasonable results for TTO samples, the lowest frequency phonon of HTO can not be fit above  $\sim 150 \text{ K}$ .

The polycrystalline  $\text{Tb}_2\text{Sn}_2\text{O}_7$  is studied in the same way. A compensation of the  $\text{Tb}_2\text{Sn}_2\text{O}_7$  reflectance is necessary to deal with the influence of polyethylene used in the pelletisation process. This process is described in Section 6.3.3.

A factor group analysis was performed using the Bilbao crystallographic server [124]. The calculation gives 7 infrared-active modes for the  $Fd-3m$  space group.

## 6.3 Results

### 6.3.1 $\text{Ho}_2\text{Ti}_2\text{O}_7$ (HTO)

Two single crystals of  $\text{Ho}_2\text{Ti}_2\text{O}_7$  were studied with  $k \parallel [111]$  and  $k \parallel [100]$ , respectively. The property  $k$  represents the wave vector of light travelling through the crystal. Thus,  $k$  is perpendicular to the illuminated sample surface. A low signal-to-noise ratio below  $\sim 70 \text{ cm}^{-1}$  makes the data unreliable, thus the lower cut-off frequency was set on this value for  $k \parallel [111]$ . The typical reflectance spectra of HTO are plotted in Figure 6.6. There is a trend towards higher reflectance for  $k \parallel [100]$ .

Figure 6.7 summarises the imaginary dielectric function,  $\varepsilon_2$ , for the same set of temperatures. In both crystals, the phonons are situated at similar frequencies. However, the phonons of the  $k \parallel [100]$  sample are much stronger and much narrower compared to the  $k \parallel [111]$  crystal. The clear and sharp phonons indicate the samples to be high quality single crystals. In general, the two spectra are comparable, although there are differences in the width of the peaks and a broadband background in the

$k \parallel [111]$   $\varepsilon_2$  results. These tributed to the uncertainties of the measurements and Kramers-Kronig analysis.

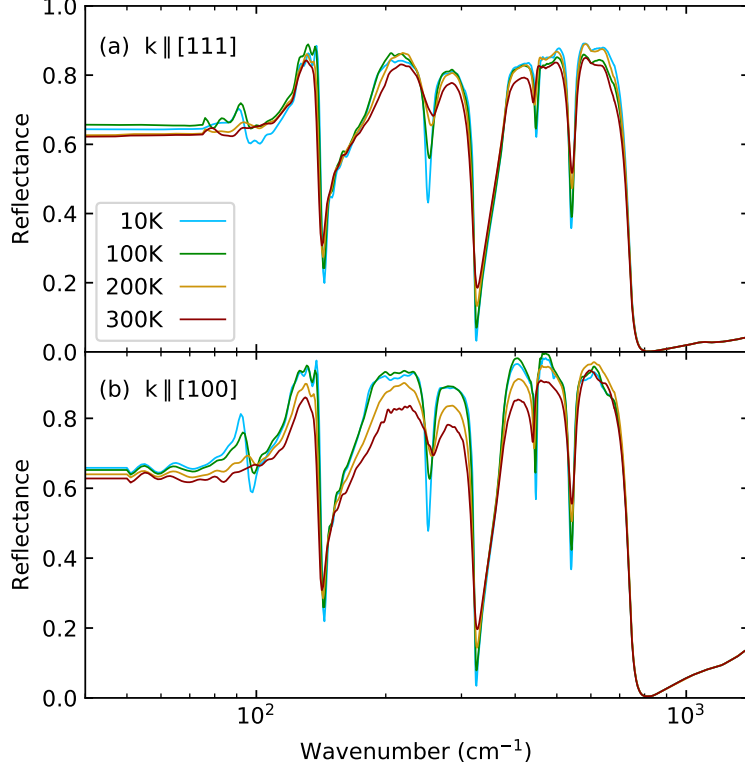


**Figure 6.6:** Reflectance of HTO pyrochlore plotted between  $40 \text{ cm}^{-1}$  and  $1400 \text{ cm}^{-1}$  as a function of temperature. The plots show the raw spectra obtained with the FTIR spectrometer for  $k \parallel [111]$  (a) and  $k \parallel [100]$  (b).

The spectra, plotted in Figure 6.7, were fit with RefFIT and the resonance frequencies of the model Lorentzian profiles summarised in Figure 6.8. Here one can see almost identical frequencies for all the modes. Noticeable discrepancies are observable only for the lowest mode. Here the  $k \parallel [100]$  frequency is systematically  $\sim 5 \text{ cm}^{-1}$  larger. In agreement with the group theoretical analysis, 7 modes can be observed in these pyrochlore samples. The fitted frequencies are summarised in Appendix A.3.

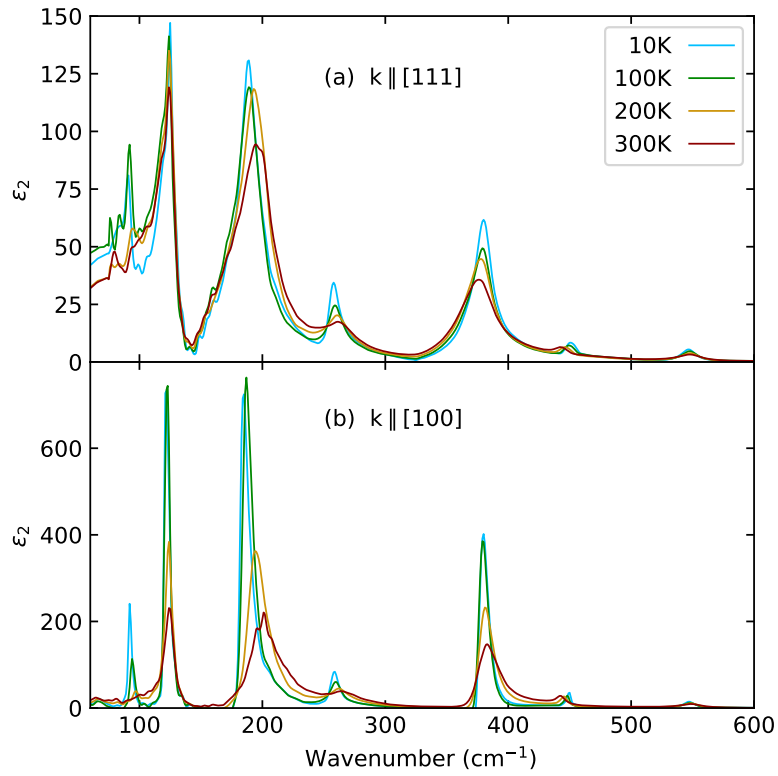


**Figure 6.7:** Imaginary part of the dielectric function of HTO pyrochlore plotted between  $40 \text{ cm}^{-1}$  and  $600 \text{ cm}^{-1}$  as a function of temperature. The plots show the raw spectra obtained with the FTIR spectrometer after KK analysis for  $k \parallel [111]$  (a) and  $k \parallel [100]$  (b).

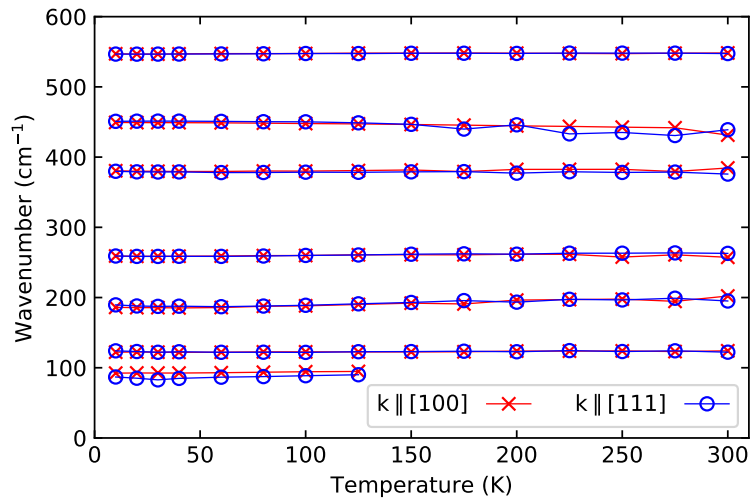
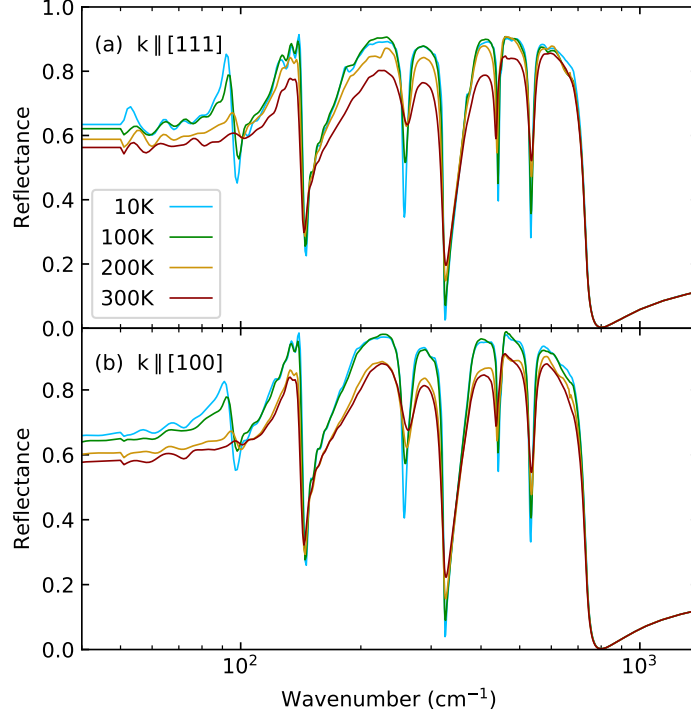


**Figure 6.8:** Frequencies of the 7 phonons in HTO plotted as a function of temperature. The figure compares the results of  $k \parallel [111]$  and  $k \parallel [100]$ .



### 6.3.2 $Tb_2Ti_2O_7$ (TTO)

The raw reflectance of TTO is plotted in Figure 6.9. Here, the shape of the spectra looks similar for both investigated samples ( $k \parallel [111]$  and  $k \parallel [100]$ ) of this material. In general, higher reflectance can be observed for the  $k \parallel [100]$  crystal. This is in agreement with the trends observed in HTO.



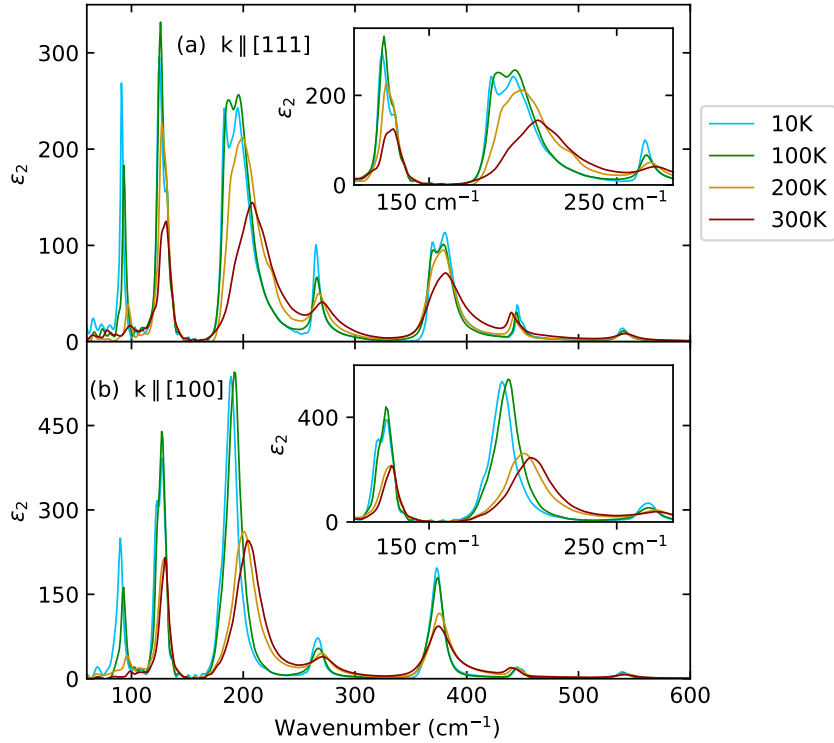
**Figure 6.9:** Reflectance of TTO pyrochlore plotted between  $40 \text{ cm}^{-1}$  and  $1400 \text{ cm}^{-1}$  as a function of temperature. The plots show the raw spectra obtained with the FTIR spectrometer for  $k \parallel [111]$  (a) and  $k \parallel [100]$  (b).

Figure 6.10 contains the imaginary part of the dielectric function. A rough view suggests a result similar to HTO. However, a closer look verifies that four modes are split for the  $k \parallel [111]$  example. Here, the strong modes at  $\sim 200 \text{ cm}^{-1}$  and  $\sim 380 \text{ cm}^{-1}$  are clearly split, while the splitting of the phonons at  $\sim 130 \text{ cm}^{-1}$  and  $\sim 450 \text{ cm}^{-1}$  is weaker. Nevertheless, zooming into these modes resolves a clear splitting. For  $k \parallel [100]$  the splitting can be observed only for the  $\sim 130 \text{ cm}^{-1}$  mode. The frequencies in both samples are in close agreement.

Spectra of  $\varepsilon_2$  have been fit at all temperatures as measured and the resulting frequencies are plotted in Figure 6.11(a). This figure shows that all modes keep constant in terms of frequency, and that when a  $k \parallel [111]$  mode is split, the  $k \parallel [100]$  mode sits exactly in between them. This plot further defines the split modes as P2, P3, P5 and P6. The non degenerate phonons are perfectly matching, as we saw already in the HTO case. Figure 6.11(b) gives one more view on the frequencies of the

$k\parallel[111]$  sample, highlighting the energy gap  $\Delta$ , being constant over the investigated temperature range. The P6 mode of  $k\parallel[111]$ , the one with the smallest  $\Delta$ , can be accurately fitted with two oscillators only below  $\sim 150$  K. Here, the peak in  $\varepsilon_2$  decreases such that a clear second phonon can not be verified. An identical behaviour can be seen for the P2 mode of  $k\parallel[100]$ .

In the  $k\parallel[100]$  orientation, the P3 mode has a weak shoulder below temperatures  $\sim 100$  K (see the inset of Figure 6.10(b)). At these temperatures fitting with two phonons gives reasonable results. In general this shoulder was not taken into account and the mode was fit with a single phonon only.



**Figure 6.10:** Imaginary part of the dielectric function of the TTO pyrochlore, plotted between  $40 \text{ cm}^{-1}$  and  $600 \text{ cm}^{-1}$  as a function of temperature. The plots show the raw spectra obtained with the FTIR spectrometer after the KK analysis for  $k\parallel[111]$  (a) and  $k\parallel[100]$  (b). The insets zoom into the area of the second and third phonon to highlight the splitting.

The splitting for  $k\parallel[111]$  is somehow symmetric, i.e. the gap of the outer two modes, P2 and P6 is  $\sim 5 \text{ cm}^{-1}$  and that of the inner two modes, P3 and P5, is  $\sim 12 \text{ cm}^{-1}$ , see Figure 6.11(b). Fascinatingly, this is in close agreement to the energy of the first CEF level and the splitting energy of the doublet states, see Section 6.1.3. Nevertheless there is no evidence for a connection of these properties. The average values of the splitting are summarised in Table 6.1. The splitting depends on the orientation of the crystal.

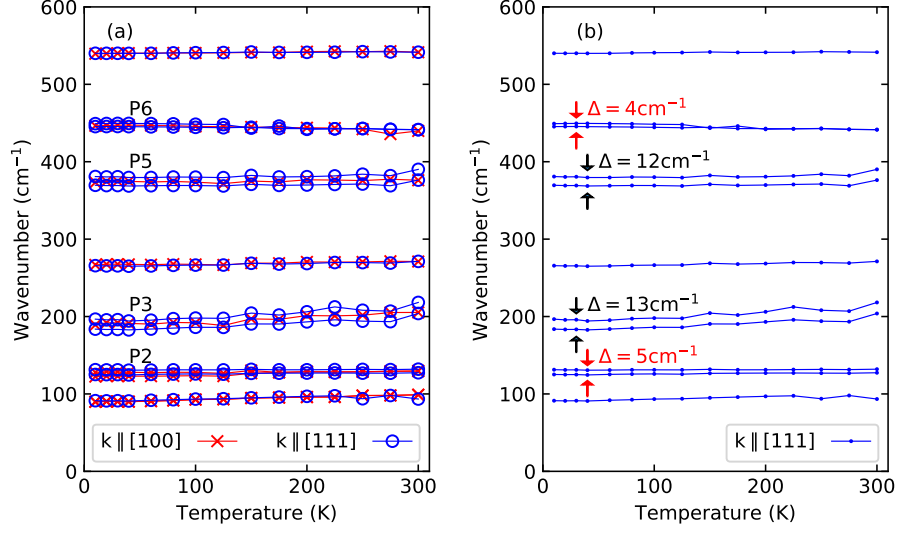


**Figure 6.11:** Fitted phonon frequencies of TTO pyrochlore plotted as a function of temperature. (a) The data of  $k||[111]$  and  $k||[100]$  is compared. The labels P2, P3, P5 and P6 highlight the modes split for  $k||[111]$ . (b) Energy splitting of the  $k||[111]$  modes.

peak	$k  [111]$	$k  [100]$
	$\Delta$ ( $\text{cm}^{-1}$ )	$\Delta$ ( $\text{cm}^{-1}$ )
P2	$5.3 \pm 0.7$	$4.4 \pm 0.7$
P3	$12.9 \pm 1.4$	$(7.0 \pm 1.4)$
P5	$11.5 \pm 1.0$	—
P6	$4.0 \pm 0.2$	—

**Table 6.1:** Frequency splitting  $\Delta$  of the TTO phonons in  $\text{cm}^{-1}$ . For TTO  $k||[100]$ , only the P2 phonon shows a clear splitting. For P3 the splitting was calculated by fitting the shoulder with a second phonon.

### 6.3.3 Tb<sub>2</sub>Sn<sub>2</sub>O<sub>7</sub> (TSO)

Finally, a powder pellet sample of Tb<sub>2</sub>Sn<sub>2</sub>O<sub>7</sub> is studied in the FTIR spectrometer. The goal was to check the influence of the Ti → Sn substitution. TSO is known to be a spin ice that orders in a certain way as described in reference [234]. The radius of a Sn ion is much larger than the one of a Ti ion. Thus, a comparison of the TSO and TTO data gives information about the influence of the *B*-site ion.

Unfortunately, single crystals of TSO are difficult to grow, so we were required to use a powder pellet. This sample was made by pressing powders into a pellet (with a diameter  $\sim 3.5$  mm). The TSO sample was produced by adding polyethylene (PE) in a 1:9 ratio of PE:TSO. A direction of polarisation is not given since this type of sample is polycrystalline.

The TSO reflectance corresponds with an abnormally shaped  $\varepsilon_2$  function. Most of the highly asymmetric peaks cannot be fit well with a Lorentzian profile. The reason is likely due to the PE added to the pellet. Therefore the reflectance of a pure PE pellet of same diameter was measured in additional. It shows a decreasing trend, as plotted in Figure 6.12(a). This curve was fitted with a function

$$f(x) = a_0 + A_0 \exp(\tau/x), \quad (6.9)$$

with temperature dependent fitting parameters  $a_0$ ,  $A_0$  and  $\tau$ . The raw reflectance was then divided by the fitting function. Finally, this reflectance has to be multiplied with a constant factor  $\sim 2.5$ , to compensate for these effects and produce physical results for  $\varepsilon_2$  without negative values. It is acknowledged that this procedure is not highly accurate, but the main aim of the pellet studies is to check the phonon modes against splitting, which is not affected by this procedure. The data of MIR and NIR room temperature measurements remain unchanged. The effects of PE are not considered in these spectral regions.

The adjusted reflectance is presented in Figure 6.12(b), the imaginary dielectric function is shown in Figure 6.12(c). These results show that the expected 7 modes are clearly visible. The peaks appear clean although a lot of data processing was necessary. There is clear evidence that TSO phonons do not show any splitting.

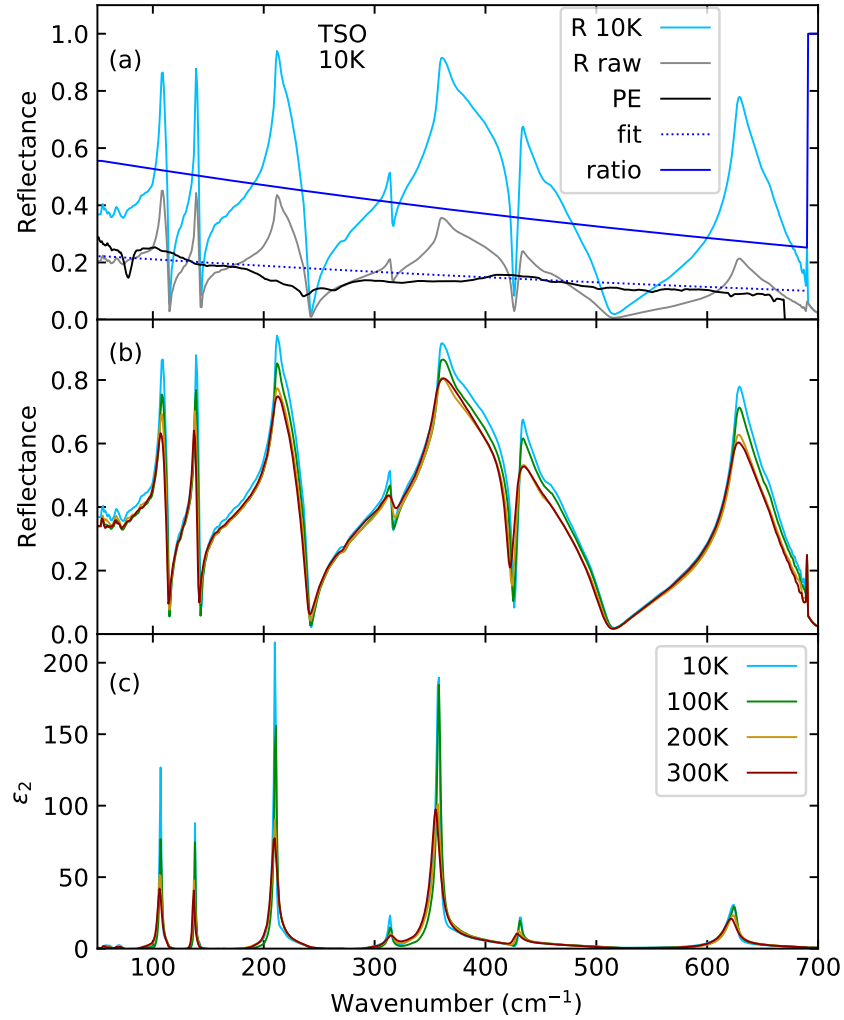


**Figure 6.12:** Spectra of TSO. (a) The reflectance of TSO at 10 K before ( $R$  raw) and after adjustment ( $R$  10K) including their ratio. The reflectance of polyethylene (PE) is plotted as well as the fit. The adjusted reflectance of four temperatures is plotted in (b), the corresponding  $\epsilon_2$  in (c).

## 6.4 Discussion and Summary

The main result is a unique clear splitting of phonons in TTO single crystals, that can not be seen in any other pyrochlore studied in my thesis. This splitting seems to be intrinsic as it is visible at high temperatures (even 300 K) far to high for spin lattice processes (spin coupling processes take place usually at temperatures of some tenth of kelvin). The energy gap  $\Delta$  of the splitting of these modes is in close agreement with the energy of the first CEF level and the splitting of the ground state (and the CEF level), respectively. Nevertheless there is no clear hint for a connection of these properties.

The splitting depends on the orientation of the single crystal. Thus, there is a relation to some structural anisotropy in the TTO lattice.

Since this splitting can nether be observed in HTO nor in TSO, a combination of the Tb and Ti sublattices is necessary for producing this effect. The Ti ions are much smaller than Sn ions. Thus, the Tb sublattice is more susceptible to displacement.

The conclusion is that TTO features likely intrinsic distortions that may be dynamic at time scales of some picoseconds. Thus, they can influence the spins through vibronic processes.

This system is highly sensitive to deviations from the perfect stoichiometry as samples of  $\text{Tb}_{2+x}\text{Ti}_{2-x}\text{O}_7$  [221], with  $x$  being the stuffing factor. For  $x > -0.0025$  an additional peak (at  $T \sim 0.5$  K) in measurements of the specific heat,  $C_P$ , highlights a signature of a second-order phase transition [221]. Thus, a long-range ordering (with unknown order parameter) can be seen in TTO, if this stuffing factor  $x$  is above a critical value  $x_c$ , otherwise a spin-liquid state can be seen [221]. In this thesis a  $k||[111]$  sample characterised with  $x \sim 0.003$  was investigated. Thus, in this sample, we expect the ground state to support long-range ordering. A second sample characterised with  $k||[100]$  was also studied. This crystal has a stuffing factor,  $x \sim -0.003$ , such that long-range ordering is not expected. However, follow up measurements have been performed with a  $k||[111]$  sample with a stuffing factor,  $x \sim -0.003$ . Even in this case splitting is observed. This verifies that the anisotropy of the TTO lattice plays an important role.

---

# 7

## Conclusions and Outlook

---

This chapter summarises the main achievements of my thesis and combines the most important results of the different materials. Ideas for future experiments to continue my studies are presented.

---

Magnetic frustration is a large topic covering a broad variety of materials. A lot of work is necessary to really understand the dynamic lattice environment that supports these frustrated spin states. In my thesis, I have only scratched the surface of this topic. Fascinatingly, we can learn about magnetic frustration without performing experiments under magnetic field.

In langasite  $\text{La}_3\text{Ga}_5\text{SiO}_{14}$  and rare-earth substituted compounds, low-frequency phonons were studied. The aim was to characterise the dynamics of an anomalous low-frequency phonon arising for  $E\parallel c$  polarised light. A softening of this mode can be observed with decreasing temperature. The same effect can be induced by replacing the  $\text{La}^{3+}$  ions with heavier ions. Here, the trend is linear with respect to the ion's atomic number. All these effects lead to the conclusion that the langasite lattice is close to a structural instability. For full softening of the anomalous low-frequency phonon, a transition from the P321 space group to the close laying polar P3 phase is expected.

Infrared investigations on langasites covered the spectra obtained at zero magnetic field. A first set of field dependent (up to 7 T) scans of HoLGS was performed using the THz spectrometer [85, 126]. Since these measurements provide information not only about the magnetic signatures of the low-frequency mode, but also about crystal electric field levels, a systematic study could be useful. Our samples are pretty thick for transmission measurements, thus we plan to do these scans for all four crystals in a reflectance time-domain spectrometer. Another idea is to perform one set of measurements (using the FTIR spectrometer and the cryostat) on a frustrated Fe-langasite. This could give information whether the low-frequency phonon is a global property of the langasite lattice or not. Time-domain measurements are actually performed on  $\text{Nd}_3\text{Ga}_5\text{SiO}_{14}$  to check this material for magnetic modes, predicted by our coworkers from General Physics Institute Moscow.

The multiferroic francisite,  $\text{Cu}_3\text{Bi}(\text{SeO}_3)_2\text{O}_2\text{Cl}$ , has a kagome lattice similar to the langasites. Again, the dynamics of a soft mode was the main goal of the investigations. Here, we observe the softening of a phonon reaching its minimum in frequency at  $T_S = 115\text{ K}$ , the critical temperature of a structural phase transition. While recent publications highlight this mode driving a fully displacive antiferroelectric transition, my work using infrared spectroscopy gives information on a close lying ferroelectric phase. The dynamics of this mode in both phases gives information about a possible sublattice polarisation. This is a signature of an antiferroelectric state.

In francisite, we observed a weak excitation ( $\bar{\nu} \sim 10\text{ cm}^{-1}$ ), only visible at 10 K. Probably this mode is magnetic, thus experiments could be planned using the THz spectrometer and the magnet to study its behaviour in more details. A second aim is to establish the theoretical model describing my results.

Further on, the studies on pyrochlores deal with the observations of splitting of phonons in  $\text{Tb}_2\text{Ti}_2\text{O}_7$  (TTO) pyrochlore (despite the other investigated groups of materials only a weak softening of some mode is seen here). This splitting can not be observed for other materials of the pyrochlore family, such as  $\text{Ho}_2\text{Ti}_2\text{O}_7$  and  $\text{Tb}_2\text{Sn}_2\text{O}_7$ . TTO features intrinsic distortions that contribute to the vibronic coupling and to quantum fluctuations that drive the spin-liquid behaviour. Future ideas on



$\text{Tb}_2\text{Ti}_2\text{O}_7$  focus on the influence of the Tb/Ti ratio. The investigated sample of  $\text{Tb}_{2+x}\text{Ti}_{2-x}\text{O}_7$  has a stuffing value,  $x$ , in the range where a spin liquid state is not expected according to reference [221]. A second crystal with  $x \sim -0.003$ , supporting a spin-liquid state, is currently investigated. Here, the aim is to study and compare the splitting of the TTO  $k_{\parallel}[111]$  crystals. Further samples with  $x = 0.01$  and  $x = -0.01$ , are available for further projects.

Finally, my thesis presents new details of the lattice dynamics of the three investigated magnetically frustrated materials. My work highlights several individual mechanisms driving the lattice dynamics.



---

# A

## Supplementary data

---

This Appendix shows supplementary data of the investigated materials.

### Contents

---

<b>A.1</b>	<b>Langasites</b>	<b>106</b>
A.1.1	Phonon data	106
A.1.2	Spectra	107
<b>A.2</b>	<b>Francisite</b>	<b>112</b>
A.2.1	Phonon data	112
A.2.2	Spectra	113
<b>A.3</b>	<b>Pyrochlores</b>	<b>116</b>

---

## A.1 Langasites

Various compounds of the langasite family were studied in the frame of this thesis and the results were presented in Chapter 4. In this Appendix, additionally the list of phonon frequencies at room temperature will be shown. Further, the reflectance and the dielectric function of all investigated a-cut crystals are shown as a function of the sample's temperature. This is done for both polarisations and four temperatures (10 K, 100 K, 200 K, 300 K).

### A.1.1 Phonon data

The following tables summarise the fitting parameters (frequency  $\bar{\nu}_0$  and dielectric contribution  $\Delta\varepsilon$ ) of the langasite models, obtained with the RefFIT software. Additionally the value of the high frequency permittivity,  $\varepsilon_\infty$ , is given. The data is given for room temperature measurements.

	LGS		HoLGS		NGS		PGS	
	$\varepsilon_\infty = 3.66$		$\varepsilon_\infty = 3.5$		$\varepsilon_\infty = 3.6$		$\varepsilon_\infty = 3.77$	
	$\bar{\nu}_0$ (cm <sup>-1</sup> )	$\Delta\varepsilon$	$\bar{\nu}_0$ (cm <sup>-1</sup> )	$\Delta\varepsilon$	$\bar{\nu}_0$ (cm <sup>-1</sup> )	$\Delta\varepsilon$	$\bar{\nu}_0$ (cm <sup>-1</sup> )	$\Delta\varepsilon$
1	44.94	47.76	41.57	51.60	38.39	63.06	40.56	60.72
2	85.96	2.74	88.88	1.32	92.21	2.36	89.91	2.76
3					136.02	0.03	139.18	0.01
4	162.99	0.79	163.08	0.65	161.40	0.90	162.01	0.98
5	210.86	0.34	211.31	0.25	213.73	0.18	213.17	0.29
6	243.60	0.18	241.95	0.12	258.68	0.18	250.43	0.19
7	287.60	0.69	288.74	0.43	296.49	0.54	293.61	0.68
8	308.05	0.58	310.84	0.55	315.00	0.62	313.3	0.62
9	478.00	0.03	479.24	0.01	478.61	0.13	483.16	0.01
10	511.85	0.89	516.66	0.68	520.47	0.98	521.16	1.02
11	577.71	0.10	578.99	0.08	582.94	0.06	581.89	0.11
12	648.46	0.52	652.61	0.38	648.93	0.53	648.70	0.58
13	672.48	0.18	677.34	0.27	682.70	0.13	677.02	0.15
14	733.49	0.01	734.88	0.01	737.09	0.01	735.16	0.01
15	861.92	0.01	861.73	0.01	856.35	0.02	862.24	0.02
16	947.03	0.09	949.77	0.07	942.12	0.11	947.80	0.11
17	966.33	0.05	968.89	0.05	969.08	0.03	967.00	0.05

**Table A.1:** Oscillator data of the four langasites at room temperature and E||c. Phonon 1 represents the low frequency structure, which consists out of two phonons at lower temperatures. The fit was performed with one oscillator only.

	LGS		HoLGS		NGS		PGS	
	$\varepsilon_\infty = 3.7$		$\varepsilon_\infty = 3.56$		$\varepsilon_\infty = 3.58$		$\varepsilon_\infty = 3.95$	
	$\bar{\nu}_0$ (cm <sup>-1</sup> )	$\Delta\varepsilon$	$\bar{\nu}_0$ (cm <sup>-1</sup> )	$\Delta\varepsilon$	$\bar{\nu}_0$ (cm <sup>-1</sup> )	$\Delta\varepsilon$	$\bar{\nu}_0$ (cm <sup>-1</sup> )	$\Delta\varepsilon$
1	88.71	6.25	82.51	8.18	87.76	3.56	82.63	5.19
2	103.21	2.94	102.49	2.20	101.84	3.71	102.72	4.31
3	112.86	0.21	112.72	0.08				
4	129.78	1.33	129.73	0.98	128.81	1.16	129.43	1.12
5	150.41	2.07	150.52	1.60	151.83	2.35	150.56	2.56
6	193.86	1.18	194.03	0.88	194.01	1.33	193.54	1.41
7	214.40	0.50	214.76	0.41	215.27	0.24	214.64	0.29
8	241.77	0.55	239.98	0.25	239.97	0.74	238.14	0.65
9	257.22	1.16	258.38	1.02	259.37	1.26	259.45	1.49
10	284.09	0.82	285.49	0.72	284.38	0.39	282.96	0.58
11	316.98	0.06	317.68	0.05	318.19	0.23	317.84	0.12
12	341.15	0.58	343.29	0.49	347.47	0.47	343.73	0.65
13	374.16	0.49	375.88	0.45	377.85	0.40	376.32	0.51
14	425.41	0.29	427.40	0.25	431.32	0.30	429.98	0.37
15	448.48	0.23	450.45	0.22	455.79	0.23	453.93	0.24
16	487.19	0.10	489.37	0.13	499.62	0.11	496.60	0.12
17	508.01	0.06	511.80	0.04	517.42	0.04	514.11	0.06
18	631.07	0.31	634.72	0.27	629.81	0.32	633.11	0.31
19	682.60	0.14	683.81	0.12	684.20	0.12	682.71	0.17
20	733.46	0.05	734.85	0.05	737.78	0.05	737.18	0.06
21	883.65	0.05	884.02	0.03	878.88	0.07	882.24	0.04
22	905.09	0.11	908.14	0.11	904.53	0.08	904.51	0.14

**Table A.2:** Oscillator data of the four langasites at room temperature and E||b\*.

### A.1.2 Spectra

The following spectra show the reflectance and dielectric function of each of the four investigated langasites. Data of both investigated polarisations is presented and shown for four temperatures. Reflectance and  $\varepsilon_2$  is plotted in the range between 0 cm<sup>-1</sup> and 600 cm<sup>-1</sup>,  $\varepsilon_1$  only between 0 cm<sup>-1</sup> and 300 cm<sup>-1</sup>.

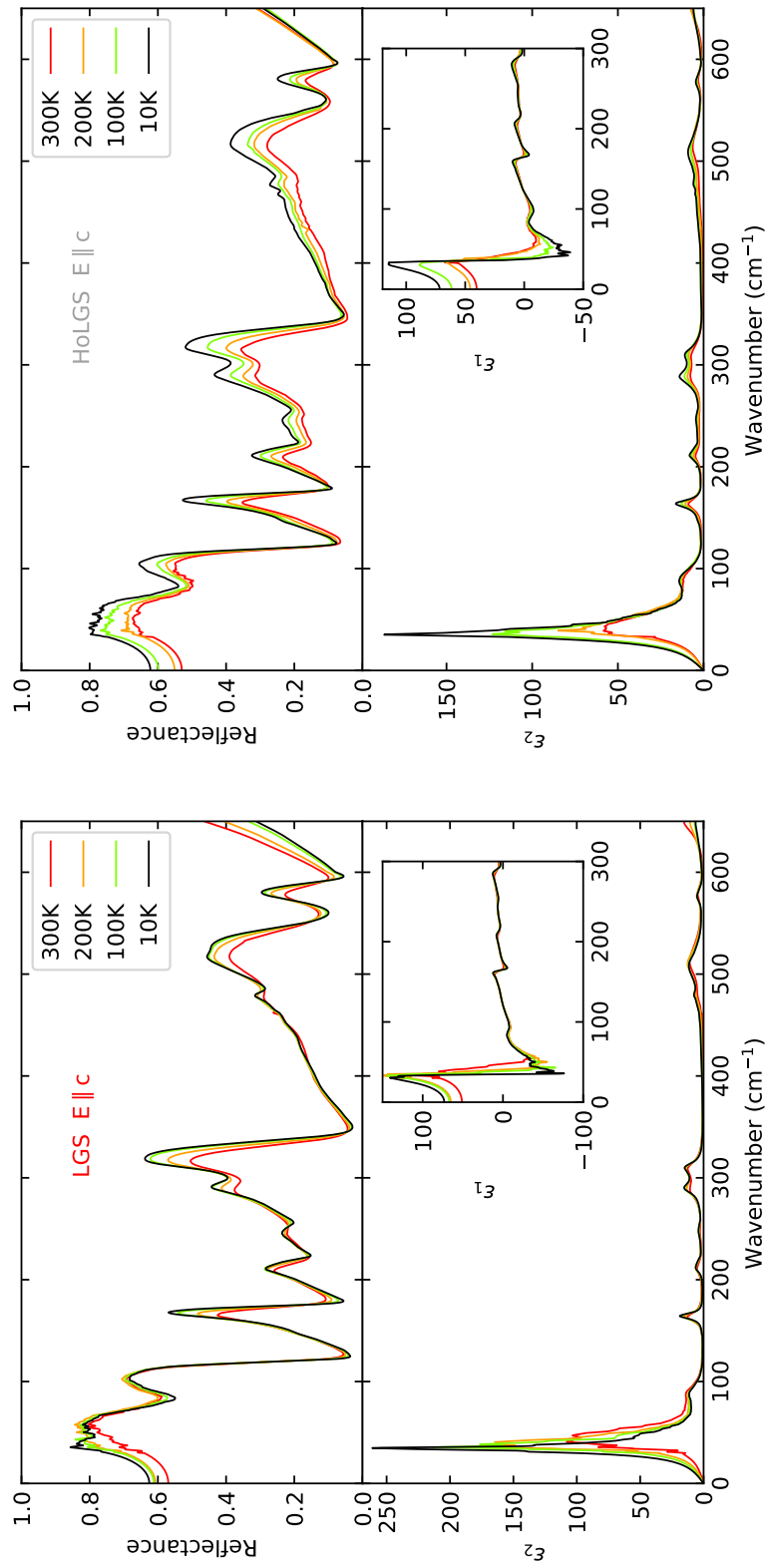


**Figure A.1:** Data of LGS (left) and HoLGS (right) for  $E \parallel c$  polarisation.

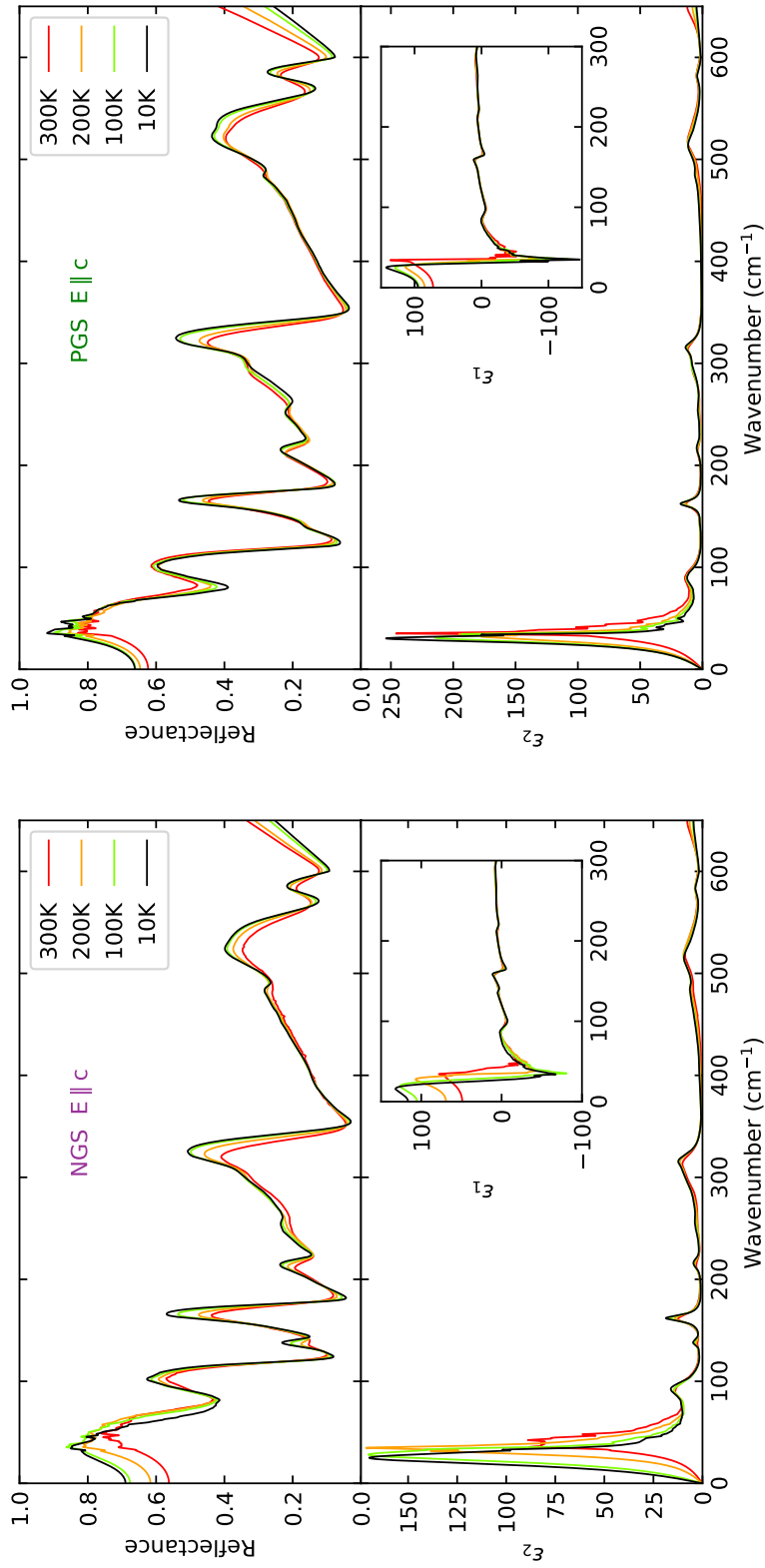


**Figure A.2:** Data of NGS (left) and PGS (right) for  $E||c$  polarisation.

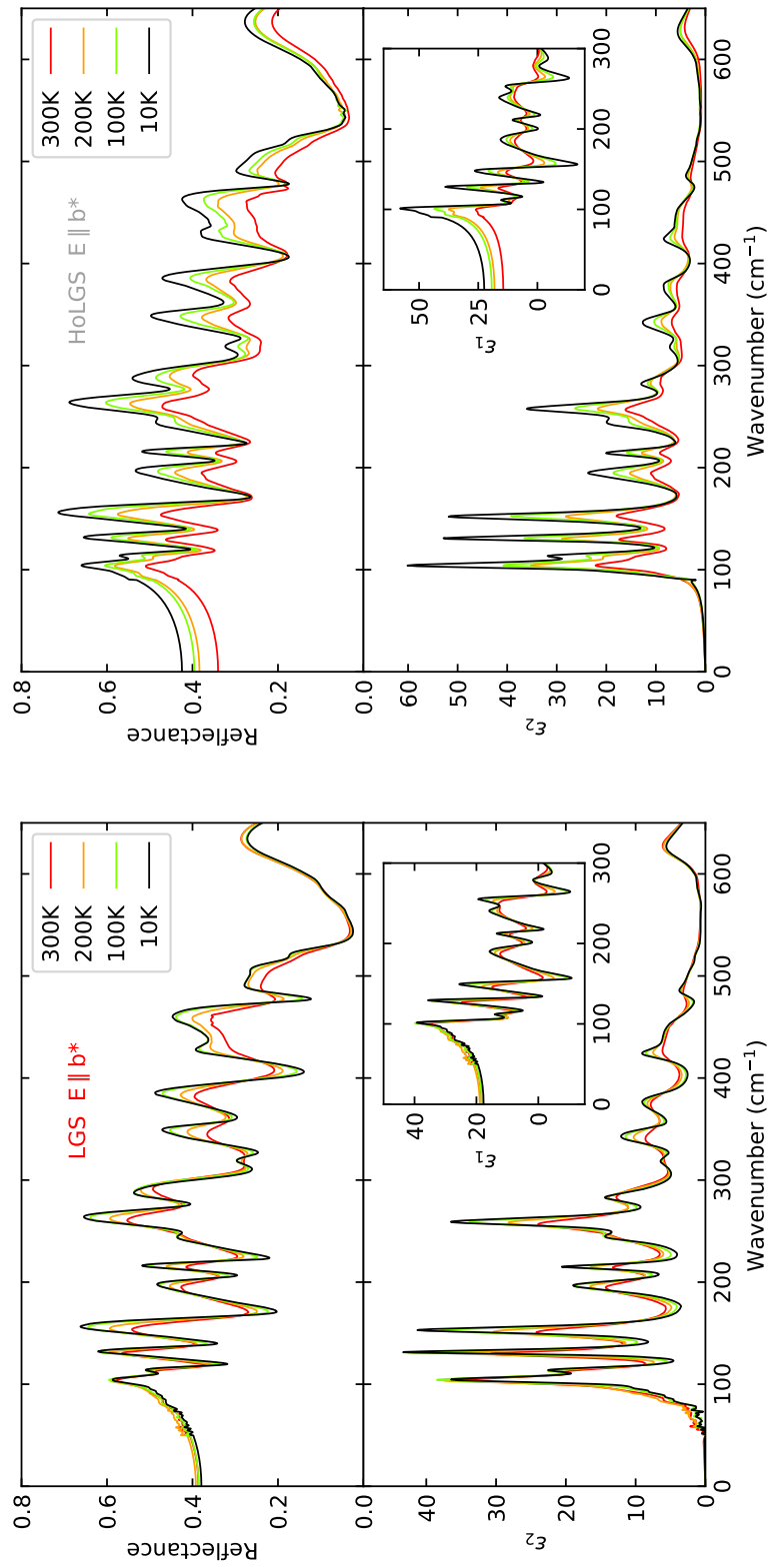


**Figure A.3:** Data of LGS (left) and HoLGS (right) for  $E||b^*$  polarisation.



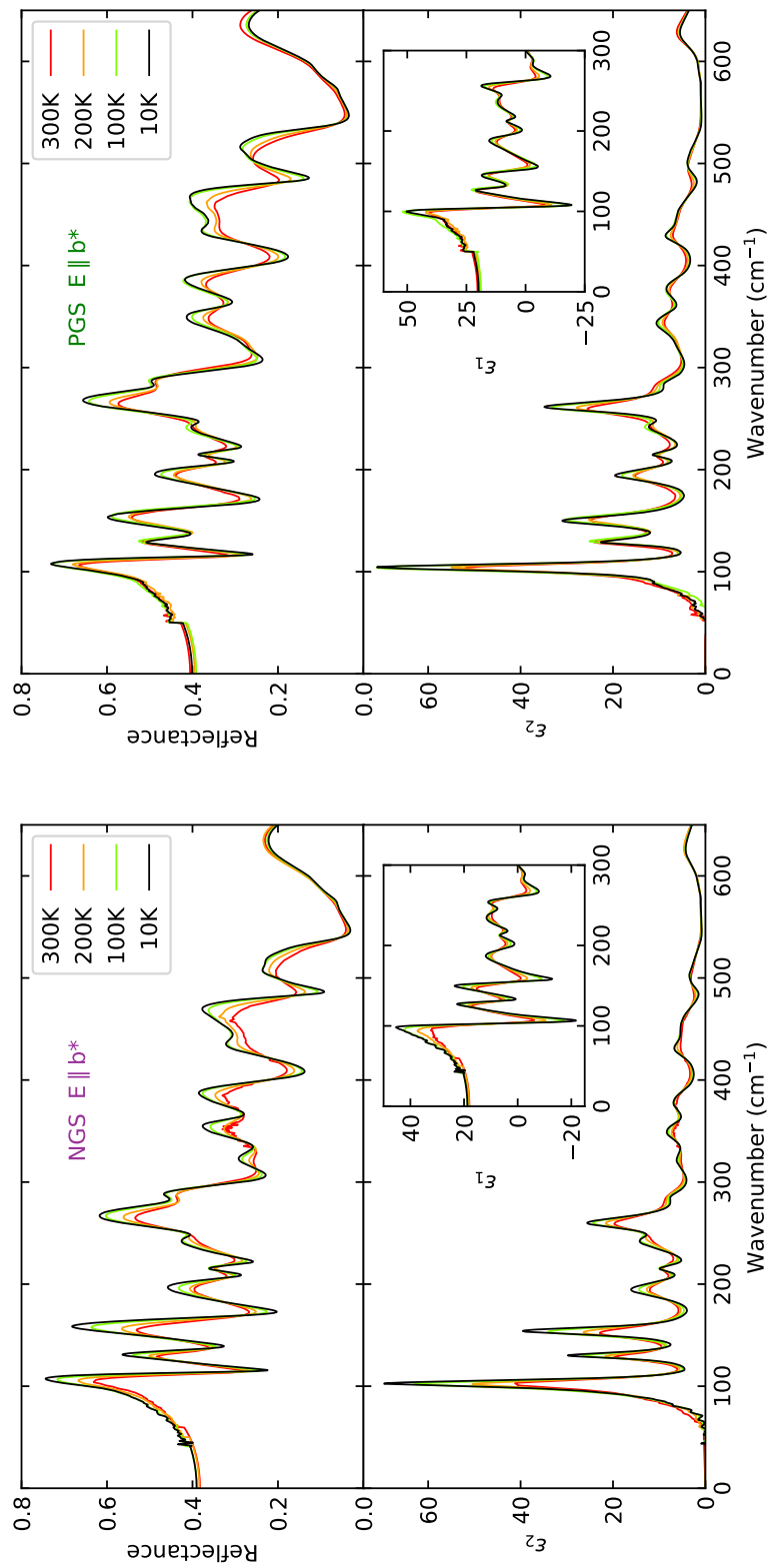


**Figure A.4:** Data of NGS (left) and PGS (right) for  $E||b^*$  polarisation.

## A.2 Francisite

The section covers additional information about francisite (CBSCl), as presented in Chapter 5.

### A.2.1 Phonon data

The following tables summarise the resonance frequency and dielectric contribution of the individual Lorentzian oscillators, obtained with the fit. The data is presented for three temperatures (10 K, 115 K= $T_S$ , 300 K) and both polarisations.

	10 K		115 K		300 K	
	$\varepsilon_\infty = 4.22$		$\varepsilon_\infty = 4.09$		$\varepsilon_\infty = 4.17$	
	$\bar{\nu}_0$ (cm <sup>-1</sup> )	$\Delta\varepsilon$	$\bar{\nu}_0$ (cm <sup>-1</sup> )	$\Delta\varepsilon$	$\bar{\nu}_0$ (cm <sup>-1</sup> )	$\Delta\varepsilon$
1	52.93	3.00	31.80	18.77	41.29	10.54
2	69.36	1.13				
3	88.63	2.42	87.97	1.82	86.33	2.18
4	94.29	0.90	93.13	0.73	90.64	0.83
5	162.72	0.27	162.57	0.22	162.02	0.28
6	172.72	0.13				
7	194.01	1.16	192.80	1.10	189.94	1.21
8	202.47	0.34	201.88	0.38	198.96	0.32
9	320.80	0.07	327.10	0.07	323.25	0.08
10	331.98	0.03				
11	423.08	0.05	421.07	0.03	418.12	0.01
12	543.34	0.09	546.95	0.01		
13	559.19	0.33	554.16	0.39	544.87	0.41
14	686.00	0.48	685.21	0.48	684.55	0.52

**Table A.3:** Oscillator data of CBSCl for E||a polarisation. Last fit including phonon 2 performed at 100 K, phonons 6 and 10 at 115 K and phonon 12 at 120 K.

	10 K		115 K		300 K	
	$\varepsilon_\infty = 3.78$		$\varepsilon_\infty = 3.46$		$\varepsilon_\infty = 3.61$	
	$\bar{\nu}_0$ (cm <sup>-1</sup> )	$\Delta\varepsilon$	$\bar{\nu}_0$ (cm <sup>-1</sup> )	$\Delta\varepsilon$	$\bar{\nu}_0$ (cm <sup>-1</sup> )	$\Delta\varepsilon$
1	37.81	15.92	40.27	12.38	51.70	5.05
2	68.02	1.71	68.66	1.60	68.19	2.96
3	98.08	0.10				
4	113.97	1.51	114.28	1.35	112.33	1.53
5	128.87	0.06				
6	133.35	0.11	133.72	0.11	131.97	0.09
7	185.69	0.51	185.33	0.46	182.90	0.48
8	257.31	0.20	258.19	0.21	255.78	0.23
9	276.45	0.08	274.94	0.01		
10	300.79	0.05	300.08	0.05	297.74	0.07
11	314.67	0.02	314.41	0.01	310.62	0.01
12	457.64	0.31	456.77	0.33	452.08	0.36
13	486.25	0.11	487.86	0.01		
14	508.90	0.35	504.64	0.36	496.31	0.38
15	542.71	0.06	542.49	0.06	539.77	0.05
16	572.88	0.04	568.75	0.03	559.18	0.03
17	715.15	0.53	712.06	0.52	712.48	0.50
18	809.42	0.01	810.75	0.01	804.83	0.00
19	825.43	0.04	824.05	0.03	822.02	0.05

**Table A.4:** Oscillator data of CBSCl for E||b polarisation. Last fit including phonons 3 and 5 performed at 100 K and phonons 9 and 13 at 115 K. Phonon 18 becomes almost invisible at temperatures larger than 115 K, but there is no clear cut.

## A.2.2 Spectra

Here, the raw FTIR data is compared with the fits. Further, broadband spectra are plotted up to 900 cm<sup>-1</sup>.

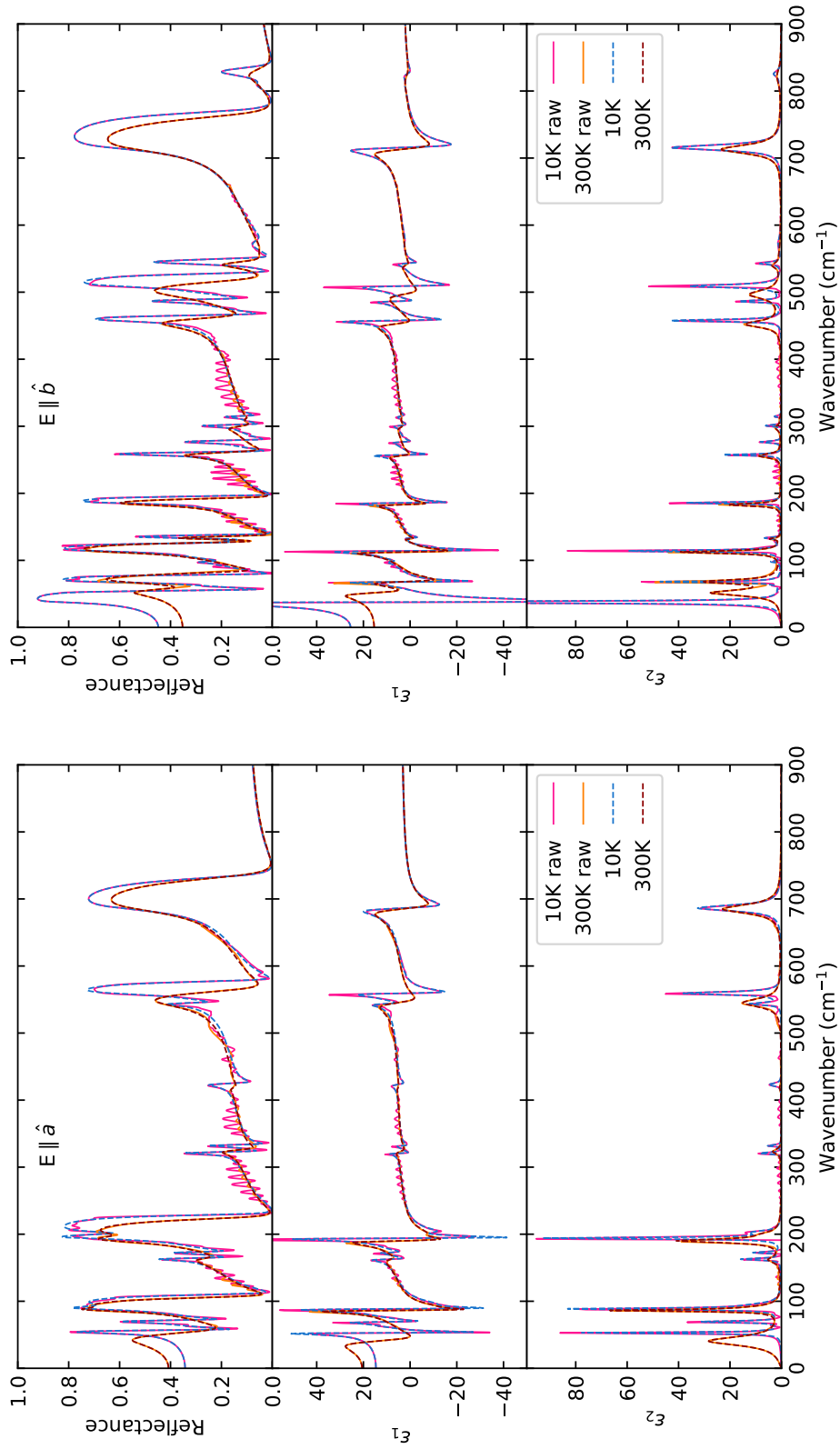


**Figure A.5:** The raw reflectance and the dielectric function (solid lines) are compared with data obtained by fitting (dashed lines). Left for the  $E \parallel \hat{a}$  case, right for  $E \parallel \hat{b}$ . Data is shown for 10 K and 300 K.

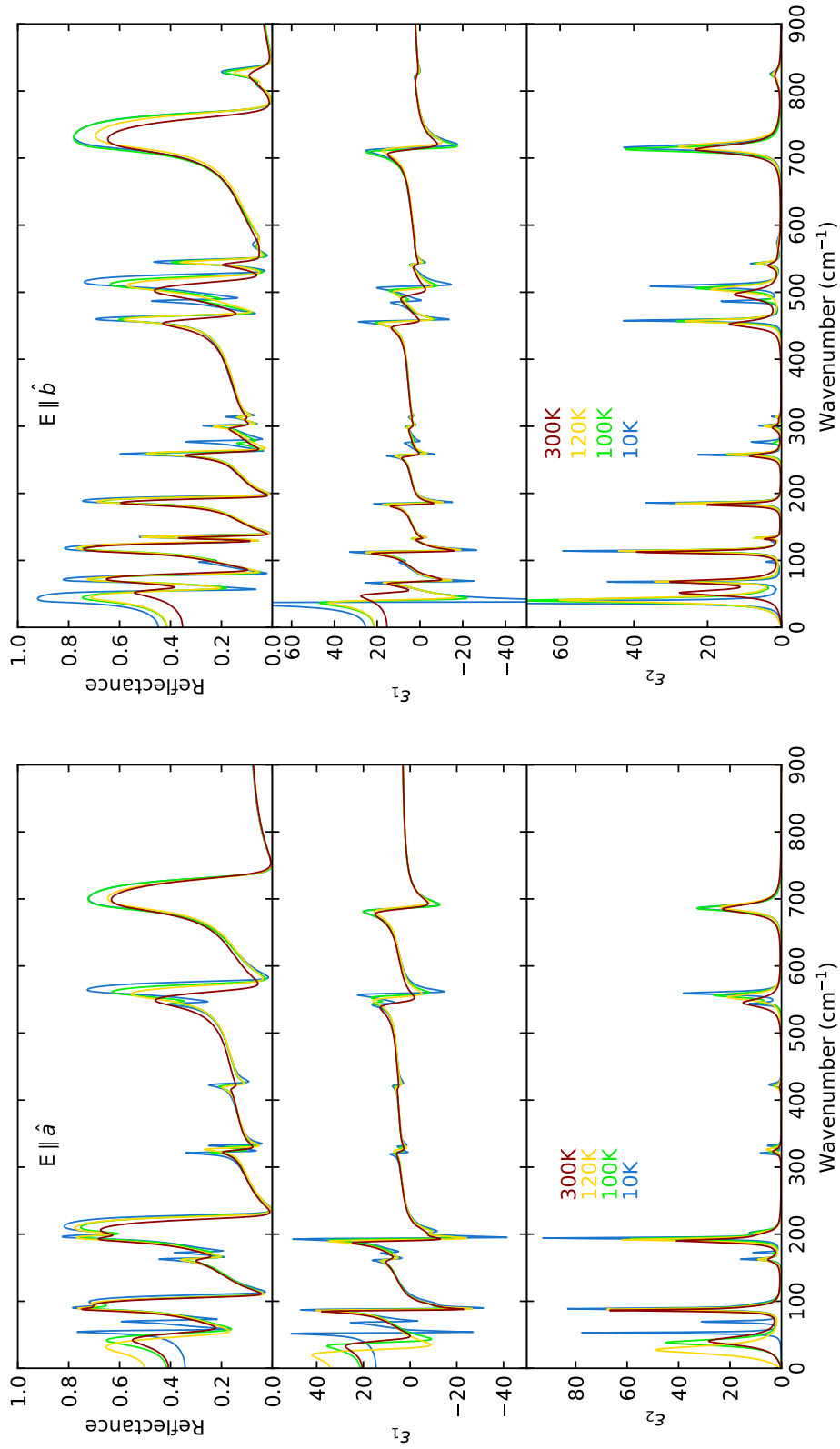


**Figure A.6:** Reflectance spectra and dielectric function (fit) of four temperatures plotted between  $0 \text{ cm}^{-1}$  and  $900 \text{ cm}^{-1}$ . Left for the  $E \parallel \hat{a}$  case, right for  $E \parallel \hat{b}$  (here the first excitation is not completely shown for  $\epsilon_2$ , details see Figure 5.3(f)).

## A.3 Pyrochlores

The section covers additional information about the pyrochlore samples, as presented in Chapter 6. The following tables summarise the resonance frequency of the individual Lorentzian oscillators, obtained with the fit.

	TTO $k  [100]$		TTO $k  [111]$	
	10 K	300 K	10 K	300 K
	$\bar{\nu}_0$ (cm <sup>-1</sup> )	$\bar{\nu}_0$ (cm <sup>-1</sup> )	$\bar{\nu}_0$ (cm <sup>-1</sup> )	$\bar{\nu}_0$ (cm <sup>-1</sup> )
1	89.85	99.12	91.27	93.42
2	122.37	126.84	125.14	127.36
2'	127.82	130.75	131.31	131.98
3	190.38	205.29	183.72	203.91
3'			196.62	218.19
4	266.72	271.09	265.71	271.25
5	373.16	376.06	369.56	376.27
5'			380.84	390.12
6	449.91	439.76	445.37	441.43
6'			449.19	
7	539.49	541.43	540.08	541.48

**Table A.5:** Phonon frequencies of TTO.

	HTO $k  [100]$		HTO $k  [111]$		TSO	
	10 K	300 K	10 K	300 K	10 K	300 K
	$\bar{\nu}_0$ (cm <sup>-1</sup> )	$\bar{\nu}_0$ (cm <sup>-1</sup> )	$\bar{\nu}_0$ (cm <sup>-1</sup> )	$\bar{\nu}_0$ (cm <sup>-1</sup> )	$\bar{\nu}_0$ (cm <sup>-1</sup> )	$\bar{\nu}_0$ (cm <sup>-1</sup> )
1	92.34	73.32	86.85	92.05	106.82	106.15
2	122.20	124.13	124.08	122.17	138.11	136.76
3	186.01	202.17	189.54	195.09	210.05	209.66
4	259.16	257.32	259.13	262.89	313.59	314.85
5	380.54	384.52	379.80	375.82	356.98	355.09
6	449.35	431.35	450.94	438.95	431.84	429.25
7	547.09	548.29	546.70	547.45	621.99	621.07

**Table A.6:** Phonon frequencies of HTO and TSO.

---

# Bibliography

---

- [1] C. Lacroix, P. Mendels, and F. Mila. *Introduction to Frustrated Magnetism: Materials, Experiments, Theory*, vol. 164. Springer Science & Business Media (2011).
- [2] J. T. Chalker, P. C. W. Holdsworth, and E. F. Shender. *Hidden order in a frustrated system: Properties of the Heisenberg kagome antiferromagnet*. Physical Review Letters **68**, 855 (1992).
- [3] D. A. Huse and A. D. Rutenberg. *Classical antiferromagnets on the kagome lattice*. Physical Review B **45**, 7536 (1992).
- [4] K. Binder and A. P. Young. *Spin glasses: Experimental facts, theoretical concepts, and open questions*. Reviews of Modern Physics **58**, 801 (1986).
- [5] S. T. Bramwell and M. J. P. Gingras. *Spin ice state in frustrated magnetic pyrochlore materials*. Science **294**, 1495 (2001).
- [6] L. Balents. *Spin liquids in frustrated magnets*. Nature **464**, 199 (2010).
- [7] A. P. Ramirez. *Strongly geometrically frustrated magnets*. Annual Review of Materials Science **24**, 453 (1994).
- [8] G. H. Wannier. *Antiferromagnetism. The triangular Ising net*. Physical Review **79**, 357 (1950).
- [9] M. Kenzelmann, G. Lawes, A. B. Harris, G. Gasparovic, C. Broholm, A. P. Ramirez, G. A. Jorge, M. Jaime, S. Park, Q. Huang, A. Y. Shapiro, and L. A. Demianets. *Direct transition from a disordered to a multiferroic phase on a triangular lattice*. Physical Review Letters **98**, 267205 (2007).
- [10] K. Marty, V. Simonet, E. Ressouche, R. Ballou, P. Lejay, and P. Bordet. *Single domain magnetic helicity and triangular chirality in structurally enantiopure  $Ba_3NbFe_3Si_2O_{14}$* . Physical Review Letters **101**, 247201 (2008).
- [11] A. Mulder, R. Ganesh, L. Capriotti, and A. Paramekanti. *Spiral order by disorder and lattice nematic order in a frustrated Heisenberg antiferromagnet on the honeycomb lattice*. Physical Review B **81**, 214419 (2010).
- [12] R. Ganesh, J. van den Brink, and S. Nishimoto. *Deconfined criticality in the frustrated Heisenberg honeycomb antiferromagnet*. Physical Review Letters **110**, 127203 (2013).
- [13] Y. Kubota, H. Tanaka, T. Ono, Y. Narumi, and K. Kindo. *Successive magnetic phase transitions in  $\alpha$ - $RuCl_3$ : XY-like frustrated magnet on the honeycomb lattice*. Physical Review B **91**, 094422 (2015).

- [14] S. Nishimoto, V. M. Katukuri, V. Yushankhai, H. Stoll, U. K. Rößler, L. Hozoi, I. Rousochatzakis, and J. Van Den Brink. *Strongly frustrated triangular spin lattice emerging from triplet dimer formation in honeycomb  $Li_2IrO_3$* . Nature Communications **7**, 1 (2016).
- [15] Y. J. Uemura, A. Keren, K. Kojima, L. P. Le, G. M. Luke, W. D. Wu, Y. Ajiro, T. Asano, Y. Kuriyama, M. Mekata, H. Kikuchi, and K. Kakurai. *Spin fluctuations in frustrated kagome lattice system  $SrCr_8Ga_4O_{19}$  studied by muon spin relaxation*. Physical Review Letters **73**, 3306 (1994).
- [16] G. Evenbly and G. Vidal. *Frustrated antiferromagnets with entanglement renormalization: Ground state of the spin-1/2 Heisenberg model on a kagome lattice*. Physical Review Letters **104**, 187203 (2010).
- [17] G.-B. Jo, J. Guzman, C. K. Thomas, P. Hosur, A. Vishwanath, and D. M. Stamper-Kurn. *Ultracold atoms in a tunable optical kagome lattice*. Physical Review Letters **108**, 045305 (2012).
- [18] S. Nishimoto, N. Shibata, and C. Hotta. *Controlling frustrated liquids and solids with an applied field in a kagome Heisenberg antiferromagnet*. Nature Communications **4**, 1 (2013).
- [19] P. Bordet, I. Gelard, K. Marty, A. Ibanez, J. Robert, V. Simonet, B. Canals, R. Ballou, and P. Lejay. *Magnetic frustration on a kagome lattice in  $R_3Ga_5SiO_{14}$  langasites with  $R = Nd, Pr$* . Journal of Physics: Condensed Matter **18**, 5147 (2006).
- [20] B. D. Gaulin, J. N. Reimers, T. E. Mason, J. E. Greedan, and Z. Tun. *Spin freezing in the geometrically frustrated pyrochlore antiferromagnet  $Tb_2Mo_2O_7$* . Physical Review Letters **69**, 3244 (1992).
- [21] M. J. P. Gingras, C. V. Stager, N. P. Raju, B. D. Gaulin, and J. E. Greedan. *Static critical behavior of the spin-freezing transition in the geometrically frustrated pyrochlore antiferromagnet  $Y_2Mo_2O_7$* . Physical Review Letters **78**, 947 (1997).
- [22] J. S. Gardner, S. R. Dunsiger, B. D. Gaulin, M. J. P. Gingras, J. E. Greedan, R. F. Kiefl, M. D. Lumsden, W. A. MacFarlane, N. P. Raju, J. E. Sonier, I. Swainson, and Z. Tun. *Cooperative paramagnetism in the geometrically frustrated pyrochlore antiferromagnet  $Tb_2Ti_2O_7$* . Physical Review Letters **82**, 1012 (1999).
- [23] K. Matsuhira, Y. Hinatsu, K. Tenya, and T. Sakakibara. *Low temperature magnetic properties of frustrated pyrochlore ferromagnets  $Ho_2Sn_2O_7$  and  $Ho_2Ti_2O_7$* . Journal of Physics: Condensed Matter **12**, L649 (2000).
- [24] P. A. M. Dirac. *Quantised singularities in the electromagnetic field*. Proceedings of the Royal Society of London. Series A, Containing Papers of a Mathematical and Physical Character **133**, 60 (1931).



- 
- [25] C. Castelnovo, R. Moessner, and S. L. Sondhi. *Magnetic monopoles in spin ice*. Nature **451**, 42 (2008).
- [26] L. D. C. Jaubert and P. C. W. Holdsworth. *Signature of magnetic monopole and Dirac string dynamics in spin ice*. Nature Physics **5**, 258 (2009).
- [27] A. Farhan, M. Saccone, C. F. Petersen, S. Dhuey, R. V. Chopdekar, Y.-L. Huang, N. Kent, Z. Chen, M. J. Alava, T. Lippert, A. Scholl, and S. van Dijken. *Emergent magnetic monopole dynamics in macroscopically degenerate artificial spin ice*. Science Advances **5**, eaav6380 (2019).
- [28] F. Wooten. *Optical Properties of Solids*. Academic Press, New York and London (1972).
- [29] D. B. Tanner. *Optical effects in solids*. Cambridge University Press, Cambridge and New York (2019).
- [30] J. D. Jackson. *Classical Electrodynamics*. John Wiley & Sons, New York (1975).
- [31] C. Kittel. *Introduction to Solid State Physics*. John Wiley & Sons, Inc, New York (2005).
- [32] N. A. Spaldin. *A beginner's guide to the modern theory of polarization*. Journal of Solid State Chemistry **195**, 2 (2012).
- [33] M. Born and K. Huang. *Dynamical theory of crystal lattices*. Clarendon press (1954).
- [34] W. Cochran. *Crystal stability and the theory of ferroelectricity*. Physical Review Letters **3**, 412 (1959).
- [35] P. A. Fleury, J. F. Scott, and J. M. Worlock. *Soft phonon modes and the 110 K phase transition in SrTiO<sub>3</sub>*. Physical Review Letters **21**, 16 (1968).
- [36] J. C. Tsang, J. E. Smith Jr, and M. W. Shafer. *Raman spectroscopy of soft modes at the charge-density-wave phase transition in 2H-NbSe<sub>2</sub>*. Physical Review Letters **37**, 1407 (1976).
- [37] S. B. Vakhrushev, V. A. Isupov, B. E. Kvyatkovsky, N. M. Okuneva, I. P. Pronin, G. A. Smolensky, and P. P. Syrnikov. *Phase transitions and soft modes in sodium bismuth titanate*. Ferroelectrics **63**, 153 (1985).
- [38] J. Petzelt, G. V. Kozlov, and A. A. Volkov. *Dielectric spectroscopy of paraelectric soft modes*. Ferroelectrics **73**, 101 (1987).
- [39] T. P. Dougherty, G. P. Wiederrecht, K. A. Nelson, M. H. Garrett, H. P. Jensen, and C. Warde. *Femtosecond resolution of soft mode dynamics in structural phase transitions*. Science **258**, 770 (1992).

- [40] A. P. Giddy, M. T. Dove, G. S. Pawley, and V. Heine. *The determination of rigid-unit modes as potential soft modes for displacive phase transitions in framework crystal structures*. Acta Crystallographica Section A: Foundations of Crystallography **49**, 697 (1993).
- [41] K. Parlinski, Z. Q. Li, and Y. Kawazoe. *First-principles determination of the soft mode in cubic ZrO<sub>2</sub>*. Physical Review Letters **78**, 4063 (1997).
- [42] A. Kogar, M. S. Rak, S. Vig, A. A. Husain, F. Flicker, Y. I. Joe, L. Venema, G. J. MacDougall, T. C. Chiang, E. Fradkin, J. van Wezel, and P. Abbamonte. *Signatures of exciton condensation in a transition metal dichalcogenide*. Science **358**, 1314 (2017).
- [43] J. Valasek. *Piezo-electric and allied phenomena in Rochelle salt*. Physical Review **17**, 475 (1921).
- [44] R. C. Smith and C. L. Hom. *Domain wall theory for ferroelectric hysteresis*. Journal of Intelligent Material Systems and Structures **10**, 195 (1999).
- [45] W. Cochran. *Dielectric constants and lattice vibrations of cubic ionic crystals*. Zeitschrift für Kristallographie-Crystalline Materials **112**, 465 (1959).
- [46] W. Cochran. *Crystal stability and the theory of ferroelectricity*. Advances in Physics **9**, 387 (1960).
- [47] W. Cochran. *Crystal stability and the theory of ferroelectricity part II. Piezo-electric crystals*. Advances in Physics **10**, 401 (1961).
- [48] A. D. B. Woods, W. Cochran, and B. N. Brockhouse. *Lattice dynamics of alkali halide crystals*. Physical Review **119**, 980 (1960).
- [49] R. H. Lyddane, R. G. Sachs, and E. Teller. *On the polar vibrations of alkali halides*. Physical Review **59**, 673 (1941).
- [50] G. Venkataraman. *Soft modes and structural phase transitions*. Bulletin of Materials Science **1**, 129 (1979).
- [51] G. A. Samara. *Ferroelectricity revisited – advances in materials and physics*. Solid State Physics **56**, 239 (2001).
- [52] L. Landau. *The theory of phase transitions*. Nature **138**, 840 (1936).
- [53] L. D. Landau. *On the theory of phase transitions. I*. Zhurnal Eksperimental noi i Teoreticheskoi Fiziki **11**, 19 (1937).
- [54] L. D. Landau. *On the theory of phase transitions. II*. Zhurnal Eksperimental noi i Teoreticheskoi Fiziki **11**, 627 (1937).
- [55] A. A. Michelson. *ART. XXI.–The relative motion of the earth and the luminiferous ether*. American Journal of Science (1880-1910) **22**, 120 (1881).

- [56] A. A. Michelson and E. W. Morley. *On the relative motion of the earth and of the luminiferous ether*. Sidereal Messenger, vol. 6, pp. 306-310 **6**, 306 (1887).
- [57] H. Günzler and H. U. Gremlich. *IR-Spektroskopie Eine Einführung*. WILEY-VCH Verlag GmbH & Co. KGaA, Weinheim (2003).
- [58] P. R. Griffiths and J. A. de Haseth. *Fourier Transform Infrared Spectrometry*. John Wiley & Sons, Inc., Hoboken, New Jersey (2007).
- [59] P. L. Richards. *Bolometers for infrared and millimeter waves*. Journal of Applied Physics **76**, 1 (1994).
- [60] OPUS Spektroskopiesoftware <https://www.bruker.com/de/products/infrared-near-infrared-and-raman-spectroscopy/opus-spectroscopy-software.html>, accessed 2021-01-30.
- [61] M. Bass, E. W. Van Stryland, D. R. Williams, and W. L. Wolfe. *Handbook of optics – Volume II: Devices, Measurements and Properties*, vol. 2. McGraw-Hill New York (1995).
- [62] H. A. Kramers. *La diffusion de la lumiere par les atomes*. In *Atti Cong. Intern. Fisica (Transactions of Volta Centenary Congress) Como*, vol. 2, pp. 545–557 (1927).
- [63] R. d. L. Kronig. *On the theory of dispersion of X-rays*. Josa **12**, 547 (1926).
- [64] M. Bartelmann, B. Feuerbacher, T. Krüger, D. Lüst, A. Rebhan, and A. Wipf. *Theoretische Physik 2 – Elektrodynamik*. Springer Spektrum, Springer-Verlag Deutschland GmbH, ein Teil von Springer Nature (2018).
- [65] C. Klingshirn. *Semiconductor Optics*. Springer Verlag Berlin Heidelberg New York (1995).
- [66] F. C. Jahoda. *Fundamental absorption of barium oxide from its reflectivity spectrum*. Physical Review **107**, 1261 (1957).
- [67] H. R. Phillip and E. A. Taft. *Kramers-Kronig analysis of reflectance data for diamond*. Physical Review **136**, A1445 (1964).
- [68] D. M. Roessler. *Kramers-Kronig analysis of reflection data*. British Journal of Applied Physics **16**, 1119 (1965).
- [69] U. Kreibig. *Kramers-Kronig analysis of the optical properties of small silver particles*. Zeitschrift für Physik **234**, 307 (1970).
- [70] A. R. Beal and H. P. Hughes. *Kramers-Kronig analysis of the reflectivity spectra of 2H-MoS<sub>2</sub>, 2H-MoSe<sub>2</sub> and 2H-MoTe<sub>2</sub>*. Journal of Physics C: Solid State Physics **12**, 881 (1979).

- [71] E. Shiles, T. Sasaki, M. Inokuti, and D. Y. Smith. *Self-consistency and sum-rule tests in the Kramers-Kronig analysis of optical data: applications to aluminum*. Physical Review B **22**, 1612 (1980).
- [72] F. Gao, D. B. Romero, D. B. Tanner, J. Talvacchio, and M. G. Forrester. *Infrared properties of epitaxial  $La_{2-x}Sr_xCuO_4$  thin films in the normal and superconducting states*. Physical Review B **47**, 1036 (1993).
- [73] A. Pimenov, T. Rudolf, F. Mayr, A. Loidl, A. A. Mukhin, and A. M. Balbashov. *Coupling of phonons and electromagnons in  $GdMnO_3$* . Physical Review B **74**, 100403 (2006).
- [74] A. Akrap, M. Tran, A. Ubaldini, J. Teyssier, E. Giannini, D. Van Der Marel, P. Lerch, and C. C. Homes. *Optical properties of  $Bi_2Te_2Se$  at ambient and high pressures*. Physical Review B **86**, 235207 (2012).
- [75] K. H. Miller, P. W. Stephens, C. Martin, E. Constable, R. A. Lewis, H. Berger, G. L. Carr, and D. B. Tanner. *Infrared phonon anomaly and magnetic excitations in single-crystal  $Cu_3Bi(SeO_3)_2O_2Cl$* . Physical Review B **86**, 174104 (2012).
- [76] H. Okamura. *A simple method for the Kramers-Kronig analysis of reflectance spectra measured with diamond anvil cell*. In *Journal of Physics: Conference Series*, vol. 359, p. 012013. IOP Publishing (2012).
- [77] D. B. Tanner. *Use of X-ray scattering functions in Kramers-Kronig analysis of reflectance*. Physical Review B **91**, 035123 (2015).
- [78] A. L. Cauchy. *Oeuvres complètes*. Ser. 1, 4, Paris (1890).
- [79] S. S. Ng, Z. Hassan, and H. A. Hassan. *Kramers-Kronig analysis of infrared reflectance spectra with a single resonance*. Jurnal Teknologi **44**, 67 (2012).
- [80] L. Zehnder. *Ein neuer Interferenzrefraktor*. Zeitschrift für Instrumentenkunde **11**, 275 (1891).
- [81] L. Mach. *Über einen Interferenzrefraktor*. Zeitschrift für Instrumentenkunde **12**, 89 (1892).
- [82] A. A. Volkov, Y. G. Goncharov, G. V. Kozlov, S. P. Lebedev, and A. M. Prokhorov. *Dielectric measurements in the submillimeter wavelength region*. Infrared Physics **25**, 369 (1985).
- [83] G. Kozlov and A. Volkov. *Coherent source submillimeter wave spectroscopy*. In *Millimeter and submillimeter wave spectroscopy of solids*, pp. 51–109. Springer (1998).
- [84] A. Shuvaev. *Spectroscopic study of manganites with magnetoelectric coupling (PhD thesis)*. TU Wien (2013).

- [85] L. Bergen, L. Weymann, J. Wettstein, A. M. Kuzmenko, A. A. Mukhin, B. V. Mill, A. Pimenov, and E. Constable. *Lattice contributions to the anisotropic dielectric response of rare-earth langasites*. Physical Review B **104**, 024106 (2021).
- [86] L. Weymann, L. Bergen, T. Kain, A. Pimenov, A. Shuvaev, E. Constable, D. Szaller, B. V. Mill, A. M. Kuzmenko, V. Y. Ivanov, N. V. Kostyuchenko, A. I. Popov, A. K. Zvezdin, A. Pimenov, A. A. Mukhin, and M. Mostovoy. *Unusual magnetoelectric effect in paramagnetic rare-earth langasite*. npj Quantum Materials **5**, 1 (2020).
- [87] B. V. Mill and Y. V. Pisarevsky. *Langasite-type materials: from discovery to present state*. In *Proceedings of the 2000 IEEE/EIA International Frequency Control Symposium and Exhibition (Cat. No. 00CH37052)*, pp. 133–144. IEEE (2000).
- [88] B. V. Mill, E. L. Belokoneva, and T. Fukuda. *Novel Gallates and Aluminates of the  $Ca_3Ga_2Ge_4O_{14}$  Crystal Structure*. Russian Journal of Inorganic Chemistry **43**, 1032 (1998).
- [89] W. Eysel, U. Lambert, B. E. Mayer, C. Renkenberger, and B. Nuber. *Crystal structures and crystal chemistry of compounds  $M_{5-p}T_{4+p}O_{14}$* . Zeitschrift für Kristallographie-Crystalline Materials **201**, 235 (1992).
- [90] J. Stade, L. Bohatý, M. Hengst, and R. B. Heimann. *Electro-optic, piezoelectric and dielectric properties of langasite ( $La_3Ga_5SiO_{14}$ ), langanite ( $La_3Ga_{5.5}Nb_{0.5}O_{14}$ ) and langataite ( $La_3Ga_{5.5}Ta_{0.5}O_{14}$ )*. Crystal Research and Technology: Journal of Experimental and Industrial Crystallography **37**, 1113 (2002).
- [91] J. Bohm, R. B. Heimann, M. Hengst, R. Roewer, and J. Schindler. *Czochralski growth and characterization of piezoelectric single crystals with langasite structure:  $La_3Ga_5SiO_{14}$  (LGS),  $La_3Ga_{5.5}Nb_{0.5}O_{14}$  (LGN), and  $La_3Ga_{5.5}Ta_{0.5}O_{14}$  (LGT): Part I*. Journal of Crystal Growth **204**, 128 (1999).
- [92] M. M. Markina, B. V. Mill, G. Pristáš, M. Marcin, S. A. Klimin, K. N. Boldyrev, and M. N. Popova.  *$La_3CrGe_3Be_2O_{14}$  and  $Nd_3CrGe_3Be_2O_{14}$ : New magnetic compounds of the langasite family*. Journal of Alloys and Compounds **779**, 380 (2019).
- [93] A. A. Kaminskii, B. V. Mill, I. M. Silvestrova, and G. G. Khodzhabagian. *The nonlinearly active material  $(La_{1-x}Nd_x)_3Ga_5SiO_{14}$* . Akademiia Nauk SSSR Izvestiia Serii Fizicheskaiia **47**, 1903 (1983).
- [94] I. Andreev and M. F. Dubovik. *A new piezoelectric material, langasite ( $La_3Ga_5SiO_{14}$ ), with a zero temperature coefficient of the elastic vibration frequency*. Soviet Technical Physics Letters **10**, 205 (1984).

- [95] I. H. Jung and K. H. Auh. *Crystal growth and piezoelectric properties of langasite ( $\text{La}_3\text{Ga}_5\text{SiO}_{14}$ ) crystals*. Materials Letters **41**, 241 (1999).
- [96] T. Iwataki, H. Ohsato, K. Tanaka, H. Morikoshi, J. Sato, and K. Kawasaki. *Mechanism of the piezoelectricity of langasite based on the crystal structures*. Journal of the European Ceramic Society **21**, 1409 (2001).
- [97] H. Ogi, N. Nakamura, K. Sato, M. Hirao, and S. Uda. *Elastic, anelastic, and piezoelectric coefficients of langasite: Resonance ultrasound spectroscopy with laser-Doppler interferometry*. IEEE Transactions on Ultrasonics, Ferroelectrics, and Frequency Control **50**, 553 (2003).
- [98] N. Araki, H. Ohsato, K. Kakimoto, T. Kuribayashi, Y. Kudoh, and H. Morikoshi. *Origin of piezoelectricity for langasite  $\text{A}_3\text{Ga}_5\text{SiO}_{14}$  ( $A = \text{La}$  and  $\text{Nd}$ ) under high pressure*. Journal of the European Ceramic Society **27**, 4099 (2007).
- [99] R. Tarumi, H. Nitta, H. Ogi, and M. Hirao. *Low-temperature elastic constants and piezoelectric coefficients of langasite ( $\text{La}_3\text{Ga}_5\text{SiO}_{14}$ )*. Philosophical Magazine **91**, 2140 (2011).
- [100] H. Fritze and H. L. Tuller. *Langasite for high-temperature bulk acoustic wave applications*. Applied Physics Letters **78**, 976 (2001).
- [101] H. Seh, H. L. Tuller, and H. Fritze. *Langasite for high-temperature acoustic wave gas sensors*. Sensors and Actuators B: Chemical **93**, 169 (2003).
- [102] M. P. Da Cunha, R. J. Lad, T. Moonlight, G. Bernhardt, and D. J. Frankel. *High temperature stability of langasite surface acoustic wave devices*. In *2008 IEEE Ultrasonics Symposium*, pp. 205–208. IEEE (2008).
- [103] A. Ghosh, C. Zhang, S. Shi, and H. Zhang. *High temperature  $\text{CO}_2$  sensing and its cross-sensitivity towards  $\text{H}_2$  and  $\text{CO}$  gas using calcium doped  $\text{ZnO}$  thin film coated langasite SAW sensor*. Sensors and Actuators B: Chemical **301**, 126958 (2019).
- [104] H. Fritze, H. L. Tuller, H. Seh, and G. Borchardt. *High temperature nanobalance sensor based on langasite*. Sensors and Actuators B: Chemical **76**, 103 (2001).
- [105] H. Fritze, H. Seh, H. L. Tuller, and G. Borchardt. *Operation limits of langasite high temperature nanobalances*. Journal of the European Ceramic Society **21**, 1473 (2001).
- [106] M. Nespolo, M. I. Aroyo, and B. Souvignier. *Crystallographic shelves: Space-group hierarchy explained*. Journal of Applied Crystallography **51**, 1481 (2018).
- [107] B. A. Maksimov, V. N. Molchanov, B. V. Mill, E. L. Belokoneva, M. K. Rabadanov, A. A. Pugacheva, Y. V. Pisarevskii, and V. I. Simonov. *Absolute structure of  $\text{La}_3\text{Ga}_5\text{SiO}_{14}$  langasite crystals*. Crystallography Reports **50**, 751 (2005).

- [108] K. Momma and F. Izumi. *VESTA 3 for three-dimensional visualization of crystal, volumetric and morphology data*. Journal of Applied Crystallography **44**, 1272 (2011).
- [109] E. L. Belokoneva, S. Y. Stefanovich, Y. V. Pisarevskij, and A. V. Mosunov. *Refined structures of  $\text{La}_3\text{Ga}_5\text{SiO}_{14}$  and  $\text{Pb}_3\text{Ga}_2\text{Ge}_4\text{O}_{14}$  and the crystal-chemical regularities in the structure and properties of compounds of the langacite family*. Zhurnal Neorganicheskoy Khimii **45**, 1786 (2000).
- [110] H. Ohsato. *Origin of piezoelectricity on langasite*. Materials Science and Technology, edited by: Hutagalung, S., IntechOpen, Rijeka, Croatia pp. 15–40 (2012).
- [111] K. Marty, P. Bordet, V. Simonet, M. Loire, R. Ballou, C. Darie, J. Kljun, P. Bonville, O. Isnard, P. Lejay, B. Zawilski, and C. Simon. *Magnetic and dielectric properties in the langasite-type compounds:  $\text{A}_3\text{BFe}_3\text{D}_2\text{O}_{14}$  ( $A = \text{Ba}, \text{Sr}, \text{Ca}$ ;  $B = \text{Ta}, \text{Nb}, \text{Sb}$ ;  $D = \text{Ge}, \text{Si}$ )*. Physical Review B **81**, 054416 (2010).
- [112] M. Loire, V. Simonet, S. Petit, K. Marty, P. Bordet, P. Lejay, J. Ollivier, M. Enderle, P. Steffens, E. Ressouche, A. Zorko, and R. Ballou. *Parity-Broken Chiral Spin Dynamics in  $\text{Ba}_3\text{NbFe}_3\text{Si}_2\text{O}_{14}$* . Physical Review Letters **106**, 207201 (2011).
- [113] I. S. Lyubutin, P. G. Naumov, B. V. Mill, K. V. Frolov, and E. I. Demikhov. *Structural and magnetic properties of the iron-containing langasite family  $\text{A}_3\text{MFe}_3\text{X}_2\text{O}_{14}$  ( $A = \text{Ba}, \text{Sr}$ ;  $M = \text{Sb}, \text{Nb}, \text{Ta}$ ;  $X = \text{Si}, \text{Ge}$ ) observed by Mössbauer spectroscopy*. Physical Review B **84**, 214425 (2011).
- [114] L. Chaix, R. Ballou, A. Cano, S. Petit, S. De Brion, J. Ollivier, L.-P. Regnault, E. Ressouche, E. Constable, C. V. Colin, A. Zorko, V. Scagnoli, J. Balay, P. Lejay, and V. Simonet. *Helical bunching and symmetry lowering inducing multiferroicity in Fe langasites*. Physical Review B **93**, 214419 (2016).
- [115] M. Ramakrishnan, E. Constable, A. Cano, M. Mostovoy, J. S. White, N. Gung, E. Schierle, S. De Brion, C. V. Colin, F. Gay, P. Lejay, E. Ressouche, E. Weschke, V. Scagnoli, R. Ballou, V. Simonet, and U. Staub. *Field-induced double spin spiral in a frustrated chiral magnet*. npj Quantum Materials **4**, 1 (2019).
- [116] H. D. Zhou, B. W. Vogt, J. A. Janik, Y.-J. Jo, L. Balicas, Y. Qiu, J. R. D. Copley, J. S. Gardner, and C. R. Wiebe. *Partial field-induced magnetic order in the spin-liquid kagome  $\text{Nd}_3\text{Ga}_5\text{SiO}_{14}$* . Physical Review Letters **99**, 236401 (2007).
- [117] J. Robert, V. Simonet, B. Canals, R. Ballou, P. Bordet, P. Lejay, and A. Stunault. *Spin-liquid correlations in the Nd-langasite anisotropic kagome antiferromagnet*. Physical Review Letters **96**, 197205 (2006).

- [118] J. Robert, V. Simonet, B. Canals, R. Ballou, P. Bordet, P. Lejay, and A. Stunault. *Erratum: Spin-liquid correlations in the Nd-langasite anisotropic kagome antiferromagnet [Phys. Rev. Lett. PRLTAO0031-9007 96, 197205 (2006)]*. Physical Review Letters **97**, 259901 (2006).
- [119] V. Simonet, R. Ballou, J. Robert, B. Canals, F. Hippert, P. Bordet, P. Lejay, P. Fouquet, J. Ollivier, and D. Braithwaite. *Hidden magnetic frustration by quantum relaxation in anisotropic Nd langasite*. Physical Review Letters **100**, 237204 (2008).
- [120] R. D. Shannon. *Revised effective ionic radii and systematic studies of interatomic distances in halides and chalcogenides*. Acta crystallographica section A: crystal physics, diffraction, theoretical and general crystallography **32**, 751 (1976).
- [121] A. B. Kuzmenko. *Kramers–Kronig constrained variational analysis of optical spectra*. Review of Scientific Instruments **76**, 083108 (2005).
- [122] Guide to RefFIT - software to fit optical spectra (Manual) <https://reffit.ch/wp-content/uploads/2018/10/Manual.pdf>, accessed 2020-08-11.
- [123] RefFIT - Homepage <https://reffit.ch>, accessed 2020-08-11.
- [124] E. Kroumova, M. I. Aroyo, J. M. Perez-Mato, A. Kirov, C. Capillas, S. Ivantchev, and H. Wondratschek. *Bilbao crystallographic server: useful databases and tools for phase-transition studies*. Phase Transitions: A Multinational Journal **76**, 155 (2003).
- [125] Bilbao Crystallographic Server <https://www.cryst.ehu.es/rep/sam.html>, accessed 2020-11-30.
- [126] L. Weymann. *Novel Static and Dynamic Phenomena in Magnetoelectric Materials (PhD thesis)*. TU Wien (2020).
- [127] X. S. Xu, T. V. Brinzari, S. McGill, H. D. Zhou, C. R. Wiebe, and J. L. Musfeldt. *Absence of Spin Liquid Behavior in  $Nd_3Ga_5SiO_{14}$  Using Magneto-Optical Spectroscopy*. Physical Review Letters **103**, 267402 (2009).
- [128] L. Bergen *et al.* *Polar soft-mode dynamics in candidate antiferroelectric francisite  $Cu_3Bi(SeO_3)_2O_2Cl$* . under preparation .
- [129] E. Malysheva. *Infrared studies on antiferroelectric candidate francisite  $Cu_3Bi(SeO_3)_2O_2Cl$  (Bachelor’s thesis)*. TU Wien (2018).
- [130] E. Malysheva. *Temperature dependence of lattice contribution to dielectric response of francisite  $Cu_3Bi(SeO_3)_2O_2Cl$  (Project work)*. TU Wien (2019).
- [131] A. Pring, B. M. Gatehouse, and W. D. Birch. *Francisite,  $Cu_3Bi(SeO_3)_2O_2Cl$ , a new mineral from Iron Monarch, South Australia; description and crystal structure*. American Mineralogist **75**, 1421 (1990).



- [132] E. Constable, S. Raymond, S. Petit, E. Ressouche, F. Bourdarot, J. Debray, M. Josse, O. Fabelo, H. Berger, S. DeBrion, and V. Simonet. *Magnetic and dielectric order in the kagomelike francisite  $Cu_3Bi(SeO_3)_2O_2Cl$* . Physical Review B **96**, 014413 (2017).
- [133] P. Millet, B. Bastide, V. Pashchenko, S. Gnatchenko, V. Gapon, Y. Ksari, and A. Stepanov. *Syntheses, crystal structures and magnetic properties of francisite compounds  $Cu_3Bi(SeO_3)_2O_2X$  ( $X= Cl, Br$  and  $I$ )*. Journal of Materials Chemistry **11**, 1152 (2001).
- [134] R. Berrigan and B. M. Gatehouse.  *$Cu_3Er(SeO_3)_2O_2Cl$ , the erbium analogue of francisite*. Acta Crystallographica Section C: Crystal Structure Communications **52**, 496 (1996).
- [135] K. V. Zakharov, E. A. Zvereva, M. M. Markina, M. I. Stratan, E. S. Kuznetsova, S. F. Dunaev, P. S. Berdonosov, V. A. Dolgikh, A. V. Olenov, S. A. Klimin, L. S. Mazaev, M. A. Kashchenko, M. A. Ahmed, A. Banerjee, S. Bandyopadhyay, A. Iqbal, B. Rahaman, T. Saha-Dasgupta, and A. N. Vasiliev. *Magnetic, resonance, and optical properties of  $Cu_3Sm(SeO_3)_2O_2Cl$ : A rare-earth francisite compound*. Physical Review B **94**, 054401 (2016).
- [136] K. V. Zakharov, E. A. Zvereva, E. S. Kuznetsova, P. S. Berdonosov, V. A. Dolgikh, M. M. Markina, A. V. Olenov, A. A. Shakin, O. S. Volkova, and A. N. Vasiliev. *Two new lanthanide members of francisite family  $Cu_3Ln(SeO_3)_2O_2Cl$  ( $Ln= Eu, Lu$ )*. Journal of Alloys and Compounds **685**, 442 (2016).
- [137] V. Gnezdilov, Y. Pashkevich, P. Lemmens, V. Kurnosov, P. Berdonosov, V. Dolgikh, E. Kuznetsova, V. Pryadun, K. Zakharov, and A. Vasiliev. *Lattice and magnetic instabilities in  $Cu_3Bi(SeO_3)_2O_2X$  ( $X= Br, Cl$ )*. Physical Review B **96**, 115144 (2017).
- [138] I. Dzyaloshinsky. *A thermodynamic theory of “weak” ferromagnetism of anti-ferromagnetics*. Journal of Physics and Chemistry of Solids **4**, 241 (1958).
- [139] T. Moriya. *New mechanism of anisotropic superexchange interaction*. Physical Review Letters **4**, 228 (1960).
- [140] I. Rousochatzakis, J. Richter, R. Zinke, and A. A. Tsirlin. *Frustration and Dzyaloshinsky-Moriya anisotropy in the kagome francisites  $Cu_3Bi(SeO_3)_2O_2X$  ( $X= Br, Cl$ )*. Physical Review B **91**, 024416 (2015).
- [141] M. Pregelj, O. Zaharko, A. Günther, A. Loidl, V. Tsurkan, and S. Guerrero. *Magnetic ground state and two-dimensional behavior in pseudo-kagome layered system  $Cu_3Bi(SeO_3)_2O_2Cl$* . Physical Review B **86**, 144409 (2012).
- [142] K. V. Zakharov, E. A. Zvereva, P. S. Berdonosov, E. S. Kuznetsova, V. A. Dolgikh, L. Clark, C. Black, P. Lightfoot, W. Kockelmann, Z. V. Pchelkina, S. V.

- Streltsov, O. S. Volkova, and A. N. Vasiliev. *Thermodynamic properties, electron spin resonance, and underlying spin model in  $\text{Cu}_3\text{Y}(\text{SeO}_3)_2\text{O}_2\text{Cl}$* . Physical Review B **90**, 214417 (2014).
- [143] D. A. Prishchenko, A. A. Tsirlin, V. Tsurkan, A. Loidl, A. Jesche, and V. G. Mazurenko. *Antiferroelectric instability in the kagome francisites  $\text{Cu}_3\text{Bi}(\text{SeO}_3)_2\text{O}_2\text{X}$  ( $\text{X} = \text{Cl}, \text{Br}$ )*. Physical Review B **95**, 064102 (2017).
- [144] C. Milesi-Brault, C. Toulouse, E. Constable, H. Aramberri, V. Simonet, S. de Brion, H. Berger, L. Paolasini, A. Bosak, J. Íñiguez, and M. Guennou. *Archetypal Soft-Mode-Driven Antipolar Transition in Francisite  $\text{Cu}_3\text{Bi}(\text{SeO}_3)_2\text{O}_2\text{Cl}$* . Physical Review Letters **124**, 097603 (2020).
- [145] Z. Wang, M. Schmidt, Y. Goncharov, V. Tsurkan, H. K. von Nidda, A. Loidl, and J. Deisenhofer. *Terahertz spectroscopy in the pseudo-kagome system  $\text{Cu}_3\text{Bi}(\text{SeO}_3)_2\text{O}_2\text{Br}$* . Physical Review B **86**, 174411 (2012).
- [146] C. Kittel. *Theory of antiferroelectric crystals*. Physical Review **82**, 729 (1951).
- [147] J. F. Scott. *Soft-mode spectroscopy: Experimental studies of structural phase transitions*. Reviews of Modern Physics **46**, 83 (1974).
- [148] P. Tolédano and M. Guennou. *Theory of antiferroelectric phase transitions*. Physical Review B **94**, 014107 (2016).
- [149] B. Jaffe. *Antiferroelectric ceramics with field-enforced transitions: A new non-linear circuit element*. Proceedings of the IRE **49**, 1264 (1961).
- [150] Y.-H. Kim and J.-J. Kim. *Scaling behavior of an antiferroelectric hysteresis loop*. Physical Review B **55**, R11933 (1997).
- [151] K. M. Rabe. *Antiferroelectricity in oxides: A reexamination*. Functional Metal Oxides pp. 221–244 (2013).
- [152] J. Ge, Y. Chen, X. Dong, D. Rémiens, X. Guo, F. Cao, and G. Wang. *Dynamic hysteresis and scaling behavior in epitaxial antiferroelectric film*. Thin Solid Films **584**, 108 (2015).
- [153] M. E. Lines and A. M. Glass. *Principles and applications of ferroelectrics and related materials*. Oxford University Press (2001).
- [154] G. Shirane, E. Sawaguchi, and Y. Takagi. *Dielectric properties of lead zirconate*. Physical Review **84**, 476 (1951).
- [155] G. Shirane. *Ferroelectricity and antiferroelectricity in ceramic  $\text{PbZrO}_3$  containing Ba or Sr*. Physical Review **86**, 219 (1952).
- [156] E. Sawaguchi. *Ferroelectricity versus antiferroelectricity in the solid solutions of  $\text{PbZrO}_3$  and  $\text{PbTiO}_3$* . Journal of the Physical Society of Japan **8**, 615 (1953).

- [157] H. Fujishita and S. Hoshino. *A study of structural phase transitions in antiferroelectric  $PbZrO_3$  by neutron diffraction*. Journal of the Physical Society of Japan **53**, 226 (1984).
- [158] Z. G. Fthenakis and I. Ponomareva. *Dynamics of antiferroelectric phase transition in  $PbZrO_3$* . Physical Review B **96**, 184110 (2017).
- [159] A. K. Tagantsev, K. Vaideeswaran, S. B. Vakhrushev, A. V. Filimonov, R. G. Burkovsky, A. Shaganov, D. Andronikova, A. I. Rudskoy, A. Q. R. Baron, H. Uchiyama, D. Chernyshov, A. Bosak, Z. Ujma, K. Roleder, A. Majchrowski, J.-H. Ko, and N. Setter. *The origin of antiferroelectricity in  $PbZrO_3$* . Nature Communications **4**, 1 (2013).
- [160] S. Inui, N. Iimura, T. Suzuki, H. Iwane, K. Miyachi, Y. Takanishi, and A. Fukuda. *Thresholdless antiferroelectricity in liquid crystals and its application to displays*. Journal of Materials Chemistry **6**, 671 (1996).
- [161] J. M. Otón, X. Quintana, P. L. Castillo, A. Lara, V. Urruchi, and N. Bennis. *Antiferroelectric liquid crystal displays*. Optoelectronics Review pp. 263–270 (2004).
- [162] S. T. Lagerwall. *Ferroelectric and antiferroelectric liquid crystals*. Ferroelectrics **301**, 15 (2004).
- [163] K. Singh. *Antiferroelectric lead zirconate, a material for energy storage*. Ferroelectrics **94**, 433 (1989).
- [164] L. Zhao, Q. Liu, J. Gao, S. Zhang, and J.-F. Li. *Lead-free antiferroelectric silver niobate tantalate with high energy storage performance*. Advanced Materials **29**, 1701824 (2017).
- [165] H. Wang, Y. Liu, T. Yang, and S. Zhang. *Ultra-high energy-storage density in antiferroelectric ceramics with field-induced multiphase transitions*. Advanced Functional Materials **29**, 1807321 (2019).
- [166] N. Dalal, A. Klymachyov, and A. Bussmann-Holder. *Coexistence of order-disorder and displacive features at the phase transitions in hydrogen-bonded solids: squaric acid and its analogs*. Physical Review Letters **81**, 5924 (1998).
- [167] S. Y. Stefanovich, A. A. Belik, M. Azuma, M. Takano, O. V. Baryshnikova, V. A. Morozov, B. I. Lazoryak, O. I. Lebedev, and G. Van Tendeloo. *Antiferroelectric phase transition in  $Sr_9In(PO_4)_7$* . Physical Review B **70**, 172103 (2004).
- [168] O. Gunaydin-Sen, R. Fu, R. Achey, and N. S. Dalal. *Order-disorder and displacive behavior of the cation ( $NH_4^+$ ) sites in the hydrogen-bonded antiferroelectric  $NH_4H_2AsO_4$ :  $^{15}N$  NMR evidence*. Ferroelectrics **337**, 153 (2006).

- [169] N. S. Dalal, O. Gunaydin-Sen, and A. Bussmann-Holder. *Experimental evidence for the coexistence of order/disorder and displacive behavior of hydrogen-bonded ferroelectrics and antiferroelectrics*. Ferro- and Antiferroelectricity pp. 23–50 (2006).
- [170] T. Fukami, S. Akahoshi, K. Hukuda, and T. Yagi. *Refinement of the crystal structure of  $NH_4H_2PO_4$  above and below antiferroelectric phase transition temperature*. Journal of the Physical Society of Japan **56**, 2223 (1987).
- [171] P. Jain, N. S. Dalal, B. H. Toby, H. W. Kroto, and A. K. Cheetham. *Order-disorder antiferroelectric phase transition in a hybrid inorganic-organic framework with the perovskite architecture*. Journal of the American Chemical Society **130**, 10450 (2008).
- [172] S. Horiuchi, R. Kumai, and S. Ishibashi. *Strong polarization switching with low-energy loss in hydrogen-bonded organic antiferroelectrics*. Chemical Science **9**, 425 (2018).
- [173] D. Atencio, M. B. Andrade, A. G. Christy, R. Gieré, and P. M. Kartashov. *The pyrochlore supergroup of minerals: nomenclature*. The Canadian Mineralogist **48**, 673 (2010).
- [174] Mineralienatlas <https://www.mineralienatlas.de/lexikon/index.php/MineralData?mineral=Pyrochlor-Gruppe>, accessed 2021-03-30.
- [175] R. Trujillano, J. A. Martín, and V. Rives. *Hydrothermal synthesis of  $Sm_2Sn_2O_7$  pyrochlore accelerated by microwave irradiation. A comparison with the solid state synthesis method*. Ceramics International **42**, 15950 (2016).
- [176] F. Wöhler. *Ueber den Pyrochlor, eine neue Mineralspecies*. Annalen der Physik **83**, 417 (1826).
- [177] mindat.org <https://www.mindat.org/min-3316.html>, accessed 2021-03-30.
- [178] A. Christy and D. Atencio. *Clarification of status of species in the pyrochlore supergroup*. Mineralogical Magazine **77**, 13 (2013).
- [179] H. R. v. Gaertner. *Die Kristallstrukturen von Loparit und Pyrochlor*. Neues Jahrbuch für Mineralogie und Beilage **61**, 1 (1930).
- [180] J. S. Gardner, M. J. P. Gingras, and J. E. Greedan. *Magnetic pyrochlore oxides*. Reviews of Modern Physics **82**, 53 (2010).
- [181] M. A. Subramanian, G. Aravamudan, and G. V. S. Rao. *Oxide pyrochlores-A review*. Progress in Solid State Chemistry **15**, 55 (1983).
- [182] R. A. McCauley. *Structural characteristics of pyrochlore formation*. Journal of Applied Physics **51**, 290 (1980).

- [183] M. V. Talanov and V. M. Talanov. *Formation of breathing pyrochlore lattices: structural, thermodynamic and crystal chemical aspects*. CrystEngComm **22**, 1176 (2020).
- [184] W. R. Cook Jr. and H. Jaffe. *Ferroelectricity in oxides of face-centered cubic structure*. Physical Review **89**, 1297 (1953).
- [185] F. Jona, G. Shirane, and R. Pepinsky. *Dielectric, X-ray, and optical study of ferroelectric  $Cd_2Nb_2O_7$  and related compounds*. Physical Review **98**, 903 (1955).
- [186] J. E. Greedan, M. Sato, X. Yan, and F. S. Razavi. *Spin-glass-like behavior in  $Y_2Mo_2O_7$ , a concentrated, crystalline system with negligible apparent disorder*. Solid State Communications **59**, 895 (1986).
- [187] J. Reimers, J. Greedan, and M. Sato. *The crystal structure of the spin-glass pyrochlore,  $Y_2Mo_2O_7$* . Journal of Solid State Chemistry **72**, 390 (1988).
- [188] C. H. Booth, J. S. Gardner, G. H. Kwei, R. H. Heffner, F. Bridges, and M. A. Subramanian. *Local lattice disorder in the geometrically frustrated spin-glass pyrochlore  $Y_2Mo_2O_7$* . Physical Review B **62**, R755 (2000).
- [189] N. P. Raju, E. Gmelin, and R. K. Kremer. *Magnetic-susceptibility and specific-heat studies of spin-glass-like ordering in the pyrochlore compounds  $R_2Mo_2O_7$  ( $R= Y, Sm, \text{ or } Gd$ )*. Physical Review B **46**, 5405 (1992).
- [190] G. Ehlers, J. Greedan, J. Stewart, K. Rule, P. Fouquet, A. Cornelius, C. Adriano, P. Pagliuso, Y. Qiu, and J. S. Gardner. *High-resolution neutron scattering study of  $Tb_2Mo_2O_7$ : A geometrically frustrated spin glass*. Physical Review B **81**, 224405 (2010).
- [191] P. W. Anderson. *Resonating valence bonds: A new kind of insulator?* Materials Research Bulletin **8**, 153 (1973).
- [192] B. Canals and C. Lacroix. *Pyrochlore antiferromagnet: A three-dimensional quantum spin liquid*. Physical Review Letters **80**, 2933 (1998).
- [193] R. Sibille, E. Lhotel, V. Pomjakushin, C. Baines, T. Fennell, and M. Kenzelmann. *Candidate quantum spin liquid in the  $Ce^{3+}$  pyrochlore stannate  $Ce_2Sn_2O_7$* . Physical Review Letters **115**, 097202 (2015).
- [194] B. Gao, T. Chen, D. W. Tam, C.-L. Huang, K. Sasmal, D. T. Adroja, F. Ye, H. Cao, G. Sala, M. B. Stone, C. Baines, J. A. T. Verezhak, H. Hu, J. H. Chung, X. Xu, S. W. Cheong, M. Nallaiyan, S. Spagna, M. B. Maple, A. H. Nevidomskyy *et al.* *Experimental signatures of a three-dimensional quantum spin liquid in effective spin-1/2  $Ce_2Zr_2O_7$  pyrochlore*. Nature Physics **15**, 1052 (2019).

- [195] Y.-J. Kao, M. Enjalran, A. Del Maestro, H. R. Molavian, and M. J. Gingras. *Understanding paramagnetic spin correlations in the spin-liquid pyrochlore  $Tb_2Ti_2O_7$* . Physical Review B **68**, 172407 (2003).
- [196] R. Sibille, E. Lhotel, M. C. Hatnean, G. J. Nilsen, G. Ehlers, A. Cervellino, E. Ressouche, M. Frontzek, O. Zaharko, V. Pomjakushin, U. Stuhr, H. C. Walker, D. T. Adroja, H. Luetkens, C. Baines, A. Amato, G. Balakrishnan, T. Fennell, and M. Kenzelmann. *Coulomb spin liquid in anion-disordered pyrochlore  $Tb_2Hf_2O_7$* . Nature Communications **8**, 1 (2017).
- [197] M. J. Harris, S. T. Bramwell, D. F. McMorrow, T. H. Zeiske, and K. W. Godfrey. *Geometrical frustration in the ferromagnetic pyrochlore  $Ho_2Ti_2O_7$* . Physical Review Letters **79**, 2554 (1997).
- [198] L. Pauling. *The structure and entropy of ice and of other crystals with some randomness of atomic arrangement*. Journal of the American Chemical Society **57**, 2680 (1935).
- [199] J. D. Bernal and R. H. Fowler. *A Theory of water and ionic solution, with particular reference to hydrogen and hydroxyl ions*. The Journal of Chemical Physics **1**, 515 (1933).
- [200] W. F. Giaque and M. F. Ashley. *Molecular rotation in ice at 10 K. Free energy of formation and entropy of water*. Physical Review **43**, 81 (1933).
- [201] W. F. Giaque and J. W. Stout. *The entropy of water and the third law of thermodynamics. The heat capacity of ice from 15 to 273 K*. Journal of the American Chemical Society **58**, 1144 (1936).
- [202] L. E. Boltzmann. *Über die Beziehung zwischen dem zweiten Hauptsatze der mechanischen Wärmetheorie und der Wahrscheinlichkeitsrechnung respektive den Sätzen über das Wärmegleichgewicht*. In: Sitzungsberichte der kaiserlichen Akademie der Wissenschaften zu Wien **II**, 373 (1877).
- [203] A. P. Ramirez, A. Hayashi, R. J. Cava, R. Siddharthan, and B. Shastry. *Zero-point entropy in ‘spin ice’*. Nature **399**, 333 (1999).
- [204] J. G. Rau and M. J. P. Gingras. *Magnitude of quantum effects in classical spin ices*. Physical Review B **92**, 144417 (2015).
- [205] P. W. Anderson. *Ordering and antiferromagnetism in ferrites*. Physical Review **102**, 1008 (1956).
- [206] S. T. Bramwell, M. J. P. Gingras, and J. N. Reimers. *Order by disorder in an anisotropic pyrochlore lattice antiferromagnet*. Journal of Applied Physics **75**, 5523 (1994).
- [207] S. T. Bramwell and M. J. Harris. *The history of spin ice*. Journal of Physics: Condensed Matter **32**, 374010 (2020).

- 
- [208] S. T. Bramwell and M. J. Harris. *Frustration in Ising-type spin models on the pyrochlore lattice*. Journal of Physics: Condensed Matter **10**, L215 (1998).
- [209] H. Kadowaki, Y. Ishii, K. Matsuhira, and Y. Hinatsu. *Neutron scattering study of dipolar spin ice  $\text{Ho}_2\text{Sn}_2\text{O}_7$ : Frustrated pyrochlore magnet*. Physical Review B **65**, 144421 (2002).
- [210] G. Ehlers, A. Huq, S. O. Diallo, C. Adriano, K. C. Rule, A. L. Cornelius, P. Fouquet, P. G. Pagliuso, and J. S. Gardner. *Low energy spin dynamics in the spin ice  $\text{Ho}_2\text{Sn}_2\text{O}_7$* . Journal of Physics: Condensed Matter **24**, 076005 (2012).
- [211] K. Matsuhira, Y. Hinatsu, and T. Sakakibara. *Novel dynamical magnetic properties in the spin ice compound  $\text{Dy}_2\text{Ti}_2\text{O}_7$* . Journal of Physics: Condensed Matter **13**, L737 (2001).
- [212] Y. Qi, T. Brintlinger, and J. Cumings. *Direct observation of the ice rule in an artificial kagome spin ice*. Physical Review B **77**, 094418 (2008).
- [213] R. F. Wang, C. Nisoli, R. S. Freitas, J. Li, W. McConville, B. J. Cooley, M. S. Lund, N. Samarth, C. Leighton, V. H. Crespi, and P. Schiffer. *Artificial ‘spin ice’ in a geometrically frustrated lattice of nanoscale ferromagnetic islands*. Nature **439**, 303 (2006).
- [214] S. Zhang, I. Gilbert, C. Nisoli, G.-W. Chern, M. J. Erickson, L. O’Brien, C. Leighton, P. E. Lammert, V. H. Crespi, and P. Schiffer. *Crystallites of magnetic charges in artificial spin ice*. Nature **500**, 553 (2013).
- [215] M. J. P. Gingras, B. C. Den Hertog, M. Faucher, J. S. Gardner, S. R. Dunsiger, L. J. Chang, B. D. Gaulin, N. P. Raju, and J. E. Greedan. *Thermodynamic and single-ion properties of  $\text{Tb}^{3+}$  within the collective paramagnetic-spin liquid state of the frustrated pyrochlore antiferromagnet  $\text{Tb}_2\text{Ti}_2\text{O}_7$* . Physical Review B **62**, 6496 (2000).
- [216] N. Hamaguchi, T. Matsushita, N. Wada, Y. Yasui, and M. Sato. *Low-temperature phases of the pyrochlore compound  $\text{Tb}_2\text{Ti}_2\text{O}_7$* . Physical Review B **69**, 132413 (2004).
- [217] K. C. Rule, J. P. C. Ruff, B. D. Gaulin, S. R. Dunsiger, J. S. Gardner, J. P. Clancy, M. J. Lewis, H. A. Dabkowska, I. Mirebeau, P. Manuel, Y. Qiu, and J. R. D. Copley. *Field-induced order and spin waves in the pyrochlore antiferromagnet  $\text{Tb}_2\text{Ti}_2\text{O}_7$* . Physical Review Letters **96**, 177201 (2006).
- [218] J. P. C. Ruff, B. D. Gaulin, J. P. Castellan, K. C. Rule, J. P. Clancy, J. Rodriguez, and H. A. Dabkowska. *Structural fluctuations in the spin-liquid state of  $\text{Tb}_2\text{Ti}_2\text{O}_7$* . Physical Review Letters **99**, 237202 (2007).

- [219] J. P. C. Ruff, Z. Islam, J. P. Clancy, K. A. Ross, H. Nojiri, Y. H. Matsuda, H. A. Dabkowska, A. D. Dabkowski, and B. D. Gaulin. *Magnetoelastics of a spin liquid: X-ray diffraction studies of  $Tb_2Ti_2O_7$  in pulsed magnetic fields*. Physical Review Letters **105**, 077203 (2010).
- [220] B. D. Gaulin, J. S. Gardner, P. A. McClarty, and M. J. P. Gingras. *Lack of evidence for a singlet crystal-field ground state in the magnetic pyrochlore  $Tb_2Ti_2O_7$* . Physical Review B **84**, 140402 (2011).
- [221] T. Taniguchi, H. Kadowaki, H. Takatsu, B. Fåk, J. Ollivier, T. Yamazaki, T. J. Sato, H. Yoshizawa, Y. Shimura, T. Sakakibara, T. Hong, K. Goto, L. R. Yaraskavitch, and J. B. Kycia. *Long-range order and spin-liquid states of polycrystalline  $Tb_{2+x}Ti_{2-x}O_{7+y}$* . Physical Review B **87**, 060408 (2013).
- [222] E. Constable, R. Ballou, J. Robert, C. Decorse, J.-B. Brubach, P. Roy, E. Lhotel, L. Del-Rey, V. Simonet, S. Petit, and S. deBrion. *Double vibronic process in the quantum spin ice candidate  $Tb_2Ti_2O_7$  revealed by terahertz spectroscopy*. Physical Review B **95**, 020415 (2017).
- [223] B. C. den Hertog and M. J. P. Gingras. *Dipolar interactions and origin of spin ice in Ising pyrochlore magnets*. Physical Review Letters **84**, 3430 (2000).
- [224] C. Mauws, A. M. Hallas, G. Sala, A. A. Aczel, P. M. Sarte, J. Gaudet, D. Ziat, J. A. Quilliam, J. A. Lussier, M. Bieringer, H. D. Zhou, A. Wildes, M. B. Stone, D. Abernathy, G. M. Luke, B. D. Gaulin, and C. R. Wiebe. *Dipolar-octupolar Ising antiferromagnetism in  $Sm_2Ti_2O_7$ : A moment fragmentation candidate*. Physical Review B **98**, 100401 (2018).
- [225] E. Lhotel, S. Petit, S. Guitteny, O. Florea, M. C. Hatnean, C. Colin, E. Ressouche, M. R. Lees, and G. Balakrishnan. *Fluctuations and All-In-All-Out Ordering in Dipole-Octupole  $Nd_2Zr_2O_7$* . Physical Review Letters **115**, 197202 (2015).
- [226] O. Benton, O. Sikora, and N. Shannon. *Seeing the light: Experimental signatures of emergent electromagnetism in a quantum spin ice*. Physical Review B **86**, 075154 (2012).
- [227] T. Fennell, P. P. Deen, A. R. Wildes, K. Schmalzl, D. Prabhakaran, A. T. Boothroyd, R. J. Aldus, D. F. McMorrow, and S. T. Bramwell. *Magnetic Coulomb phase in the spin ice  $Ho_2Ti_2O_7$* . Science **326**, 415 (2009).
- [228] M. Twengström, P. Henelius, and S. T. Bramwell. *Screening and the pinch point paradox in spin ice*. Physical Review Research **2**, 013305 (2020).
- [229] T. Fennell, M. Kenzelmann, B. Roessli, M. K. Haas, and R. J. Cava. *Power-law spin correlations in the pyrochlore antiferromagnet  $Tb_2Ti_2O_7$* . Physical Review Letters **109**, 017201 (2012).



- [230] S. Petit, P. Bonville, J. Robert, C. Decorse, and I. Mirebeau. *Spin liquid correlations, anisotropic exchange, and symmetry breaking in  $Tb_2Ti_2O_7$* . Physical Review B **86**, 174403 (2012).
- [231] T. T. A. Lummen, I. P. Handayani, M. C. Donker, D. Fausti, G. Dhahlenne, P. Berthet, A. Revcolevschi, and P. H. M. Van Loosdrecht. *Phonon and crystal field excitations in geometrically frustrated rare earth titanates*. Physical Review B **77**, 214310 (2008).
- [232] I. Mirebeau, P. Bonville, and M. Hennion. *Magnetic excitations in  $Tb_2Sn_2O_7$  and  $Tb_2Ti_2O_7$  as measured by inelastic neutron scattering*. Physical Review B **76**, 184436 (2007).
- [233] C. Z. Bi, J. Y. Ma, B. R. Zhao, Z. Tang, D. Yin, C. Z. Li, D. Z. Yao, J. Shi, and X. G. Qiu. *Far infrared optical properties of the pyrochlore spin ice compound  $Dy_2Ti_2O_7$* . Journal of Physics: Condensed Matter **17**, 5225 (2005).
- [234] I. Mirebeau, A. Apetrei, J. Rodríguez-Carvajal, P. Bonville, A. Forget, D. Colson, V. Glazkov, J. P. Sanchez, O. Isnard, and E. Suard. *Ordered spin ice state and magnetic fluctuations in  $Tb_2Sn_2O_7$* . Physical Review Letters **94**, 246402 (2005).



---

# List of Figures

---

1.1	Possible arrangements of three spins located on the corners of a triangle for ferromagnetic (a) and antiferromagnetic (b) interactions. . . . .	3
1.2	The two-dimensional honeycomb (a) and kagome (b) lattice. . . . .	3
1.3	(a) Tetrahedra in spin-ice with a 2-in/2-out local organising principle and (b) after flipping the connecting spin to a 3-in/1-out and 1-in/3-out local organising principle, such that magnetic charges are created. . . . .	4
2.1	Dielectric function and reflectance of a Lorentzian oscillator. . . . .	13
2.2	Model of a one dimensional diatomic chain with a lattice parameter $a$ . . . . .	14
2.3	Dispersion of the diatomic chain (Eq. (2.29) and Eq. (2.30)), showing the two phonon branches in the first Brillouin zone. . . . .	16
2.4	Ferroelectric hysteresis loop of a PMN-PT-BT actuator. . . . .	19
2.5	Landau free energy as a function of the order parameter $\eta$ and the order parameter $\eta$ as a function of temperature. . . . .	21
3.1	Photo of the FTIR spectrometer used throughout my thesis. . . . .	24
3.2	Beam path of an FTIR spectrometer with a Michelson interferometer for transmission measurements. . . . .	25
3.3	Beam path of the FTIR spectrometer with the Michelson interferometer. . . . .	26
3.4	Beam path of transmission and reflectivity arrangements around the sample. . . . .	27
3.5	Effective bandwidth of the different spectral settings. . . . .	29
3.6	Picture of the flow cryostat and the sample mount used within the cryostat. . . . .	30
3.7	Example of a data set in the FIR regime ( $\text{Pr}_3\text{Ga}_5\text{SiO}_{14}$ ). . . . .	31
3.8	Calculation of the reflectance in the FIR region of the $\text{Pr}_3\text{Ga}_5\text{SiO}_{14}$ sample by dividing the sample spectrum with the gold reference. . . . .	32
3.9	Plot of the integration path $\Gamma$ (red dashed line) composited out of the four segments ① to ④ in the complex $\omega'$ -space. . . . .	35
3.10	Beam path and photo of the Mach-Zehnder interferometer . . . . .	41
3.11	Image of BWO; working ranges of the different BWOs; sample mount. . . . .	41
3.12	Overview of the spectroscopic ranges of the used experimental techniques. . . . .	45
4.1	The langasite structure. . . . .	49
4.2	Photo of the four langasite a-cut crystals. . . . .	50
4.3	Reflectance of pure langasite (LGS) for $E  c$ between $20\text{ cm}^{-1}$ and $600\text{ cm}^{-1}$ . The four arrows indicate the positions of four lowest frequency phonons. . . . .	53
4.4	Comparison of raw reflectance with fits of LGS ( $E  c$ ). . . . .	54
4.5	Dielectric function of pure langasite (LGS) $E  c$ , split into the real part, $\varepsilon_1$ (a), and the imaginary part, $\varepsilon_2$ (b). . . . .	56

4.6	Fits of P1 and P2 plotted along with the $\varepsilon_2$ spectra at (a) 10 K, (b) 200 K and (c) 300 K. . . . .	56
4.7	Fitting parameters including the dielectric contribution, $\Delta\varepsilon$ (a), and resonance frequency, $\bar{\nu}_0$ (b), of LGS for E  c polarisation. The inset in (a) shows the spectral weight, $SW = \Delta\varepsilon \cdot \bar{\nu}_0^2$ , of the P1 and P2 phonons. . . . .	57
4.8	Reflectance (a) and dielectric function (b,c) of LGS for E  b* at different temperatures in the FIR range. . . . .	58
4.9	Room temperature reflectance of all four langasite samples for E  c. . . . .	60
4.10	Dielectric function of all four langasite samples for E  c (a,b). Fitting parameters of the anomalous low-frequency phonon structure including resonance frequency (c), dielectric contribution (d) and spectral weight (e). . . . .	61
4.11	Squared frequencies of P1 phonon of all four langasites. Linear fits intercept the baseline at different temperatures. . . . .	62
4.12	Comparison of static permittivity of the four langasites for E  c polarisation. . . . .	63
4.13	Measurements of the HoLGS transmission (E  c polarisation) performed using the THz-spectrometer. (a) Comparison of raw transmission and fit at 2 K, (b) relative change in transmission for different external magnetic fields, H  b*. . . . .	64
4.14	Broadband reflectance (between $50\text{ cm}^{-1}$ and $1500\text{ cm}^{-1}$ ) and imaginary part of the dielectric function (from $50\text{ cm}^{-1}$ to $550\text{ cm}^{-1}$ ) of the four a-cut langasite samples obtained for E  b* polarisation. . . . .	65
4.15	The reflectance of a HoLGS c-cut crystal is plotted in steps of $45^\circ$ polarisation rotation. The upper plot, (a), was conducted under room temperature conditions, (b) at a sample temperature of 10 K. . . . .	67
5.1	The low temperature ( <i>Pcmn</i> ) crystalline structure of $\text{Cu}_3\text{Bi}(\text{SeO}_3)_2\text{O}_2\text{Cl}$ . . . . .	71
5.2	Far infrared reflectance of CBSCl in the range from $10\text{ cm}^{-1}$ to $900\text{ cm}^{-1}$ . . . . .	73
5.3	Far infrared reflectance and complex permittivity of CBSCl in the range below $120\text{ cm}^{-1}$ as a function of temperature. . . . .	75
5.4	Fitted properties of the CBSCl oscillators as a function of temperature. . . . .	76
5.5	Antiferroelectric double hysteresis loop of $\text{PbZrO}_3$ . . . . .	78
5.6	Analysis of the squared frequency for the $\bar{\nu}_F$ and $\bar{\nu}_{AF}$ modes. . . . .	79
5.7	Picture of the local depolarising fields, $P_A$ and $P_B$ , of the $\bar{\nu}_F$ and $\bar{\nu}_{AF}$ phonon. The low-temperature phase is plotted in (a), the high-temperature phase in (b). The red circles represent the Cu ions. . . . .	80
5.8	Analysis of squared frequency for $\bar{\nu}_F$ and $\bar{\nu}_{AF}$ modes: difference and ratio. . . . .	82
6.1	The pyrochlore lattice: (a) crystalline structure, (b) tetrahedra network of <i>A</i> -sites. . . . .	87
6.2	Visualisation of a tetrahedron in water ice (a) and spin ice (b) as a result of the 2-in/2-out local organising principle. . . . .	88

6.3	Visualisation of six possible arrangements of four spins on the corners of a tetrahedron in a spin ice, following the 2-in/2-out ordering. . . .	89
6.4	Magnetic arrangement at 0 K as a function of the effective exchange energy $J_{zz}$ . . . . .	90
6.5	Comparison of neutron scattering patterns of (a) $\text{Sm}_2\text{Ti}_2\text{O}_7$ , (b) $\text{Ho}_2\text{Ti}_2\text{O}_7$ and (c) $\text{Tb}_2\text{Ti}_2\text{O}_7$ . . . . .	91
6.6	Reflectance of HTO pyrochlore plotted between $40\text{ cm}^{-1}$ and $1400\text{ cm}^{-1}$ as a function of temperature. . . . .	93
6.7	Imaginary part of the dielectric function of HTO pyrochlore plotted between $40\text{ cm}^{-1}$ and $600\text{ cm}^{-1}$ as a function of temperature. . . . .	94
6.8	Frequencies of the 7 phonons in HTO plotted as a function of temperature. The figure compares the results of $k\parallel[111]$ and $k\parallel[100]$ . . . . .	94
6.9	Reflectance of TTO pyrochlore plotted between $40\text{ cm}^{-1}$ and $1400\text{ cm}^{-1}$ as a function of temperature. . . . .	95
6.10	Imaginary part of the dielectric function of the TTO pyrochlore, plotted between $40\text{ cm}^{-1}$ and $600\text{ cm}^{-1}$ as a function of temperature. . . . .	96
6.11	Fitted phonon frequencies of TTO pyrochlore plotted as a function of temperature. . . . .	97
6.12	Spectra of TSO. . . . .	99
A.1	Data of LGS (left) and HoLGS (right) for $E\parallel c$ polarisation. . . . .	108
A.2	Data of NGS (left) and PGS (right) for $E\parallel c$ polarisation. . . . .	109
A.3	Data of LGS (left) and HoLGS (right) for $E\parallel b^*$ polarisation. . . . .	110
A.4	Data of NGS (left) and PGS (right) for $E\parallel b^*$ polarisation. . . . .	111
A.5	The raw reflectance and the dielectric function are compared with data obtained by fitting. . . . .	114
A.6	Reflectance spectra and dielectric function (fit) of four temperatures plotted between $0\text{ cm}^{-1}$ and $900\text{ cm}^{-1}$ . . . . .	115



---

# List of Tables

---

3.1	Overview of the different FTIR spectrometer settings. . . . .	28
6.1	Frequency splitting $\Delta$ of the TTO phonons in $\text{cm}^{-1}$ . . . . .	97
A.1	Oscillator data of the four langasites at room temperature and $E  c$ . Phonon 1 represents the low frequency structure, which consists out of two phonons at lower temperatures. The fit was performed with one oscillator only. . . . .	106
A.2	Oscillator data of the four langasites at room temperature and $E  b^*$ .	107
A.3	Oscillator data of CBSCl for $E  a$ polarisation. . . . .	112
A.4	Oscillator data of CBSCl for $E  b$ polarisation. . . . .	113
A.5	Phonon frequencies of TTO. . . . .	116
A.6	Phonon frequencies of HTO and TSO. . . . .	116





---

# Acknowledgement

---

*“Sometimes, a little frustration  
can make life interesting.”*  
—Leon Balents in [6].

In February 2017, my employment as a Project assistant at TU Wien started. This was also my first day as a PhD student. I didn’t have a real clue what will happen in the next years (despite me working on my thesis). In an optimistic way I looked forward to a good time without frustration. This changed when I learned on my first days that I will study magnetically frustrated materials. Now, more than four and a half years later, a first complete version of my PhD-Thesis is written. This is the right point to take a bit of time to remember what crazy stuff and stories happened in this period. It is also time to wallow a bit in memories and to thank to a lot of people that made this last years (in a positive way) unforgettable and preserve me from being too frustrated.<sup>18</sup>

First of all I want to provide a few (probably unnecessary) numbers to show and summarize what happened within my PhD-time:

1 PhD-Thesis	=
3 visits	of Solids4Fun SummerSchools
4.636 a	ago did I start my PhD
9 contracts	were signed with TU (add ons included)
11 trips	to meetings and visits with
14.7 Mm	total travelling distance
18h05	lasted my longest working day (June 19 <sup>th</sup> , 2019 8.35 till 2.40 the next day)
26+ talks	that I have visited
28 stops	was my way to Freihaus and back home with the 2er
30.6 °C	the highest room temperature measured in the lab
46 batteries	each 9 V, were used to run the bolometer
95 pages	are fully written in my lab book
192 stairs	to reach my office in the 9 <sup>th</sup> floor
199 d	Covid-19-connected (forced) home office
278 tests	of Grundlagen 1a/1b did I correct
756 d	on which I visited Freihaus
4738 emails	did I delete
~ 3*10 <sup>5</sup> characters	typed in all .tex and .bib files so far
∞ happy	my actual feeling.

---

<sup>18</sup>This is the last frustration joke. Promised.

---

Thus, I finally come to the acknowledgement, and for sure I want to start with my two supervisors:

*Andrei Pimenov:* Lieber Andrei! Ich möchte dir zuerst einmal danken, mir die Möglichkeit gegeben zu haben, meine Doktorarbeit in deiner Gruppe machen zu dürfen. Du hast mir die Stelle gegeben, ohne mich groß zu kennen und es war kein Problem für dich, dass ich erst in einigen Monaten mit meiner Arbeit anfangen wollte, um in Dresden noch ein bisschen Luft im Ausland schnuppern zu können. Deine Bürotür stand mir und allen andern der Gruppe immer offen, um uns mit Rat und Tat zu unterstützen. Während der letzten Jahre hatte ich so gut wie alle Freiheiten, die man sich nur wünschen konnte. Danke für die gute Betreuung und die vielen Erfahrungen, die ich in den letzten Jahren sammeln durfte.

*Evan Constable:* Dear Evan! It was a real pleasure for me to work under your guidance. Thank you for all your patience, for all the time you spent describing me things and answering my questions. Sometimes I felt you are my private solid state physics teacher. Most of all I want to thank you for proof reading all kind of manuscripts. However, TU-life is not only working, but also socialising. Thus, I want to thank you for all the good time we had and for showing us the cool-postdoc style of life. Last but not least I highly appreciate how you helped me improving my English skills.

*Anna Pimenov:* Liebe Anna, vielen Dank, dass du immer drauf schaust, dass bei uns als Arbeitsgruppe die sozialen Events nicht zu kurz kommen. Mit den beiden Kunstprojekten hast du uns gezeigt, was passiert, wenn Kunst auf Wissenschaft trifft und uns damit neue Blicke auf unseren Alltag näher gebracht. Das Experiment an dem ich die meisten Messungen durchgeführt habe wurde von einem aufstrebenden Nachwachskünstler als Gemälde verewigt – wer kann das schon behaupten.

A few lines to my co-workers of the Solid State Spectroscopy Group: You made my PhD time unforgettable. Thanks for all the discussions, coffee breaks, our night-outs, our conference trips, for building impressive snow sculptures, and indeed for having a good, (mostly) calm time in the office. I want to write some personal lines to many of you:

*Alexey Shuvaev:* Lieber Alexey, danke für die Hilfe im U4 und danke, dass du mir geholfen hast zu verstehen, wie die Gruppe tatsächlich funktioniert.

*David Szaller:* Lieber David, danke für die vielen unvergesslichen Momente auf unseren gemeinsamen Konferenzen, wo du uns gezeigt hast, wie intensiv man eine Tagung ausleben kann und vor allem für deine Willenskraft, nicht während meiner Vorträge einzuschlafen.

*Jan Gospodaric:* Dear Jan, thank you for being the world's best conference travel guide and the local "the group has to visit Wiener Wiesn" organiser. You made us really enjoying all kind of informal meetings of the group. In home office I solved one issue. You are right, there is really a need to darken the windows because of the sun shining on the screen. The other riddle, why there is quite often a weird "spin counter" running on your screen, remains still unsolved...

---

*Lukas Weymann:* Auch wenn du in deiner Danksagung die Langasite noch als unsere gemeinsame Leidenschaft bezeichnet hast, wissen wir doch beide, dass du immer nur ein Auge auf die Wissenschaftsethik geworfen hast. Lieber Lukas, ich möchte dir vor allem danken, dass du immer zugehört hast, wenn ich mich ausnahmsweise über irgendetwas aufregen musste (was so gut wie nie vorkam, höchstens ein-, vielleicht zweimal [pro von dir zu wählender Zeiteinheit]).

*Janek Wettstein:* Lieber Janek, dir möchte ich besonders für unsere regelmäßigen online Meetings während der Lockdowns danken. Danke auch fürs Korrekturlesen. Da du ja noch ein paar Jahre (leider ohne uns) vor dir hast, möchte ich dir viel Erfolg für den weiteren Verlauf deiner Diss wünschen. Ich hoffe, dass sich alles wieder halbwegs normalisiert, damit auch du alles was zu einer richtigen PhD-Zeit gehört, erleben darfst. Nun setzt du ja auch die Arbeit von Lukas und mir an den Langasiten fort, dabei wünsch ich dir viel Freude und bahnbrechende Resultate (ja nicht mich als Koauthor vergessen).

*The Mittagessen Bande (also known as BILLA boys):* Thanks guys for the fruitful discussions about what to eat for lunch and for giving answers to fundamental questions, like if go to park for lunch or not. #LAAAANCH

*Maxi, Elena, Sahra:* Bei euch dreien möchte ich mich für die gute Zusammenarbeit bedanken. Ich hoffe, ihr könnt die Zeit in der Gruppe in guter Erinnerung behalten. Alles Gute für das weitere Studium und für eure nächsten Herausforderungen. Sahra, dir viel Freude bei der Diplomarbeit in unserer Gruppe.

There are many people I want to thank, being not directly connected to my working group. In particular, I want to appreciate:

*André Vogel:* Lieber André, vielen Dank, dass du dich so gut um uns alle vom DK Solids4Fun gekümmert hast. Wir haben immer gewusst, mit dir eine Ansprechperson für alle unsere organisatorischen Probleme zu haben – deine Bürotür war stets offen. Jede Reisekostenabrechnung bist du mit uns durchgegangen, hast mit mir sogar in den Tiefen der TU Bürokratie meinen verlorenen/verschwundenen Reiseantrag gesucht. Bei den SummerSchools in Waidhofen lag dein Hauptaugenmerk darauf, dass wir alle gemeinsam eine gute Zeit haben. Daher nochmal vielen Dank, dass du uns eine schöne Zeit bereitet hast und immer ein offenes Ohr für uns hattest. Jetzt, nachdem Solids4Fun ausgelaufen ist, kann ich dir nur alles Gute für deine neuen Aufgaben wünschen.

*PhD-students of S4F:* Dear colleagues, thank you for the scientific discussions and the time we spent together in Waidhofen.

*Our colleagues from Moscow:* Thank you for the good collaboration and all the input for the langasites. Special thanks to Artem Kuzmenko for his static measurements of NGS and PGS langasite.

*Isabella Floss:* Liebe Isi, vielen Dank für all deine Unterstützung beim Programmieren meines Kramers-Kronig Codes. Tatsächlich zählst du zu den wenigen, die mich schon seit Anfang meines Studiums an begleiten und warst vor allem in den

---

ersten beiden Semestern eine große mentale Stütze. Bald elf Jahre ist es her, als es uns regelmäßig kalt über den Rücken lief, wenn die Tür vom Hörsaal aufgerissen wurde. Glücklicherweise hat sich dein “es wird fix besser” bewahrheitet und so kann ich Jahre später auch gerne und mit einem Lächeln auf diese Zeit zurückblicken.

*Meine alte Gruppe:* Vielen Dank euch allen, dass ich immer wieder auf einen Kaffee und Tratsch zu euch kommen konnte. Es hat mir gut getan neue Blickwinkel auf den Alltag zu bekommen. Tatsächlich hatte ich das Glück, meine Diplomarbeit bei und mit euch machen zu dürfen. Erst während meiner PhD-Zeit wurde mir bewusst, wie viel ich schon damals gelernt habe. Vor allem, wenn es darum geht, wie die Wissenschaft tatsächlich läuft – dafür auch im Nachhinein danke. Martin Müller, dir möchte extra danken – immerhin hast du mir geraten, “*mit einer Diss beim Andrei kannst nichts falsch machen*” und mich so bestärkt, mich für die Stelle erst zu bewerben.

*Dani und Samy:* Vielen Dank euch beiden für all unsere Treffen und all die Fladen die wir gemeinsam gegessen haben. Es tut gut zu wissen, dass ich euch immer alles erzählen kann und ihr immer für mich da seid.

*Jacqueline Keintzel:* Liebe Jacy, tatsächlich hab ich während der letzten Jahre im Büro als erstes auf deine (fast) tägliche email geantwortet. Danke, dass ich dir immer schreiben konnte, wenn ich mal ein Problem hatte oder sonst was nicht gut lief. Ich hoff unsere email-Freundschaft bleibt weiter bestehen, zur Not muss ich halt am Weg zur Arbeit schreiben. Das einzige, was sich definitiv ändern wird ist meine email-Adresse.

Den *Damen vom Sekretariat* möchte ich für die Unterstützung bei allen vertraglichen und organisatorischen Problemen danken.

*meine Familie:* Danke euch allen für die Unterstützung die ich meine ganzes Leben lang, nicht nur während meines Studiums, bekommen habe. Danke, dass ihr immer hinter mir und meinen Entscheidungen gestanden seid und immer für mich da seid. Einfach nur danke!